

University of New Mexico

**UNM Digital Repository**

---

Mechanical Engineering ETDs

Engineering ETDs

---

Summer 8-1-2022

## **DESIGN, MICROFABRICATION AND CHARACTERIZATION OF VIBRATING MESH ATOMIZER FOR VISCOUS FLUIDS**

Pallavi Sharma

*University of New Mexico*

Follow this and additional works at: [https://digitalrepository.unm.edu/me\\_etds](https://digitalrepository.unm.edu/me_etds)



Part of the [Mechanical Engineering Commons](#)

---

### **Recommended Citation**

Sharma, Pallavi. "DESIGN, MICROFABRICATION AND CHARACTERIZATION OF VIBRATING MESH ATOMIZER FOR VISCOUS FLUIDS." (2022). [https://digitalrepository.unm.edu/me\\_etds/215](https://digitalrepository.unm.edu/me_etds/215)

This Dissertation is brought to you for free and open access by the Engineering ETDs at UNM Digital Repository. It has been accepted for inclusion in Mechanical Engineering ETDs by an authorized administrator of UNM Digital Repository. For more information, please contact [disc@unm.edu](mailto:disc@unm.edu).

Pallavi Sharma

*Candidate*

Mechanical Engineering

*Department*

This dissertation is approved, and it is acceptable in quality and form for publication:

*Approved by the Dissertation Committee:*

Dr. Nathan Jackson, Chair

Dr. Matthias Pleil

Dr. Matthew Campen

Dr. Daniel Banuti

**DESIGN, MICROFABRICATION AND CHARACTERIZATION OF  
VIBRATING MESH ATOMIZER FOR VISCOUS FLUIDS**

by

**PALLAVI SHARMA**

Bachelor of Engineering, Rajiv Gandhi Proudyogiki Vishwavidyalaya, 2013

Master of Technology, Maulana Azad National Institute of Technology, 2015

DISSERTATION

Submitted in Partial Fulfillment of the

Requirements for the Degree of

**Doctor of Philosophy in Engineering**

The University of New Mexico

Albuquerque, New Mexico

**July 2022**

## **ACKNOWLEDGEMENTS**

I would like to convey my gratitude to my parents, Prem Narayan Sharma, and Anita Sharma, without whom I would not have accomplished as much. I would also want to express my gratitude to my husband, Nitesh Sharma, and my in-laws for his unwavering support and understanding.

Dr. Nathan Jackson and Dr. Matthias Pleil, my mentors, have been a tremendous source of professional and personal support. Their selflessness in terms of educating, advising, encouraging, and motivating their students is only equaled by their inexhaustible enthusiasm. I would also like to thank members of SMART group and Manufacturing Training and Technology Center (MTTC) at UNM for their assistance and help throughout this journey.

Financial support through a STC UNM Gap Fund and the Research Allocation Committee Grant from University of New is acknowledged and appreciated. I was also supported by National Science Foundation Grant, DUE #1700678, Support Center for Microsystems Education.

# **DESIGN, MICROFABRICATION AND CHARACTERIZATION OF VIBRATING MESH ATOMIZER FOR VISCOUS FLUIDS**

**By:**

**Pallavi Sharma**

**B.E Mechanical Engineering, RGPV, 2013**

**M.Tech Mechanical Engineering, MANIT, 2015**

**Ph.D. Engineering, University of New Mexico, 2022**

## **ABSTRACT**

This research focuses on a new piezoelectrically driven Micro Electromechanical Systems based vibrating mesh atomizer that generates the pressure differential required for droplet ejection or spray production using frequency resonances in the 100 kHz range. This study involves device construction and experimental characterization to comprehend the device's operation and the influence of various factors on its performance and determine the limitations of a range of working fluids to atomize.

A novel approach to integrating polymer-based micro heaters with a vibrating mesh atomizer as a monolithic component is presented to expand the range of working liquids for the MEMS device. The enhanced MEMS vibrating mesh atomizer with microheater can operate with viscosities up to 28cP, which is nine times more than the threshold of 3cPs for the independent device. The innovative integrated atomizer device enables new applications in several sectors.

# TABLE OF CONTENTS

<b>LIST OF FIGURES .....</b>	<b>vii</b>
<b>LIST OF TABLES .....</b>	<b>xiv</b>
<b>CHAPTER 1 INTRODUCTION .....</b>	<b>1</b>
1.1 Motivation.....	1
1.2 Challenges.....	3
1.3 Background.....	4
1.3.1 Atomizer Technologies .....	5
1.3.2 Applications of VM technology.....	9
1.4 Literature Review.....	11
1.5 Market and Scope .....	14
1.6 Objective and Contribution.....	15
1.7 Summary and report Organization.....	18
<b>CHAPTER 2 FINITE ELEMENT MODELLING OF VIBRATING MESH ATOMIZER</b> <b>.....</b>	<b>19</b>
2.1 Working principle .....	19
2.2 Structural Mechanics Analysis .....	21
2.2.1 Eigen Frequency and Piezoelectric effect governing equations .....	21
2.2.2 FEM Simulation Model .....	23
2.2.3 Eigen Frequency Modal Analysis.....	25
2.2.4 Frequency Domain Analysis.....	29
2.3 Fluid flow Analysis.....	31

2.3.1 Fluid-flow Governing Equations and Numerical Simulations.....	32
2.3.2 Two-Phase flow Simulations .....	32
2.3.2.1 Simulation Model.....	33
2.3.2.2 Nozzle Shape Simulations .....	36
2.3.2.3 Effect of Orifice Diameter on ejected droplet diameter.....	39
2.4 Summary .....	41
<b>CHAPTER 3 FABRICATION AND CHARACTERIZATION OF VIBRATING MESH</b>	
<b>ATOMIZER .....</b>	<b>44</b>
3.1 Photomask layout.....	45
3.2. Vibrating Mesh Atomizer Microfabrication .....	47
3.3 DRIE Characterization.....	50
3.3.1 Effect of C <sub>4</sub> F <sub>8</sub> and SF <sub>6</sub> on Side wall profile.....	54
3.3.2 Effect of C <sub>4</sub> F <sub>8</sub> and SF <sub>6</sub> on Grass formation.....	56
3.3.3 Effect of C <sub>4</sub> F <sub>8</sub> and SF <sub>6</sub> on etch rates .....	59
3.3.4 Effect of cooling on the etch profiles.....	59
3.4 Experimental setup and Characterization of Vibrating mesh atomizer .....	62
3.4.1. Experimental Setup.....	62
3.4.2. Experimental Demonstration of Vibrating Mesh function .....	64
3.4.3. Characterization of Atomizer.....	65
3.4.3.1. Operating Frequency and Mode.....	65
3.4.3.2 Droplet Distribution of Different Liquids.....	69
3.5. Comparison of Silicon based and commercial vibrating mesh atomizer.....	70

3.5.1. Materials and methods .....	70
3.5.2 Droplet distribution results .....	72
3.5.2.1 Comparison of vibration dynamics of VMA Devices .....	74
3.5.2.2 Droplet Size distribution of metallic VMA and MEMS VMA.....	76
3.5.2.3 Temperature Distribution.....	86
3.6 Summary .....	87
<b>CHAPTER 4 FEM AND MICROFABRICATION OF THE MICROHEATER.....</b>	<b>90</b>
4.1 Microheater Design.....	91
4.2 Microheater Materials .....	92
4.3 Numerical simulation using COMSOL .....	93
4.3.1 Heat Transfer Governing Equations .....	94
4.3.2 Simulation Model.....	96
4.3.3 Physics and Boundary conditions .....	97
4.3.4 Study Configuration.....	98
4.4 Simulation results.....	100
4.4.1 Temperature distributions .....	100
4.4.2 Heater Height Simulations.....	103
4.4.3 Heat transfer coefficient Simulation .....	104
4.5 Fabrication Method.....	105
4.6 Characterization .....	110
4.7 Summary .....	115

<b>CHAPTER 5 INTEGRATION OF VIBRATING MESH ATOMIZER AND MICROHEATER .....</b>	<b>116</b>
5.1. Integrated device and working concept .....	116
5.2. Experimental setup.....	119
5.3 Results and Discussion .....	121
5.4 Summary .....	128
<b>CHAPTER 6 APPLICATION OF MEMS VIBRATING MESH TECHNOLOGY ...</b>	<b>130</b>
6.1 Vibrating Mesh Atomizer for Spin Spray Deposition of SOG and SU-8.....	130
6.1.1 Spin Spray Deposition Experimental Setup.....	132
6.1.2 Characterization of produced film properties – Etching, Uniformity, Roughness and Pattern ability .....	135
6.2 Spray cooling using mems vibrating mesh atomizer .....	145
6.2.1 Experimental Setup.....	148
6.2.2 Results and Discussion .....	150
6.2.2.1 Spray Angle Measurement.....	153
6.2.2.2 Heat transfer measurements .....	157
6.3 Summary .....	162
<b>CHAPTER 7 CONCLUSION AND RECOMMENDATION FOR FUTURE WORK.....</b>	<b>163</b>
<b>.....</b>	<b>163</b>
<b>APPENDIX A .....</b>	<b>170</b>
<b>REFERENCES.....</b>	<b>171</b>

## LIST OF FIGURES

Figure 1.1. Schematic of working principle of a jet atomizer .....	5
Figure 1.2. Schematic of working principle of an ultrasonic atomizer .....	6
Figure 1.3. Schematic of (a) passive type atomizer – vibrations of the piezo crystal are transmitted through transducer and passed to the mesh and (b) active type atomizer – vibrating element is surrounding the mesh at the center .....	8
Figure 2.1. Schematic of (a) Vibrating mesh atomizer, (b) cross-sectional view of dispenser structure and working concept .....	20
Figure 2.2 Analytic solution according to circular plate theory for varying (a) thickness, (b) Young’s Modulus and (c) radius.....	21
Figure 2.3. Schematic of (a) Meshed 3D simulation model, (b) Fixed boundary, (c) model with PZT ring and electrodes, (d) zoomed view of top and bottom electrode.....	24
Figure 2.4. Mesh independent graph for frequency .....	25
Figure 2.5. First nine resonant frequencies with the shape mode .....	26
Figure 2.6. Frequency spectrum of the normalized out of plane displacement amplitude ....	27
Figure 2.7. FEM results for determining (0,2) mode resonance frequency for silicon membrane with respect to membrane thickness (black) and membrane radius (red).....	28
Figure 2.8. FEM results for different frequency mode ((0,1), (0,2), (0,3)) displacement for membrane diameter (a) 2 mm, (b) 6 mm and (c) 10 mm at 100 peak to peak voltage supply ..	29
Figure 2.9. FEM analysis of displacement across the membrane (a) (0,1) mode, (b) (0,2) mode, and (c) (0,3) mode with varying applied voltage .....	30

Figure 2.10. A simplified drawing of the atomizer with examples of involved components indicated.....	32
Figure 2.11. A 2D drawing representing: (a) the simulation model, (b) two-phase flow COMSOL model and (c) Meshed model at the orifice.....	34
Figure 2.12. The function generator waveform used as an input to the amplifier for droplet ejection (a) Voltage, (b) velocity, $v(r)$ .....	36
Figure 2.13. Schematic of different nozzle shapes (a) Straight, (b) Cymbal, (c) Taper and (d) Hourglass .....	36
Figure 2.14. Droplet size for various nozzle shape.....	37
Figure 2.15. (a) a set of images showing a model that did not eject any droplet due to use of small inlet velocity, (b) a set of images showing a model that eject a droplet successfully when large inlet velocity is used.....	38
Figure 2.16. Ejected droplet velocity and mass at variable input velocity .....	39
Figure 2.17. Droplet diameter as a function of orifice diameter at different inlet velocity, $v(r)$ for taper shape nozzle .....	40
Figure 2.18. Ohnesorge number Vs Reynolds number graph for optimal working conditions .....	41
Figure 3.1. Front and backside photomasks: (a) front side used to define the structure of nozzle arrays, (b) backside used to define the holder and cavity size with alignment mark .....	46
Figure 3.2. Schematic view of fabrication process of vibrating mesh atomizer device .....	49
Figure 3.3. (a) Aperture pattern after developing, (b) aperture after oxide mask etch (c) apertures after KOH etch to form nozzles .....	50
Figure 3.4. Silicon crystal plane etch using KOH .....	50

Figure 3.5. Shape profile of trenches etched with variable  $C_4F_8$  flow rate with etch and passivation cycle ratio of (a)5:1, (b)7:2 ..... 55

Figure 3.6. Shape profile of trenches etched with variable  $SF_6$  flow rate with etch and passivation cycle ratio of (a)5:1, (b)7:2 ..... 56

Figure 3.7. (a), (b) Effect of  $C_4F_8$  on grass formation with etch and passivation cycle ratio 5:1 and 7:2, (c), (d) effect of  $SF_6$  on grass formation with etch and passivation cycle ratio of 5:1 and 7:2..... 58

Figure 3.8. (a) DRIE loading chuck for 6-inch wafer, (b) A 150mm diameter Aluminum plate with 100mm diameter groove for holding 4-inch wafer ..... 60

Figure 3.9. Using optimum recipe parameters - (a), (c) Etched structures with no fomblin oil (no cooling) (b), (d) Etched structures with fomblin oil ..... 60

Figure 3.10. (a) wafer with 80 fabricated atomizer devices, (b) SEM image of array of micro nozzles, (c) SEM image of individual KOH etched nozzle ..... 61

Figure 3.11. Schematic and image of assembled device ..... 61

Figure 3.12. Atomizer testing setup with pulse generator and piezo amplifier and atomizer device ..... 63

Figure 3.13. Image showing aerosol generation from working atomizer64

Figure 3.14. Frequency spectrum of a vibrating mesh atomizer..... 67

Figure 3.15. Velocity measurement of the atomizer..... 68

Figure 3.16. Comparison of measured deformation at different voltage with FEM results .. 69

Figure 3.17. Atomizer type investigated. (a, b) Working principle of ultrasonic mist maker and device image, (c) Vibrational mode of ultrasonic device (0,1), (d) Working principle of

vibrating mesh atomizer, (e) SEM image of single nozzle - metallic VMA and MEMS VMA, (f) Vibrational mode of VMA device (0,2).....	71
Figure 3.18. Nozzle outlet shape of (a) MEMS VMA and (b) Metallic VMA.....	71
Figure 3.19. DI water droplet distribution by devices (a) ultrasonic device, (b) Metallic VMA and (c) MEMS VMA .....	74
Figure 3.20. Frequency spectrum of (a) Metallic VMA, (b) MEMS VMA .....	75
Figure 3.21. Empirical curves of cone angle and loss coefficients in the nozzle .....	78
Figure 3.22. Droplet distribution for Metallic and MEMS VMA for (a) DI water, (b) Albuterol, (c) 20% Glycerol and (d) 10% CBD Water-based.....	80
Figure 3.23. VMD of two devices used for DI water, Albuterol, 20% Glycerol and 10% CBD W-B.....	81
Figure 3.24. Hasse diagram for VMD experiment .....	82
Figure 3.25. Flow rate of (a) Metallic VMA and (b) MEMS VMA.....	84
Figure 3.26. Effect of orifice outlet diameter on (a) Droplet distribution and (b) VMD.....	85
Figure 3.27. (a) Effect of hole pitch on the droplet distribution , (b) Distance of device from laser source on VMD .....	86
Figure 3.28. Surface temperature of (a) metallic VMA, (b) MEMS VMA, (c) Time temperature for both the device after 1 minute of operation.....	87
Figure 4.1. Schematic of adapted microheater design: (a) Meander, (b) Double meander, (c) Driving wheel, (d) S- shape .....	92
Figure 4.2. 3D simulation model of microheater .....	96
Figure 4.3. Meshing configuration of microheater .....	98
Figure 4.4. Thermal maps of top and bottom of D-wheel microheater at 1V.....	101

Figure 4.5. Thermal maps of top and bottom surface of microheater substrate along X direction for (a) double meander, (b) driving wheel, (c) meander and (d) S-shape for applied voltage of 1V..... 101

Figure 4.6. (a) The thermally induced von Mises stresses, (b) Deformation of the planar surface on the fluid side of the membrane..... 102

Figure 4.7. Temperature variation for different microheater thickness at varying applied voltage for D-wheel resistor..... 103

Figure 4.8. Effect of heat transfer coefficient on surface temperature ..... 104

Figure 4.9. Steps and tools for photolithography process..... 106

Figure 4.10. Schematic of sputter tool working and AJA sputter machine ..... 106

Figure 4.11. March plasma Etcher (Reactive ion etching) ..... 107

Figure 4.12. Photomask layout for microheater devices and etch profiles with alignment masks ..... 108

Figure 4.13. (a) Microfabrication steps polymer based microheater, (b) Device images during fabrication steps (after second polyimide layer, during aluminum etch, individual device ..... 110

Figure 4.14. I-V characteristics for four microheater designs ..... 112

Figure 4.15. Microheater performance for different designs ..... 113

Figure 4.16. With Driving wheel design, Comparison of FEM, and measurement temperature-time results for the microheater at 1V supply ..... 114

Figure 5.1 Photomask layout for spacer rings ..... 117

Figure 5.2. (a) Isometric view, (b) Cross-sectional view, (c) Exploded view of 3D model of microheater integrated device ..... 119

Figure 5.3. Tool used for characterization (a) Infrared camera setup, (b) Photographic setup and (c) Sympatec laser setup.....	120
Figure 5.4. Power and temperature profile for different glycerol concentrations with driving wheel microheater design .....	124
Figure 5.5. Photographic images of spray formation with integrated device at different time .....	126
Figure 5.6. Droplet size distribution for different glycerol concentrations with the new device .....	127
Figure 5.7. Spray angle and VMD comparison for glycerol concentration solution.....	128
Figure 6.1. Image of spin-spray setup using vibrating mesh atomizer .....	133
Figure 6.2. (a) SiO <sub>2</sub> film thickness w.r.t final spin speed (b) Spin speed while spray process	136
Figure 6.3. SiO <sub>2</sub> film thickness at various positions on the wafer with final spin speed of 5000 rpm .....	136
Figure 6.4. (a) Etch rate with 6:1 BOE etchant, (b)Etch rate with RIE plasma etcher, (c) Etch rate with Vapor HF. Black and red lines represents best linear fit of the points and error bars represent the standard deviation.....	138
Figure 6.5. SiO <sub>2</sub> film stress deposited by various methods with thicknesses of (500 m, (thermal), 220 nm (Spin), and 320 nm (spin-spray)).....	139
Figure 6.6. Absorbance as a function of wavelength for thermal, spin, and spin-spray coated films of SiO <sub>2</sub> .....	140
Figure 6.7. (a), (b) SEM images of 3D structure coated by spin coating, (c) and (d) SEM images of 3D structure coated by spin spray method.....	141
Figure 6.8. AFM surface profiles: (a) Spin-spray coated SiO <sub>2</sub> , (b) Spin coated SiO <sub>2</sub> .....	142

Figure 6.9. SU-8 resist patterned structures with spin-spray deposition method .....	142
Figure 6.10. KOH etched cavities coated with (a) Spin-spray method, (b) spin coating method .....	143
Figure 6.11. (a) Schematic of the spray cooling setup, (b) setup image of the high-speed camera and device, and (c) Schematic of the droplet distribution measuring system.....	148
Figure 6.12. Droplet distribution curve of (a), (b), (c) Water, IPA, and ethylene glycol coolant with metallic atomizer, (d), (e), (f) Water, IPA, and ethylene glycol coolant with MEMS atomizer.....	153
Figure 6.13. Spray angle of water, IPA, and PEAK (Antifreeze+coolant) for (a) Metallic device, (b) MEMS device .....	155
Figure 6.14. Spray angle comparison for both the devices at variable voltage .....	156
Figure 6.15. (a) Temperature variation and (b) Heat flux variation with time for different cooling liquids for both atomizers .....	157
Figure 6.16. (a) Temperature variation and (b) Heat flux variation with time for the two devices operating at variable voltage.....	159
Figure 6.17. (a) Temperature variation and (b) Heat flux variation with time at different spray height.....	159
Figure 6.18 - (a) Temperature variation and (b) Heat flux variation with time at different spray height.....	160

## LIST OF TABLES

Table 2.1. Material properties used in finite element modelling .....	24
Table 2.2. Dimension of contour – Nozzle with air channel .....	35
Table 3.1. DRIE parameters used in experiments.....	52
Table 3.2. Etch rate and profile angle of trenches etched at different C <sub>4</sub> F <sub>8</sub> flow rate.....	53
Table 3.3. Etch rate and profile angle of trenches etched at different SF <sub>6</sub> flow rate .....	53
Table 3.4. Physiochemical properties of the liquids used.....	76
Table 3.5. Comparing Span and FPF for metallic and MEMS VMA devices.....	79
Table 3.6. Pairwise comparisons of hole size factor levels. Case 6 implies that hole size of 30 μm produces higher VMD compared to hole size diameter of 20 μm .....	82
Table 4.1. Material properties used in the simulations .....	95
Table 5.1. Properties of the liquids used for tests .....	122
Table 6.1. Spin peed variations.....	134
Table 6.2. Etch Rate Variations .....	138
Table 6.3. Droplet density distribution for MEMS and metallic VMA device with various liquids.....	152

# CHAPTER 1

## INTRODUCTION

### 1.1 Motivation

Spray generation has significant importance in many industry applications such as (i) pharmaceutical manufacturing process for spray drying to atomize the solution and convert to drier powders[1], (ii) in semiconductor industry for polishing and plating photosensitive emulsions on silicon wafers while fabrication of circuits[2], (iii) industrial burners uses the atomized heavy fuel oils for combustion [3], (iv) food industry for spray drying of food e.g. water and corn starch suspensions [4], (v) inkjet printing, (vi) cosmetics, (vii) Vaping and home care. In most of these applications, droplets with the desired size distribution are needed, and a variety of fluids with various physiochemical properties are used (density, viscosity, and surface tension). Droplet size and nozzle diameter typically vary from 30 $\mu\text{m}$  to 10 $\mu\text{m}$ , however for some applications, droplet size ranges as low as 5 $\mu\text{m}$  are ideal (inhalation therapy). For example, inhaled pharmaceutical administration requires tiny droplet sizes (1-5  $\mu\text{m}$ ) to reach the respiratory tract, whereas large droplets end up in the mouth or throat, and ultra-fine particles can enter the circulation, accumulating and triggering a range of health issues. When spraying pesticides on farms, droplets must be small enough to cover the crop and not float into the air. Droplets should be large enough to coat the tablets but not so large that they are wasted in the pharmaceutical spray coating process. In advanced or additive manufacturing, small droplets frequently result in improved resolution and thin film uniformity. As a result, atomizer performance depends on regulating and understanding droplet size distribution processes.

To influence droplet formation and properties, a typical spray device uses pneumatic, piezoelectric, electrostatic, thermal, or acoustic actuation. These current strategies are successful in specialized applications but expanded application to another sector poses obstacles. Thermal inkjet, for example, cannot be utilized or used in biomedical applications such as processing bio samples due to the likelihood of thermal deterioration and limited lifetime related with resistor heater burnout. Similarly, pneumatic atomizers cannot be utilized for inkjet printing owing to the inability to regulate each droplet, its size, and homogeneity, and it is impossible to adjust the geometry of the pneumatic device as required, thus customization is not feasible. The majority of applications need small droplets (1-30  $\mu\text{m}$ ) with extremely tight control of droplet sizes, hence the overarching objective for designing new atomizers is to eliminate or diminish big droplets ( $>30 \mu\text{m}$ ) and ultra-fine droplets (less than 1  $\mu\text{m}$ ). In some applications, atomization of a wide spectrum of liquids with low power consumption is critical, but droplet size suffers as a result. Simplicity, operational robustness, fluid range, and minimal fabrication cost are all desirable.

The variety of working fluids with various qualities is an important consideration when selecting a device for a certain application. Drug delivery applications, for example, deal with low viscosity pharmaceuticals and require small droplet sizes and dispersion, but biofuels for combustion in energy-conversion devices are viscous and do not require controlled droplet distribution. As a result, every application deals with a working liquid that has distinct needs, and as a result, the appropriate device is used while other characteristics are sacrificed. The goal of the work presented here is to bridge the gap and create a device that allows us to have more control over the types of liquids we use, as well as droplet sizes and distribution. The current study focuses on a novel piezoelectrically powered, microfabricated atomizer that

generates droplets using a membrane with aperture resonances in the 100kHz range. This technology addresses the major issues associated with existing technologies, such as the inability to manufacture consistent sub-5 $\mu$ m diameters with low power consumption, the flexibility to vary output by changing nozzle sizes, pitch, and other characteristics, and the cheap fabrication cost. This thesis study comprises device fabrication, experimental characterization, and finite element modeling of acoustics and fluid mechanics to better understand device functioning. This also entails being acquainted with the device's shortcomings and overcoming them in order to obtain improved atomizer functioning.

Market size for fine aerosol applications is expected to experience a 6.4% CAGR between 2020 and 2030, to reach \$149 billion in 2030 from \$81.8 billion in 2019. Therefore, effective implementation of atomization method is a very important.

*This thesis introduces the concept of direct integration of a microheater with a MEMS-based vibrating mesh atomizer to increase the performance and ability to atomize viscous fluids in applications such as biology, chemistry, and electronics.*

## **1.2 Challenges**

The direct integration between vibrating mesh atomizer and the commercial microheater has multiple challenges. Few of them are explained below:

Since the device under consideration in this study is not commercially available, a thorough knowledge and creation of the single device is necessary before moving on to the final aim.

The commercially available microheaters and MEMS vibrating mesh atomizers are stand-alone devices. Their direct integration is difficult to put together because the electrical connections and assembling the microheater so that the working fluid heats up enough to lower the viscosity are some of the concerns that could result in liquid waste, human intervention,

and affect the device's performance. Improper integration might cause overheating, and direct contact without insulation could cause thermal interactions between the liquid and the resistor, releasing hazardous chemicals that are inappropriate for biological applications and vulnerable. As a result, the microheater must be designed and fabricated to satisfy the design specifications, as well as integrated and tested in conjunction with the MEMS atomizer. To address these difficulties, the research focuses on the proper design, manufacture, and characterization of separate devices, which are then combined to operate as a unit.

### **1.3 Background**

Atomization is the process of disintegration of liquid into spray drops by disruptive forces acting on the liquid. It is a two-step process including primary and secondary atomization, with the former occurring near the orifice of the nozzle where liquid sheet is broken into droplets by overcoming surface tension, viscosity, and inertial forces, and the latter occurring when droplets are further formed by shearing effect of air flow. Atomizers are devices that use a bulk liquid supply to produce micro-droplets or ultrafine sprays of liquid. Atomizers, also known as aerosol generators, are widely utilized in a variety of applications, including respiratory medication treatment, additive manufacturing, mass spectroscopy, deposition of doped polymers and dielectrics, spray coatings, neonatal humidifiers, insecticides, and many more. To improve efficiency, several types of atomizers are used in each application, depending on the droplet size distribution requirements. Different methods, such as pressure, pneumatic, ultrasonic, mechanical, and thermal atomizers, can be used to create mist or spray droplets.[5-7].

### 1.3.1 Atomizer Technologies

1. Pneumatic Atomizer also known as jet atomizer shown in the figure 1.1(a) is the first and old method invented in 1940's. This method employs a pressurized gas or electrical compressor to drive a jet of air through a nozzle, breaking the fluid into droplets. In this sort of technique, controlling the droplet size range is tough. The size range of generated aerosols is limited by the process of bigger droplet particles striking the baffle and falling back into the chamber. Working fluid adheres to the baffle as a result, resulting in waste and contamination. According to research, just 12 percent of the medicine enters the lungs, making these aerosol generators ineffective for drug delivery applications. Because compressed air is required to form an air jet, it is massive and requires an electrical or battery-operated compressor, making it immobile.

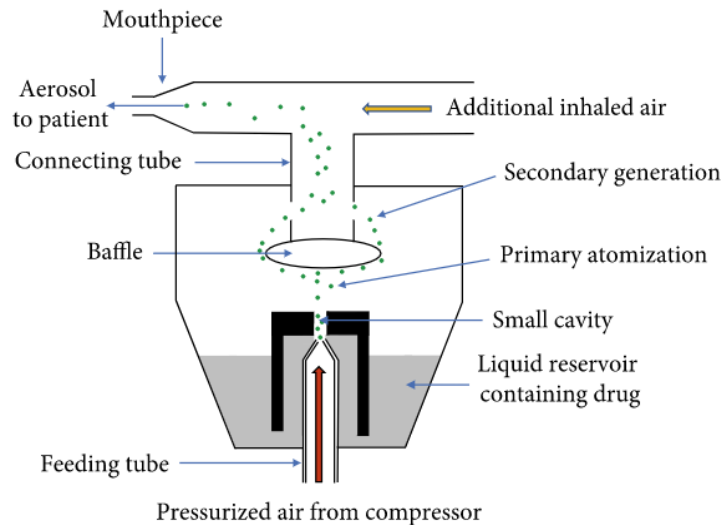


Figure 1.1 – Schematic of working principle of a jet atomizer[8].

2. Ultrasonic atomizer invented in 1960's uses a piezoelectric transducer and horn which vibrates at high frequency to generate polydisperse aerosol as shown in figure 1.2(b). Ultrasonic atomization is the ejection of droplets from a thin liquid layer formed on an ultrasonically vibrating surface. With no moving parts or heavy setup, the surface is a

piezoelectric vibrating disk powered by electrical energy, resulting in a low-energy gadget. The ejection of droplets is based on a combination of two processes: the capillary wave and the cavitation hypothesis. The capillary wave theory considers the generation of visible crests and troughs on the vibrating surface, whereas the cavitation hypothesis considers the formation of cavities in the liquid layer on the vibrating surface that collapse to generate droplets near the surface. Typically, a piezo device is put at the bottom of the container to create high frequency waves that propagate upwards into the liquid, and these generated waves have enough energy to overcome the liquid's surface tension and form droplets[5]. The wavelength is influenced by the frequency of the actuator and the characteristics of the liquid. Traditional ultrasonic aerosol generators are quieter, but they are also more costly, have a low output rate, are inefficient for high viscosity fluids and suspensions, and have residue formation and sensitive material degradation issues.

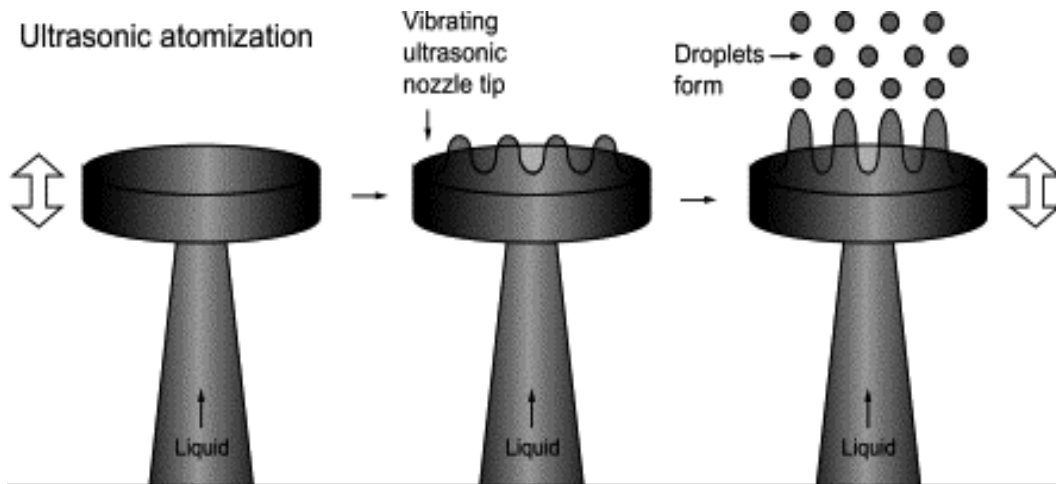


Figure 1.2 – Schematic of working principle of an ultrasonic atomizer[9].

The two methods discussed above have several drawbacks such as high-power consumption, requires number of components such as nozzles, compressed air, tubing, baffles which makes them bulky and less portable, less control on droplet size, limitation to only liquids with low viscosity, low transport factor, use of air streams, clogging. Also, piezoelectric crystal in

ultrasonic atomizer tend to generate heat that may destroy heat sensitive liquid and are unsuitable for aerosolization of suspensions[10].

3. Vibrating mesh atomizers was introduced in early 2000s for drug delivery as an advancement of ultrasonic atomization method with improved efficiency, speed of atomization, controlled droplet size, low power consumption and device handling[11]. It is also known as one of type of ultrasonic atomizer that consist of vibrating membrane or mesh with multiple apertures. These atomizers are said to have improved control over droplet dispersion and droplet size consistency. It is depending on the mesh or nozzle dimension while avoiding shear forces or excessive temperatures in the working fluid. For biomedical applications such as drug delivery purpose, it is efficient to produce droplets in range of 1-5 $\mu$ m which penetrates drug deep into the lungs while using the minimal volumes and hence doesn't waste the drug. Due to the absence of a baffle element in this device (responsible for residual losses) and the high output of the medicine with a short time to atomization, it obtained patient satisfaction. Because vibrating mesh atomizers do not require a large setup, they are quiet and can be made small and portable. These atomizers do not heat up during atomization [12] and have shown ability to atomize suspensions [13], liposomes [14] and nucleic acids[15]. Vibrating mesh are divided into two categories – Active and Passive. Active vibrating mesh devices (e.g., Aeroneb Pro) shown in figure 1.2 consist of a plate with 1000 apertures and a vibrating actuator which contracts and expands on the application of electric current. And Passive vibrating mesh device (e.g., Omron MicroAir NE U-22) consist of perforated plate with a vibrating piezoelectric crystal attached to the transducer horn. Induced vibrations in the perforated plate results into the extrusion of liquid through the holes and generates aerosol [16]. The current commercially available vibrating mesh atomizer employs many bonding

components that are manufactured using regular manufacturing techniques. Holders, washers, piezoelectric rings for actuation, laser drilled or electroformed metal membrane with perforations, and bonding adhesives are examples of components. This makes the entire manufacturing process exceedingly complicated and expensive, and the failure of a single component leads to the failure of the entire device, resulting in a poor yield. The manufacturing method restricts the form, size, and hole pitch, hence limiting the output rate. Any change or modification, such as hole size, pitch, material, and so on, is difficult to implement and does not allow for improved functionality and customization.

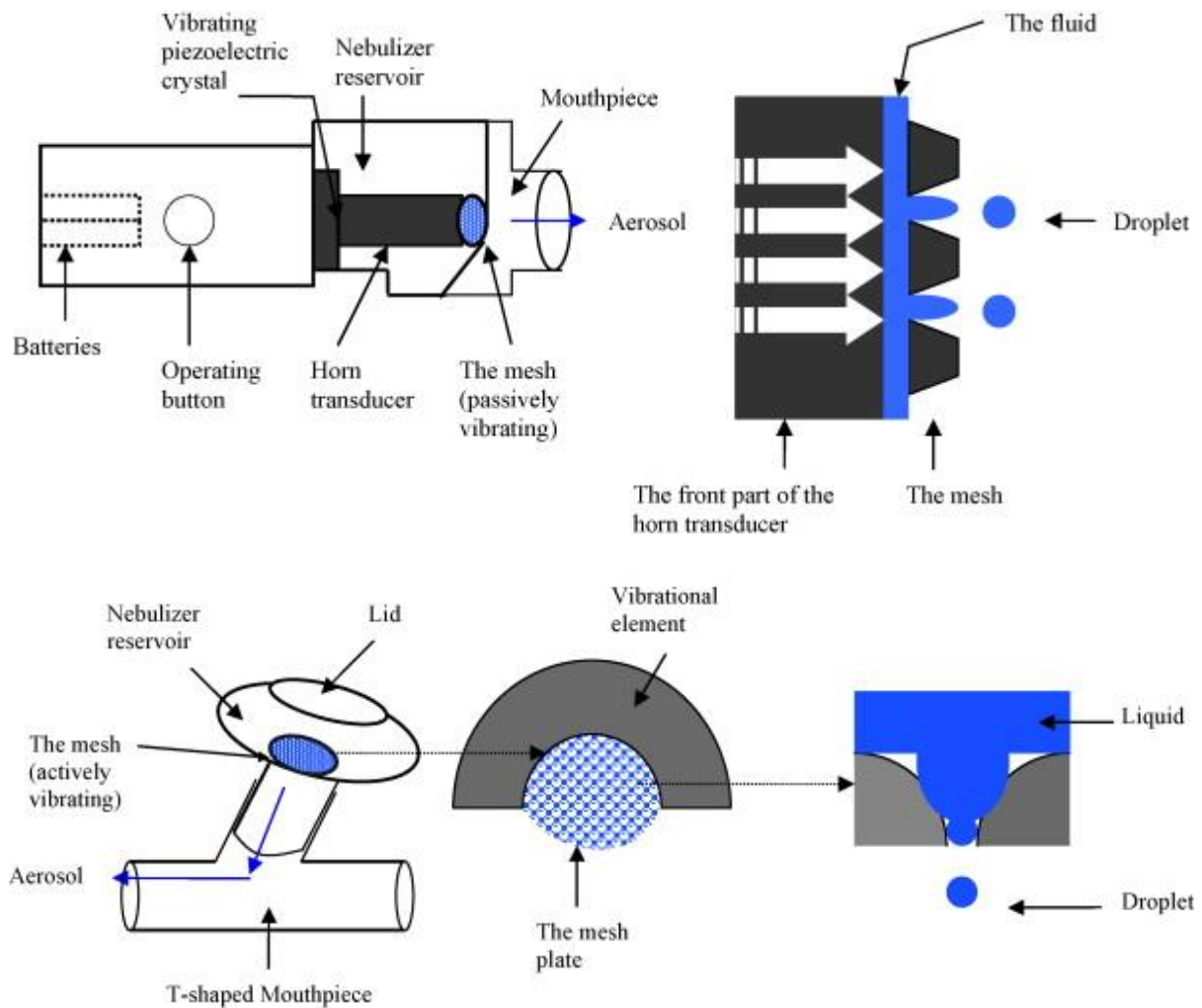


Figure 1.3 – Schematic of (a) passive type atomizer – vibrations of the piezo crystal are transmitted through transducer and passed to the mesh and (b) active type atomizer – vibrating element is surrounding the mesh at the center [17].

MEMS vibrating mesh atomizer was introduced in 2016 [10] for drug delivery. MEMS based device has silicon membrane mesh fabricated using semiconductor processes. This silicon-based atomizer has series of advantages over existing technologies such as low power consumption, good control over the aerosol size and distribution, high yield, possibility of atomizing viscous liquids and high efficiency. Method of manufacturing of these devices are based on microelectromechanical system fabrication techniques, hence, are cheap.

### **1.3.2 Applications of VM technology**

(I) Medication Delivery — This technique has the potential to be employed in a variety of drug delivery applications, including asthma treatments, medical marijuana, CBD oil, and dry powders. Aerosol size is crucial because droplet size influences aerosol deposition in the respiratory tract[18]. The VM atomizer can atomize tiny quantities and generate more droplets with sizes ranging from 1 to 5 $\mu\text{m}$ , allowing the medicine to penetrate deeper into the lungs[18].

(II) Additive Manufacturing - Additive manufacturing offers a wide range of applications and a developing industry, but the fundamental challenge is material restrictions. Most materials need heating, which degrades the material and is restricted to materials with low melting points. Furthermore, the present additive manufacturing atomization technology has poor droplet dispersal ( $>10\mu\text{m}$ ), limiting printing at small scale or high resolution. To improve resolution, a vibrating mesh atomizer can create smaller droplets.

(III) Spray Drying - Spray-drying is a one step process of conversion of liquid into dry particulates used in chemical, food and pharmaceutical industry due to high flexibility to

control particle size [19]. Most of the liquids are suspensions with high viscosity and desired smallest formulations droplet size is 1-10 $\mu$ m so, VM atomizer is capable of producing smaller droplet size and needs the advancement to atomize working fluids[20].

(III) Humidification Application - In some sectors, it is critical to maintain a consistent room state for particular processes. This prevents dry conditions from causing instrument damage. Humidifiers are also used in home settings to make rooms more pleasant. The VM atomizer produces and ejects droplets quietly and economically.

(IV) Fuel Injection - This technique might be beneficial in fuel injection, where new combustion engine designs could benefit from atomized micro-sized droplets, resulting in more efficient engines that could help remove polluting diesels and complement the electrification hybrid trend. The current approach uses big droplets and has poor droplet dispersal. The VM atomizer could create smaller droplets and improve dispersion. The VM atomizer has a higher output rate since the atomization process does not halt or slow down, unlike ultrasonic atomizers, which cannot manage high fuel flow rates. [21].

(V) E-cigarette – E-cigarette vaporization mechanism used by current devices is heating metal coil and it creates potentially toxic byproducts such as formaldehyde, acrolein etc. known to produce cardiovascular and respiratory disease. Furthermore, maximum droplets produced are in range of 100-200nm in size which can enter bloodstream and cause further potential health risks. VM atomizer has potential to control droplet size on the order of 0.5-2 $\mu$ m, preventing the particles to enter bloodstream.

## 1.4 Literature Review

Piezoelectric injection and atomization find its applications in wide range such as inhalation therapy, dust collection, precise surface coating, 3D prototyping and many others. The micron size droplet formation ability with stable injection comprised a development direction in this field.

An atomizing film with micro-tapered apertures that uses high frequency piezoelectric ceramic ring to drive the dispenser was invented by [22] to solve the problems such as high-power consumption, large droplet size and high dispersion degree effectively[23]. Then, research on these types of atomizers gained attention by many researchers. A stationary vibrating mesh atomizer actuated by piezoelectricity to improve droplet size, consume less energy and have better control on atomization process[24]. Then, micro-cone hole type device where holes were machined in the metal plate with no liquid chamber to simplify the structure of the atomizer driven by piezoelectricity was then designed to further minimize droplet size range for analyzing biomedical sample[25]. [26] developed a piezoelectric atomizer with a shaft activated by a flexing transducer to create atomization, and the atomization performance was validated by the creation of droplets with various working media such as water, ink, powder, and photoresist[27]. Atomizer with electroformed Ni-Co cymbal shaped high power driver where the actuator is piezoelectric ring shape and cymbal shape nozzle plate was studied by [28] to reduce the droplet to ultra-fine droplet distribution with median aerodynamic diameter of  $4.07\mu\text{m}$  with the rate of  $0.5\text{mL}/\text{min}$  (80% higher atomization rate than flat nozzle plate) with efficiency higher than traditional devices. Performance study of the atomizer such as ability to form droplets and identifying mass median aerodynamic diameter, output rate and operating frequency was conducted in [29]. The stable atomization rate is very important factor that plays

a vital role in the application and promotion of vibrating mesh atomizer and thus [30] studied the influencing factors of the atomization rate in this type of atomizer. Researcher in [31] subjected micro tapered atomizers to spray cooling and concluded that the spray cooling efficiency is related to atomization rate and thus to aperture diameter. Piezo ring on chip with micro tapered aperture atomizing film was invented by was applied to mass spectrometry and to deposit the sample on substrate by spraying[32]. In various applications such as spray cooling[33], inkjet printing[34], inhalation therapy[35] and many other aspects, atomization rate droplet size are the important parameters to consider. Up until now, the influence of voltage, frequency and different mediums has been considered and study on viscous fluids are usually ignored. It is necessary to investigate the factors involved in the working of the atomizer and modify it to widen the area of applications.

The piezoelectric actuator vibrates at a specific frequency with supplied voltage and effects output rate. Various properties of the device such as mesh hole size, pitch and number of holes are studied to enhance the atomization characteristics of the atomizer[10, 28, 29, 36]. The atomizer vibrates most at resonance frequency and output rate peaks when the operating frequency is close to resonant frequency and the output rate increases with increasing voltage at a fixed frequency[37]. Characterization of custom made vibrating mesh plates was performed to investigate the critical parameters affecting the output characteristics and concluded that pitch has no effect on produced droplet size, concentration, or distribution, but is affected by operating resonance frequency by a small amount and that delivery method using cotton wick is more effective for optimal atomization than syringe pump[38]. Many investigations have been conducted using commercial VMA on the process of droplet production and separation[39], the influence of driving frequency and voltage on its

performance[40], and the effect of vibration characteristics[41] using water as working medium. Previous studies have focused on the atomization performance of a stainless steel-based vibrating mesh atomizer by varying input parameters and changing the liquid, and conclusions were drawn based on the output obtained. However, these conclusions do not fully apply to MEMS VMA because it has a different membrane material and nozzle shape, even though they work on the same principle. Then, the comparison of the two devices was performed in terms of droplet distribution and concluded that MEMS VMA has narrower distribution and more uniform droplet produced in comparison to metallic VMA for range of liquids and observed that both the VMA's were incapable of perform atomization for viscosity above 3cPs[42]. [42, 43] demonstrated that application of MEMS VMA to spin spray deposition method with liquid viscosity below 2cP efficiently. The effect of fluid physiochemical properties on fluids with a wide range of viscosity, surface tension, and ion concentration was investigated in [17] using different types of commercially available vibrating mesh atomizers for drug delivery and it was discovered that the mesh atomizers were unsuitable for delivering viscous liquids, and nebulization was infrequent or stopped at >1.92cP. The existing study on mesh atomizers indicated that the device does well with droplet size distribution and is only capable of working with low viscosity liquids, which is one of the primary drawbacks. Total output, output rate and generation of smaller droplets are important parameter for many applications. No study has been performed on atomization of high viscous fluids with vibrating mesh atomizer due to its limitation and hence, fabricating a device capable of atomizing viscous fluids is the concept of our study. We focus on fabricating the atomizer, characterizing it for various liquids with range of viscosity and then integrating it with microheater to increase the range of liquids for wide range of applications.

The present work reports a modified vibrating mesh atomizer based on principle of lowering the viscosity of working liquid with the help of microheater device integrated with MEMS mesh atomizer. The main goal is to investigate the performance of a MEMS vibrating mesh atomizer, research the comparison with existing technology, and afterwards improve on the shortcomings of the standalone unit by effectively integrating a microheater device to make it suitable for a wide range of liquids. These devices are capable of atomizing low viscous fluids with controlled droplet size but is not able to atomize high viscous fluids. So, the concept of adding electrothermal microheater to atomize viscous fluids. Microfabrication methods also provides flexibility to manufacture both the device separately and then integrate them to function as one component or device. Using microheater that provide low temperature heating ( $<100^{\circ}\text{C}$ ) heating in order to reduce the liquid viscosity to enable atomization. A study in [44] developed atomizer with numerous cavities or apertures with microheater based on principle of thermal bubble actuation for viscous fluid for aromatherapy. This supports the concept of monolithic integration of microheater with the vibrating mesh atomizer for viscous fluids. Microheater operating temperature which is dependent on various parameters can be easily controlled.

## **1.5 Market and Scope**

It has been 28 years since the launch of first vibrating mesh atomizer by Omron NU-U03 in 1993 where this technology had to compete the already existing technologies like jet and ultrasonic atomizer. At that time, jet atomizer dominated 73% of world market due to decreasing prices and increases occurrences of respiratory diseases. Mesh atomizer was initially limited in the treatment of asthma and chronic obstructive pulmonary diseases, due to low cost of drugs. According to recent market research data, the mesh market is growing at a

third the rate of jet atomizers. Estimates showed a decrease in the selling price of all types of atomizers, with the mesh type showing the most decline. The decrease in mesh atomizer pricing is most likely due to greater competition and low jet atomizer prices. Despite this, further study is needed on mesh cleaning and clogging avoidance, as well as the possibility of atomizing high viscosity fluids of varying complexity for varied applications. The market is likely to expand in general. Device costs, improved quality, capacity to atomize a wide range of liquids, smaller, lighter, and more dependable devices are all key factors[45]. Recent market research reports indicate that the aerosol market is \$81.8 billion market in 2019 and expect the estimated compound annual growth rate (CAGR) of 6.4% till 2030. The global vibrating mesh atomizer market is expected to grow from \$289.9 Million in 2018 to \$ 591 Million by 2025 with CAGR of 10.76%.

Choice of liquid and device parameter that can be employed for different application area is most important.

## **1.6 Objective and Contribution**

In this thesis, the main objective is *to design and fabricate a silicon based vibrating mesh atomizer enabled with microheater to atomize high viscous fluids*. The contributions in this thesis can be summarized as follows: (1) Finite element modelling of vibrating mesh atomizer to understand the impact of its geometrical parameters, (2) Microfabrication process and experimental characterization of vibrating mesh atomizer performance and comparison with the metallic VMA (commercial device), (3) FEM and microfabrication of microheater (4) Integration of vibrating mesh atomizer with microheater (5) Application of vibrating mesh atomizer in different fields. The following provides more details on the contribution.

### **1.6.1 Numerical Simulations of atomizer to understand the impact of its geometrical parameters**

Chapter 2 presents the numerical modelling of Vibrating mesh atomizer to understand the influence of device design parameters. The simulations involve structural analysis, fluid flow analysis. Parameters such as mesh hole size, membrane diameter and piezoelectric ring thickness were considered in structural analysis to study the operating frequency range and deflection of the membrane. In Fluid flow analysis, parameters such as nozzle design, nozzle diameter and viscosity of liquid are considered. Two phase flow is used to study these parameters.

### **1.6.2 A Microfabrication process of atomizer and experimental Characterization of Vibrating mesh atomizer performance**

Microfabrication process to form the Silicon based vibrating mesh atomizer is presented in chapter 3. The vibrating mesh atomizer device is characterized on the basis of aerosol generation. This is achieved by identifying the operating frequency range and mode of the device. This is an importance performance parameter, especially for applications that require consistent aerosol volumes. Droplet producibility is very important for the device and is determined by droplet size distribution. Liquid viscosity is a major factor to predict the scope of applications from materials perspective. A comparative study of microfabricated device and stainless-steel based atomizer device is performed to evaluate the advantages of this technology over existing one.

### **1.6.3. FEM and microfabrication of the Microheater**

In chapter 4, heat transfer analysis is used for microheater design parameters for temperature study. Heater design, material, metal thickness and input supply voltage are the parameters

considered for temperature study. The results from all the simulations are then used to draw conclusions and design recommendations for atomizer and micro heater and then later Fabrication process of the microheater is discussed. Optimized device design from simulations is chosen for fabrication. Microfabrication process is necessary to enable the integration with the vibrating mesh atomizer to form a single integrated device for high viscous fluids. The device design limits the contact or direct exposure of fluids with the metal heater in order to avoid any chemical reaction between metal and liquid and effect on the fluid property. Characterization of the microheater is involved in further sections to study the performance with respect to temperature profile and response time.

#### **1.6.4 Integration of modified device and its performance characterization**

Integration of the atomizer with microheater into a single component is a critical step as it enables operation of two functions at a time – viscosity reduction of the liquid in contact with the electro heaters and aerosol generation with the mesh membrane. The integrated device assembly is demonstrated in chapter 5 and is tested with range of liquids with different physiochemical properties.

#### **1.6.5 Initial Demonstration of developed Vibrating mesh atomizer in different fields**

The ability of vibrating mesh atomizer to be implemented for different applications. Examples showing the device suitability is presented here. This includes application of MEMS VMA for spin-spray deposition of Spin on glass, SU-8 for 3D microstructures and conformal coating presented in chapter 6. Spray cooling is another application where the fabricated device showcased its better cooling performance over the commercial VMA.

#### **1.6.6 Conclusion and future work**

Chapter 7 entails the conclusion of the thesis work and proposes the future work. This is a discussion for things that can be considered in future to enhance the performance of the device in terms of added functionality.

## **1.7 Summary and report Organization**

This chapter begins with an overview of the atomization process then continuing on to the many types of atomizers and the history of each technology now in practice as background of the atomizers. Previous research work has been discussed to study the various aspects of the devices working on the same principle. This literature study aids in the identification of the technology's issues and drawbacks, as well as the opportunity to target or work on the gap. The motivation behind this work, objectives and potential applications have been also presented. The outline or the organization of the thesis has been discussed in this chapter which gives better understanding of each section and how they relate to achieve the overall goal.

## CHAPTER 2

### FINITE ELEMENT MODELLING OF VIBRATING MESH ATOMIZER

The design optimization of the atomizer aims to improve the device performance and enable the atomization of an extensive range of materials. It requires the understanding of the impact of design parameters on performance. For the design choices, different simulation modules are required such as structural analysis for membrane, Fluid flow analysis for different nozzle shape to define droplet formation. This chapter is dedicated to the numerical simulations of important design parameters to allow the interpretation of results and result in an optimized atomizer design. For the application of FEM, the commercial software package of COMSOL Multiphysics 5.6 is used. COMSOL is a general-purpose platform for modelling and simulating physics-based problems based on advanced numerical methods.

#### 2.1 Working principle

The MEMS vibrating mesh atomizer in this study uses a silicon-based circular membrane with nozzles and a piezoelectric ring (lead zirconate titanate) to create the actuation mechanism. The atomizer consists of a mechanical vibrating membrane with micro-size perforations shown in Figure 2.1. The silicon mesh membrane and the piezoelectric ring are tightly bonded to the stainless-steel holder. During operation, the bottom surface of the perforations is in contact with air, and the liquid is in contact with the top surface of the mesh, which vibrates out of the plane (vertical direction) by vibrating the PZT actuator driven by AC voltage. The inverse piezoelectric effect drives the atomizer, leading to atomization and ejection. During atomization, pressure on the top surface increases caused by the volume change in the apertures, and liquid flows from a high-pressure region to a low-pressure region caused by the

membrane's vibration when positive pressure is applied during forwarding vibration. Then the liquid is pinched off and adhered to the wall by capillary force during backward vibration. The liquid flows from the larger diameter end to the tapered or smaller end.

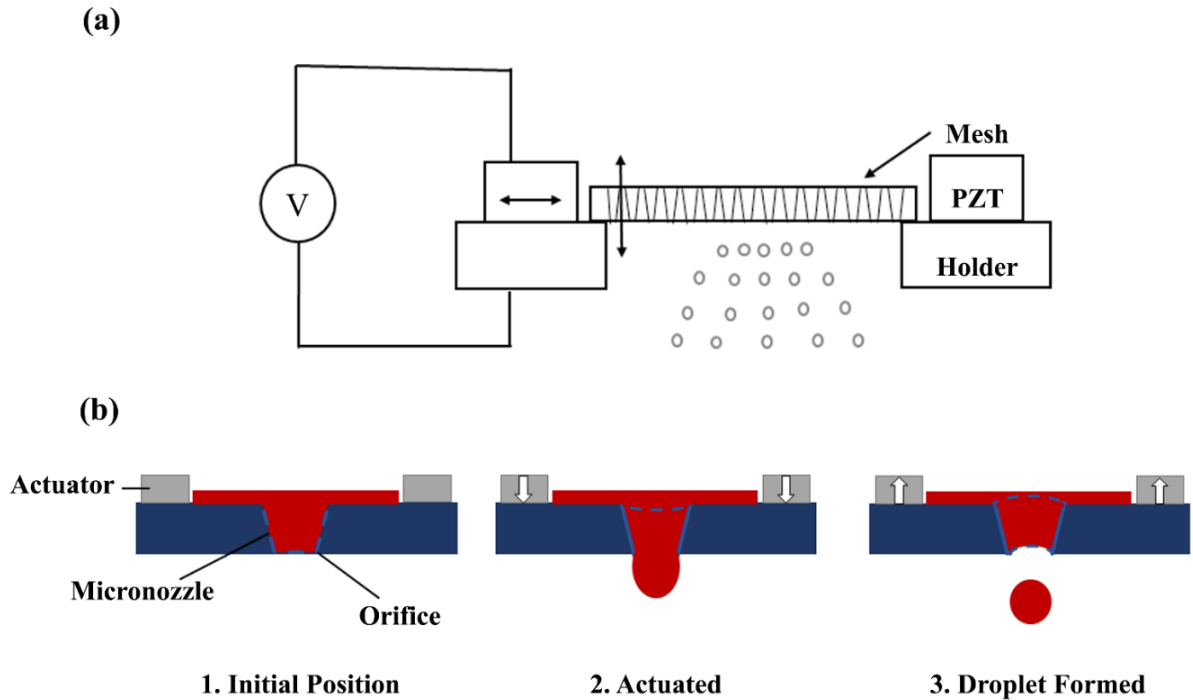


Figure 2.1 – Schematic of (a) Vibrating mesh atomizer, (b) cross-sectional view of dispenser structure and working concept.

The analytical solution for to calculate the natural frequencies of a membrane using thin plate theory is given by [46]:

$$f_{mn} = \frac{\alpha h}{2\pi R^2} \sqrt{\frac{E}{12\rho(1-\nu^2)}} \quad (1)$$

Where R is the radius of the circular membrane with thickness h,  $\rho$  is the density, E is the young's modulus,  $\nu$  is the Poisson's ratio, and  $\alpha$  is a constant that depends on the number of nodal diameters. Figure 2.2 demonstrates the analytic solution of the vibration of a solid

circular plate with no external load and clamped edge constraint as modeled by equation 1 concerning the membrane's thickness, material property (Young's Modulus), and membrane radius.

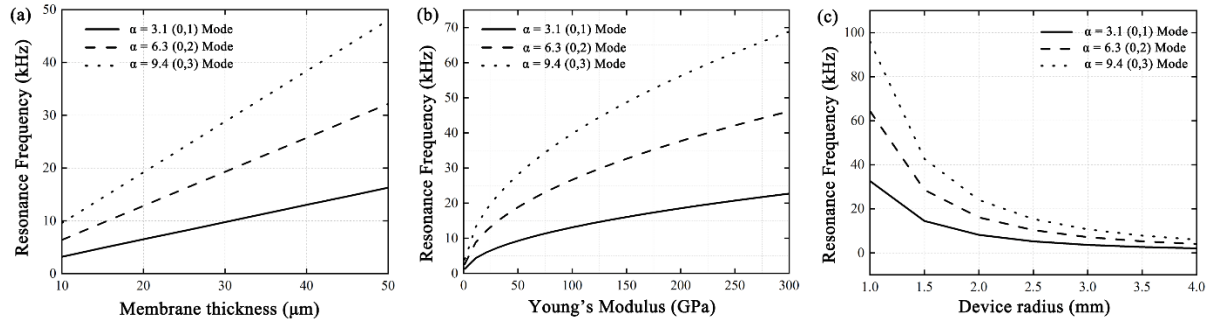


Figure 2.2 Analytic solution according to circular plate theory for varying (a) thickness, (b) Young's Modulus and (c) radius.

## 2.2 Structural Mechanics Analysis

The structural mechanics' module is employed in this study to identify resonant frequencies and modes of operation. Identification of deformation of the membrane at different frequencies at variable voltage supply is also crucial to knowing the velocity and acceleration profile of the membrane. Solid Mechanics and Electrostatic Physics are employed here to apply boundary conditions. The piezoelectric effect and electromechanical forces successfully couple them. The FEM study with solid mechanics and electrostatics aims to understand the effects of design parameters on resonance frequency and corresponding displacement.

### 2.2.1 Eigen Frequency and Piezoelectric effect governing equations:

Eigen frequencies are distinct frequencies at which a system tends to vibrate. A structure deforms into a similar shape known as eigen modes when vibrating at particular eigen frequencies. An eigen frequency analysis solves for the eigen frequencies and the shapes of the

corresponding modes but not the amplitude of the deformation. For deformation study, electrostatics physics used over a range of frequency.

The system with multiple degree of freedom can be characterized by:

$$M\ddot{u} + C\dot{u} + Ku = f(t) \quad (2)$$

Where M is the mass matrix, C is damping matrix and K is the stiffness matrix and the degree of freedoms is in row vector u and external force applied onto the system is f(t).

The free vibration is given by:

$$(-\omega^2 M + i\omega C + K)ue^{i\omega t} = 0 \quad (3)$$

Then, the eigen values are solved by:

$$\det(-\omega^2 M + i\omega C + K) = 0 \quad (4)$$

The eigen frequency for continuous structures such as membrane with T as in-plane force per unit thickness and  $\mu$  as mass per unit area is:

$$\omega_{mn} = k_{s,mn} \frac{1}{size} \sqrt{\frac{T}{\mu}} \quad (4)$$

### *Piezoelectric Effect*

The piezoelectric effect refers to a change in electric polarization when certain materials are subjected to mechanical stress, and it is demonstrated as a transfer of electrical to mechanical energy or vice-versa. The direct piezoelectric effect is an electric polarization in a particular direction when a crystal is deformed. It is proportional to deformation and causes an electric potential over the crystal. And the inverse piezoelectric effect is the opposite of the direct impact. It means that an application of electric potential induces some crystal deformation.

Relation between stress, strain electric field and displacement is given by:

Stress-charge form,

$$T = c_E S - e^T E \quad (5)$$

$$D = eS + \varepsilon_S E \quad (6)$$

Stain-charge form,

$$S = s_E T + d^T E \quad (7)$$

$$D = dT + \varepsilon_T E \quad (8)$$

Where  $S$  is structural strain and  $T$  is stress.

The equation of piezoelectricity combines the momentum equation with charge conservation equation of electrostatics is given by:

$$\nabla \cdot D = \rho_V \quad (9)$$

Where  $\rho_V$  is the electric charge concentration. The electric field is computed from electric voltage  $V$  as:

$$E = -\nabla V \quad (10)$$

Where  $V$  is the electric potential.

### 2.2.2 FEM Simulation Model

The device is modelled as a 3D asymmetrical model shown in figure 2.3. Simulating in 3D provides a better visualization of the device or membrane's behavior and shows the model's reality. This model includes 5mm diameter membrane with 1000 circular apertures of 40 $\mu$ m diameter, a 500 $\mu$ m thick holder onto which the device sits and, a 500 $\mu$ m thick lead zirconate titanate ring. Silicon is the material selected for the membrane and stainless steel as the holder. The thin layer of aluminum is set as the top and bottom electrodes for the PZT ring.

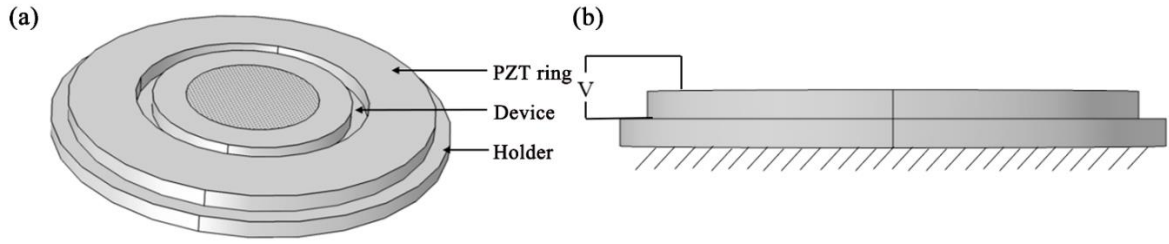


Figure 2.3 – Schematic of (a) Meshed 3D simulation model, (b) Fixed boundary, (c) model with PZT ring and electrodes, (d) zoomed view of top and bottom electrode.

Table 2.1 - Material properties used in finite element modelling.

Material	Young's Modulus (GPa)	Density (Kg/m <sup>3</sup> )	Poisson's ratio	Diameter ID/OD (mm)	Thickness (mm)
Silicon	170	2329	0.28	5	0.025
PZT	115	7500	0.31	16/6.5	0.5
Aluminum	70	2700	0.35	16/6.5	0.0001

*Boundary Conditions:* The boundary conditions with solid mechanics and electrostatics physics are fixed constraint on the boundary of the stainless-steel holder as seen in figure 2.3. The piezoelectric material is chosen from material models. The electrostatics module is used to supply voltage to one of the electrodes sandwiching piezoelectric ceramic and other one is grounded. The two modules are coupled together in Multiphysics using piezoelectric effect and electromechanical forces to study the eigen frequencies, modes, and deformation of the membrane.

*Meshing:* The meshing of the model was performed using free tetrahedral elements. Upon mesh independent study, the saturation of resonance frequency above 50,000 elements and any further change in number of elements did not make any difference in frequency further. So, for all the simulations, 150,000 elements with a minimum element size of 2 $\mu$ m is used. Figure 2.4 demonstrates the mesh independent study curve.

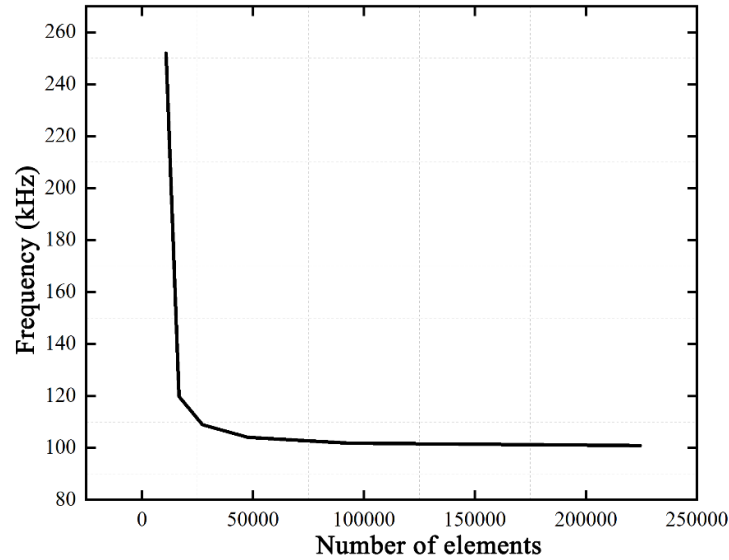


Figure 2.4 Mesh independent graph for frequency.

### 2.2.3 Eigen Frequency Modal Analysis

Eigen frequencies and mode shapes are considered when designing the device with a thin circular membrane, as they define the system's characteristics and show how it works in real life. Since our device membrane has a circular shape that exhibits many symmetrical portions, it will have multiple Eigen frequencies. Eigen frequencies and mode shapes are critical for the operation of VMA, and thus understanding how various parameters and designs can influence these is important for enhancing device performance in various applications. The first nine frequencies were simulated for the MEMS VMA device and the results are demonstrated in Figure 2.5. The first eigen mode (0,1) mode had a resonant frequency of 25.8 kHz, and the membranes deflection was out of plane i.e., perpendicular to the plane. The second mode also known as (1,1) mode had an eigen frequency of 50 kHz and produced a twisted shape rotated by 90 degrees. The third mode (2,1) mode had eigen frequencies of 82.7 kHz and a plotted shape of quadratic twist rotated by 45 degrees. The fourth (0,2) mode, cause the membrane to deflect out of plane near the center had a frequency of 101.2 kHz. The (0,2) mode has two

circular nodes one at the outside edge and one closer to the center, these result in a large velocity change near the center. The other higher order modes (3,1), (1,2), (4,1), (2,2) and (0,3) had frequencies of 130 kHz, 155 kHz, 179 kHz, 215 kHz and 230kHz. The frequency analysis FEM findings differ considerably from the analytical solution, which yielded a (0,1) and (0,2) frequency of 8.12 kHz and 16.08 kHz for the analytical model and 25.8 kHz and 101.2 kHz for the FEM for the identical membrane dimensions. The contrast between the analytical and finite element solutions shows that the membrane's extra elements and perforations have a considerable impact on the frequencies and operational parameters. As a result, analytical models are difficult to execute, and FEM is a stronger tool for understanding VMA dynamics.

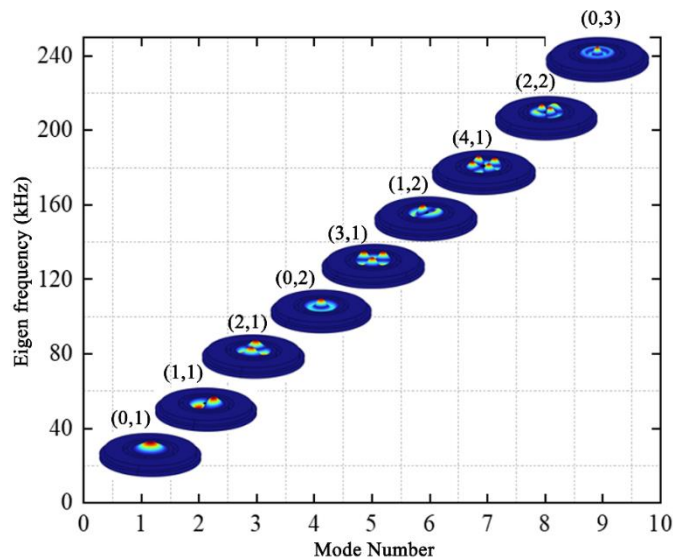


Figure 2.5 – First nine resonant frequencies with the shape mode.

The frequency spectrum curve of the vibration displacement amplitude for the simulated FEM of 3D device model is shown in Figure 2.6. The highest out of plane displacement amplitude is observed for (0,1) mode at 26kHz, (0,2) mode at 99kHz and (0,3) mode at 221kHz.

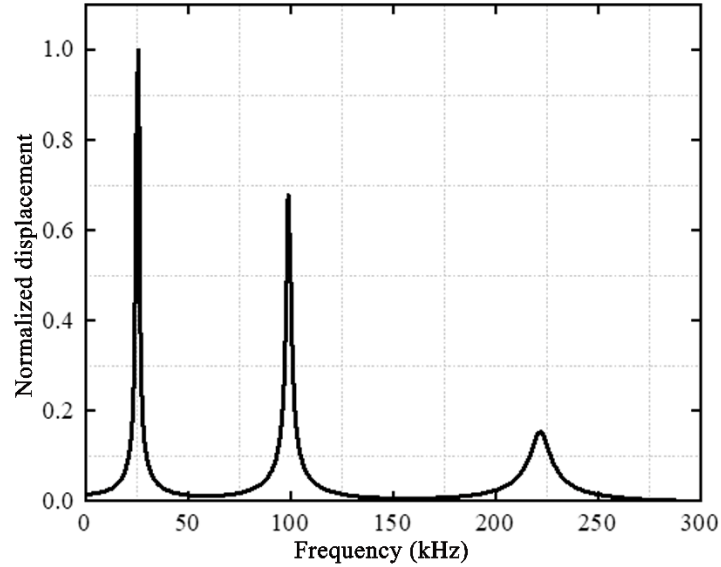


Figure 2.6 – Frequency spectrum of the normalized out of plane displacement amplitudes.

The membrane's resonance frequency is dependent on the device's design, which includes the apertures' diameter, thickness, material, shape, and pitch, as well as other limitations. Figure 2.7 demonstrates that the (0,2) mode may be changed to a higher or lower frequency by adjusting the membrane's width and thickness. A silicon membrane with a diameter of 2mm functioned in the (0,2) mode at a frequency of approximately 400 kHz. As the membrane's diameter increased, the frequency decreased, reaching 45 kHz for a 7mm membrane. The increase in frequency would result in a greater flow rate, necessitating a smaller displacement to meet the same atomization velocity threshold. Atomization of liquids with greater viscosity needs more effort to overcome viscosity and surface tension, necessitating an increase in velocity. In contrast to the diameter, altering the membrane's thickness has the opposite effect on the membrane's stiffness, resulting in higher frequency operations. For a given membrane diameter, a silicon membrane with a thickness of 10  $\mu\text{m}$  would produce a (0,2) mode frequency of 42 kHz, whereas a membrane with a thickness of 60  $\mu\text{m}$  would generate a frequency of 237 kHz.

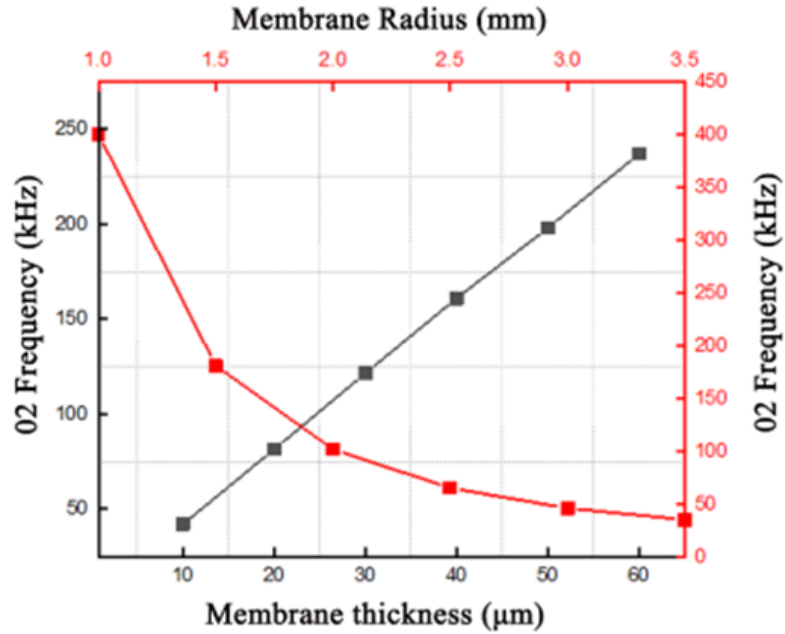


Figure 2.7 - FEM results for determining (0,2) mode resonance frequency for silicon membrane with respect to membrane thickness (black) and membrane radius (red).

As illustrated in Figure 2.8, the effects of modifying the diameter of silicon membrane VMA were examined by examining displacement at different frequency modes to establish the dominant shape mode. A membrane with a 2 mm diameter revealed that the (0,1) mode shape at 100 kHz had a substantially larger displacement than other frequency modes, which exhibited displacements on the nm scale. As the membrane's width increased, the displacement amplitude of the (0,1) mode dropped, while the amplitude of the (0,2) mode increased and became dominant. The membrane with a 6 mm diameter indicated that mode (0,2) had the greatest displacement, although modes (0,1) and (0,3) and other modes began to exhibit greater displacements. The (0,2) mode no longer had the maximum displacement for the 10 mm membrane, as the (0,3) mode operating at 36 kHz had the largest displacement and the (0,2) mode working at 16 kHz had the third highest displacement. Since the VMA operates in the (0,2) displacement mode, lower membrane diameters may be advantageous for MEMS VMA

atomizers as the (0,2) becomes the dominant displacement mode. However, as the diameter increases the dominate mode is the (0,3) mode, which has demonstrated some success at atomizing liquids [32], so if larger membranes are required the atomization process would need to operate in the (0,3) mode.

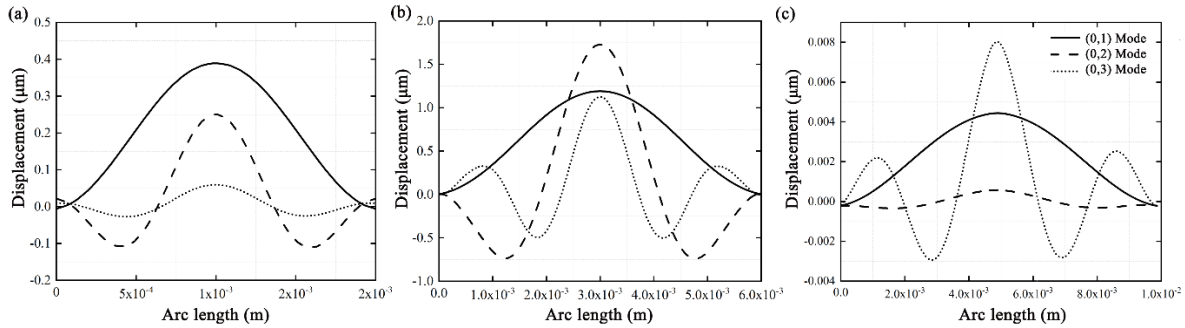


Figure 2.8 – FEM results for different frequency mode ((0,1), (0,2), (0,3)) displacement for membrane diameter (a) 2 mm, (b) 6 mm and (c) 10 mm at 100 peak to peak voltage supply.

### 2.2.4 Frequency Domain Analysis

In a frequency domain study, the response to harmonic steady-state stimulation for certain frequencies is investigated. At eigen frequency of 102 kHz or (0,2) mode, membrane out-of-plane displacement is explored. In a parametric sweep of research, an input voltage range between 10V and 100V is applied. In the physics of electromechanics, the terminal is determined by the electric potential at the top electrode (the aluminum layer at the top of the PZT ring) and the bottom electrode, which is the aluminum layer at the bottom of the PZT ring, is set to ground. Multiphysics combines electromechanics with piezoelectric effect in this instance. The model does a series of static assessments for various input voltage levels. Every sequence undergoes a certain number of iterations before arriving to convergence. The procedure is repeated for each voltage value, beginning with 10V, and ending with 100V. It was established that the atomization process of the MEMS VMA is caused by the velocity of

the membrane, which involves a combination of operating frequency and membrane displacement. The membrane displacement is determined by the mode of operation, membrane stiffness, piezoelectric actuation, and applied voltage. The displacement across the symmetric circular membrane for (0,1), (0,2), and (0,3) with varied applied voltages is shown in Figure 2.9. Mode (0,1) has the greatest amplitude of displacement near the middle of the membrane, followed by modes (0,2) and (0,3). The displacement of the central point is the greatest compared to the rest of the membrane, and its magnitude increases as the supply voltage rises. An optimal voltage supply value is established and used for design safety. In practice, a very high voltage supply is avoided so as not to rupture the membrane, since silicon is a rigid material and excessive movement tends to rupture the membrane.

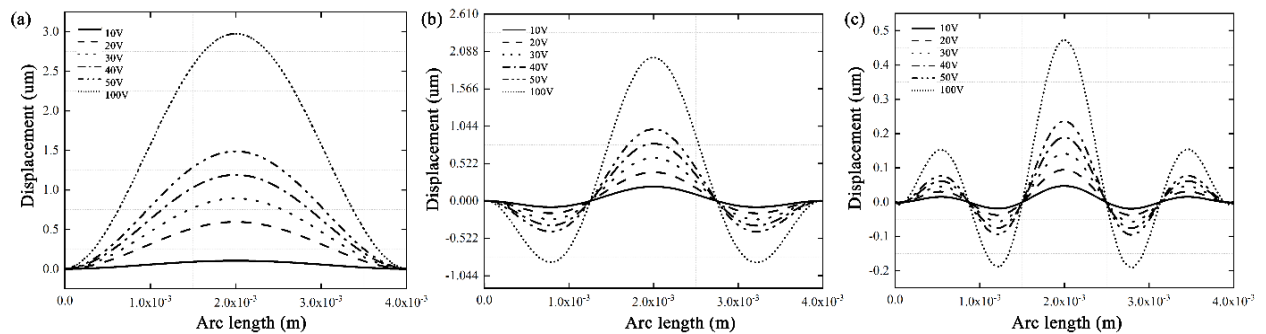


Figure 2.9 - FEM analysis of displacement across the membrane (a) (0,1) mode, (b) (0,2) mode, and (c) (0,3) mode with varying applied voltage.

The modeled atomizer device demonstrated the flexibility of altering the resonance frequency and modes by changing the physical parameters such as diameter, thickness, and membrane material. Different piezoelectric material coupled with the device impacts the displacement amplitude at the desired frequency. The membrane peak displacement, which is related to peak velocity, depends on the input voltage supply.

## 2.3 Fluid flow Analysis

The droplet formation and dispensing is a very complicated process and has been explained in various book chapters [47, 48]. When the piezoelectric actuator deforms the membrane, the fluid accelerates from broad side of the nozzle to the other side i.e., the narrow side and flow outside the nozzle. The membrane deformation and the nozzle converging profile helps the fluid to accelerate and form a droplet. In the initial stage of droplet formation, a meniscus is formed into a droplet with sufficient energy provided and in later stages, the fluids start necking and end up breaking into a main droplet and a satellite drop due to retraction of ejection cavity membrane pulls the fluid back inside the nozzle. There are many parameters involved in the process such as fluid viscosity, surface tension, pulse actuation, membrane material, micronozzle geometry. Figure 2.10 shows a drawing of dispenser with the involved components and parameters in the process that are highlighted to show the system complexity. Liquid properties also play an important role in the droplet formation and dimensionless numbers including Reynolds number (Re), Weber number (We), Ohnesorge number (Oh) are the numbers that assess the relative importance of Viscosity, surface tension, and inertia force. Reynolds number represents the ratio of inertial to viscous forces given by  $Re = \rho * V * D / \mu$  and Weber number represents the ratio of inertia to surface tension and is given by  $We = \rho * V^2 * D / \gamma$ , where  $\rho$  is the density of the liquid, V is the characteristic velocity (velocity at the exit of nozzle), D is characteristic length (Nozzle diameter in our case),  $\gamma$  is the surface tension and,  $\mu$  is the dynamic viscosity of the liquid. Both the Reynolds number and weber number is dependent on the characteristic velocity which depends on operating conditions and hence Ohnesorge number (Oh) was introduced, a dimensionless number which is independent of the velocity and relates the fluid physical properties and characteristic length.

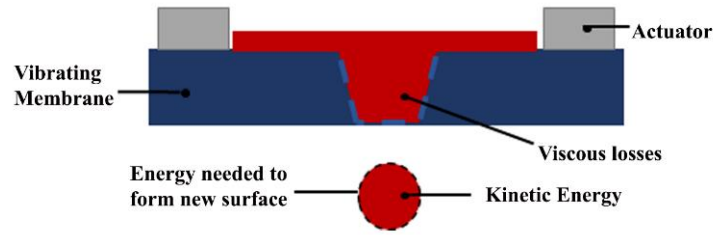


Figure 2.10 –A simplified drawing of the atomizer with examples of involved components indicated.

Three design parameters selected here for simulations are nozzle diameter, nozzle shape, and fluid properties. COMSOL Multiphysics is selected to perform these simulations with two-phase flow. The simulations are focused on process of droplet formation and diameter of ejected drop. The results from the simulations are used to draw conclusions to improve the performance of the atomizers.

### 2.3.1 Fluid-flow Governing Equations and Numerical Simulations

Numerical simulations of fluid flow in COMSOL are based on Navier-Stokes equations. For incompressible fluid flow, the Navier-stroke equation that describe transport of mass and momentum are[49]:

$$\rho \left( \frac{\partial \vec{u}}{\partial t} + \vec{u} \nabla \vec{u} \right) = -\nabla P + \mu \nabla^2 \vec{u} + \vec{f} \quad (11)$$

$$\nabla \cdot \vec{u} = 0 \quad (12)$$

Where  $\rho$  is the density,  $\vec{u}$  is the fluid velocity field,  $P$  is the pressure field,  $\mu$  is the coefficient of viscosity and  $\vec{f}$  are the other forces.

### 2.3.2 Two-Phase flow Simulations

As Navier strokes cannot be solved analytically due to its complexity, so numerical methods are used [49]. Analytical solutions can only be found for special fluid flow cases such as problem with unidirectional flow and steady state, where Navier stroke equations can be

eliminated. These conditions are not applicable to the atomizer or fluid dispenser. Atomizer has number of nozzles that means the acceleration term is non-zero as the fluid velocity changes with time. Studies shows that simulation of flow field in dispensers is difficult because of complex boundary conditions involved [50]. And due to the complexity, numerical simulation using COMSOL is chosen here.

In the atomization process, formation of droplet is a gas-liquid two-phase flow. It is difficult to trace the interface of two-phase flow. Different method such as MAC (Marker-And-Cell)[51], Simplified-MAC[52], SUMAC (Arbitrary boundary method)[53], SUMMAC (Stanford University modified MAC)[54], TUMMAC (Tokyo University Modified MAC), VOF (Volume of Fluid)[55] and LSM (Level set method). VOF and LSM are the two most commonly used approaches for interface tracking.

COMSOL Multiphysics offers wide range of simulation models as demonstration, one of the models is simulation of Inkjet dispenser. In this model, Navier-stroke equation is solved numerically. Level set method is used to describe and convect air and liquid interface. The level set function defines the ink-air interface and smoothly goes from 0, representing air to 1 representing ink. This thesis uses the similar approach. Fluid velocity function is used as the boundary condition at the inlet to produce the representative results.

### **2.3.2.1 Simulation Model**

An Axisymmetric 2D model are adopted here for problem simplification and to avoid any intensive simulation of 3D models. Using Axisymmetric 2D model means that the model is symmetric around the symmetry axis. A simulated 2D model is shown in figure 2.11 with the geometric outline of the nozzle containing the fluid-air interface.



Contour	Dimension (um)
AB	19.17
CD	1.5
AC	25
CI	100
CE	15

From previous simulations of structural mechanics, we concluded that the actuator displacement is linearly related to the applied voltage, and actuator velocity is the derivative of the displacement with respect to time. A typical sinewave form generated by the function pulse generator that is used as an input to the amplifier and the voltage that is used successfully to eject the droplets from the atomizer is shown in figure 2.12(a). Assuming the maximum actuator velocity across the membrane produce valid results and the velocity is based on the displacement at given voltage. Since the supply voltage and velocity follow the same profile similar to the pulse so, every time same amount of fluid will be dispensed during positive velocity and then retraction during negative velocity profile. And for each set of parameters, fluid velocity is assumed to be the actuator velocity. Input is the inlet velocity  $v(r)$  as the vibration velocity of the actuator. The out of plane or z direction velocity is  $v(r,t) = \sin(\omega t).v(r)$ , with  $\omega$  being the resonant frequency. The fluid velocity profile is also shown in figure 2.12(b). Maximum inlet velocity  $v(r)$  considered is 0.4m/sec during the simulations.

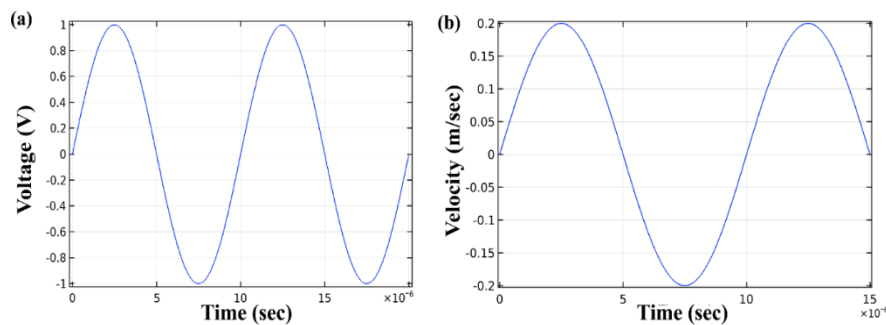


Figure 2.12 – The function generator waveform used as an input to the amplifier for droplet ejection (a) Voltage, (b) velocity,  $v(r)$ .

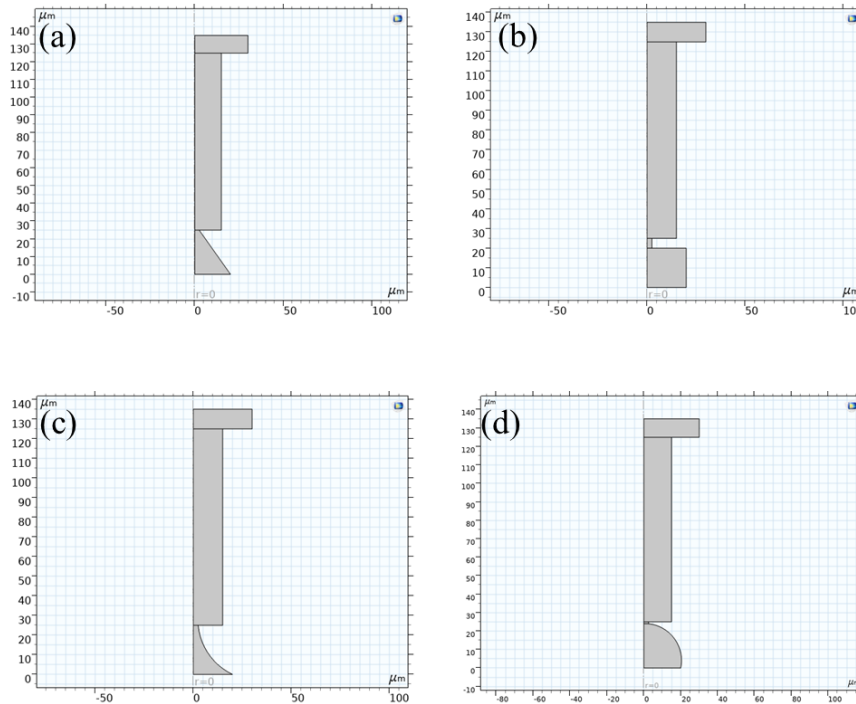


Figure 2.13 – Schematic of different nozzle shapes (a) Taper, (b) Straight, (c) Cymbal, and (d) Hourglass.

### 2.3.2.2 Nozzle Shape Simulations

As discussed already, simulations are performed for multiple parameters. Only one parameter is varied every simulation run to allow the understanding of parameter impact on droplet ejection and droplet diameter. The default value of nozzle height is  $25\mu\text{m}$ . Different shape of nozzles such as taper, straight, hourglass, and opposite hourglass shape with  $5\mu\text{m}$  orifice diameter shown in figure 2.13 and water as medium is simulated to determine the droplet diameter for the range of inlet velocities. Figure 2.14 represents that the taper, straight, cymbal and hourglass type of nozzle produces the droplet at  $v(r) > 0.2\text{m/sec}$  and the taper shape nozzle produce the droplet diameter minimum of all other geometries. All the nozzle geometries

produced the droplet diameter of almost same size and slightly higher than the diameter of the nozzle exit.

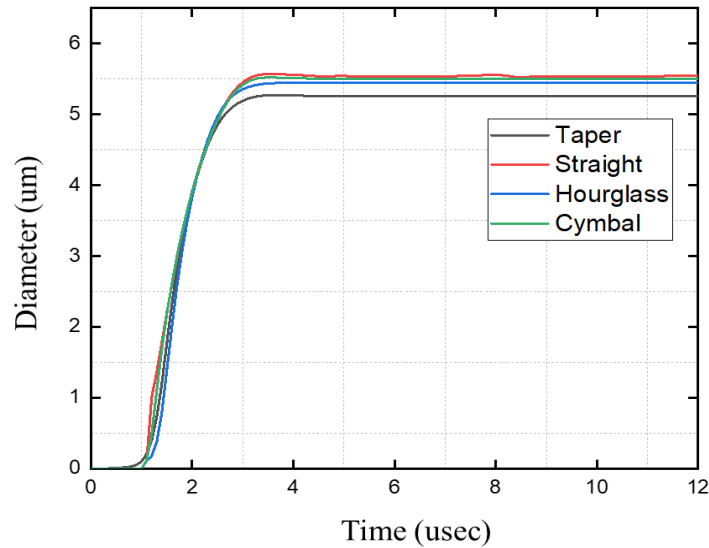


Figure 2.14 – Droplet size for various nozzle shape.

Taper shape produces most uniform droplet diameter for wide range of velocity. The value is similar to the actual devices that are found to be functional.

When simulations are carried out, the average peak velocity values in COMSOL are varied assuming small values at the beginning. This assumed average peak velocity is gradually increased to represent a shift from not being able to eject the droplet using the model to being able to eject the droplet. The minimum average peak velocity required to eject the droplet is 0.2m/sec at inlet which corresponds to the peak displacement of 2 $\mu$ m. A set of images showing two images are shown in figure 2.15. In one of these models 2.15(a), small inlet velocity ( $\sim$  0.05m/sec) is used which is not sufficient to produce the droplet while a droplet is ejected successfully from the other model as a result of larger inlet velocity, both the simulations are performed for one cycle of waveform i.e., one positive and one negative for 5 $\mu$ sec each.

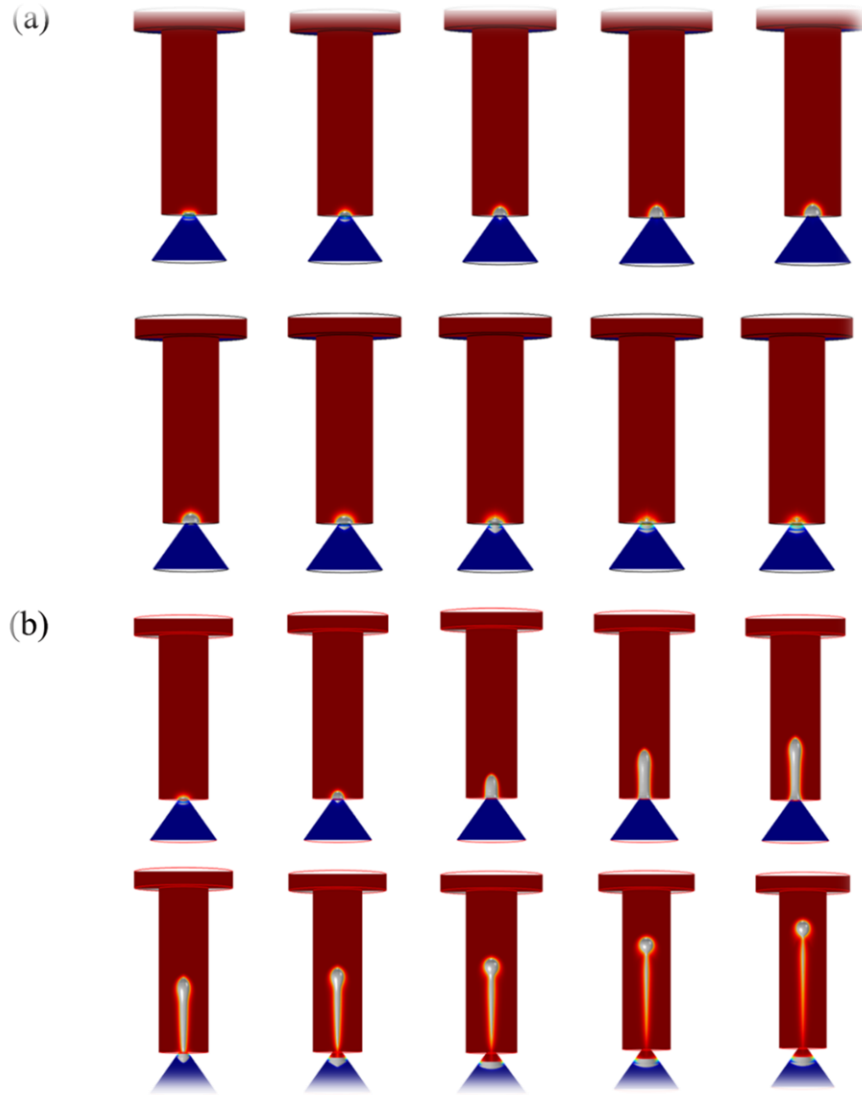


Figure 2.15 – (a) a set of images showing a model that did not eject any droplet due to use of small inlet velocity, (b) a set of images showing a model that eject a droplet successfully when large inlet velocity is used.

When the peak inlet velocity is further increased, the volume and velocity of the ejected droplet increases linearly and thus the resultant droplet diameter also increases. The large inlet velocity corresponds to the larger deformation of the atomizer membrane and large applied energy. With increase in applied energy, it is easy to break the surface tension bond of the liquid droplet and produce spray with decrease in droplet breaking time. The increase in the velocity of

ejected droplet is due to gain in kinetic energy of the droplet as input energy is increased. Figure 2.16 shows the change in velocity of the droplet, volume, and breaking time of the droplet at further increase in inlet velocity of the device. At the lowest input velocity i.e., 0.1m/sec the droplet formation did not occur whereas for velocity at and above 0.2m/sec the droplet formation starts and further increase in velocity results into higher velocity of ejected droplet with increased diameter.

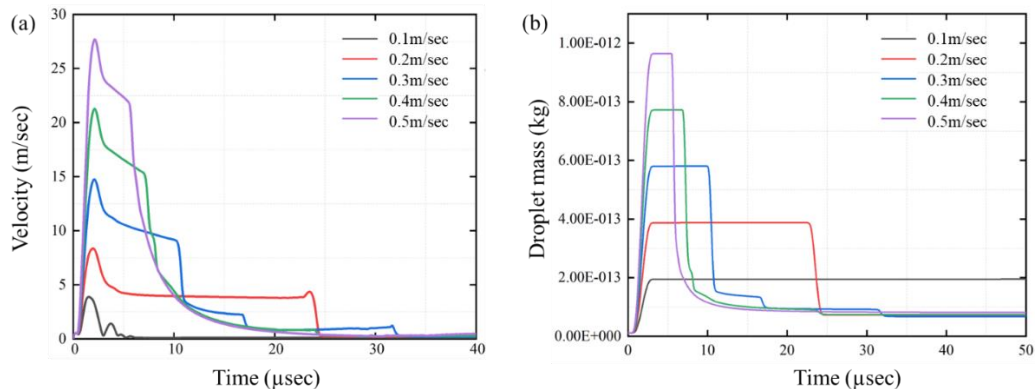


Figure 2.16 – Ejected droplet velocity and mass at variable input velocity.

### 2.3.2.3 Effect of Orifice Diameter on ejected droplet diameter

The outlet diameter of the nozzle is a crucial element, as a too-small hole will not allow enough liquid to pass through, while a too-large aperture will allow the liquid to seep through. Consequently, evaluating the relationship between the nozzle aperture, droplet size, and energy required to contribute to the droplet formation process is vital. Figure 2.17 shows the orifice diameter as the function of inlet velocity and droplet diameter. Drop diameter shows almost the linear relationship with the orifice diameter. And as the diameter increases the inlet velocity or energy required for droplet formation also increases. For the nozzle with 10µm outer diameter, the drop formation occurs at the maximum inlet velocity.

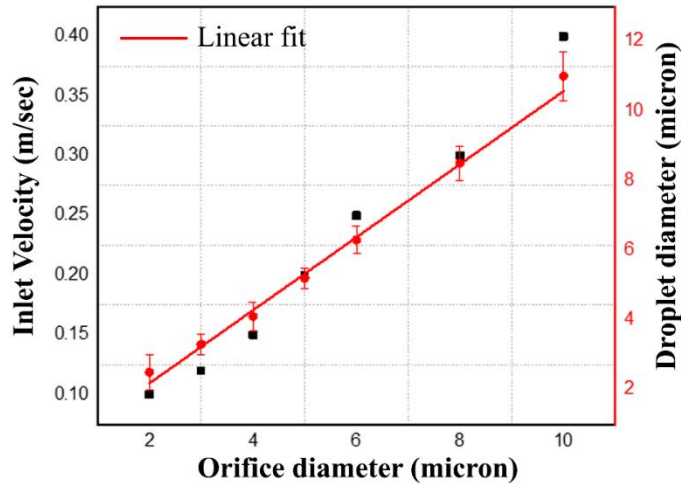


Figure 2.17 – Droplet diameter as a function of orifice diameter at different inlet velocity,  $v(r)$  for taper shape nozzle.

During droplet formation, five different mechanisms occur at the nozzle outlet as the function of jet outflow velocity due to interaction of gravity, surface tension, viscous force, and the input energy. Figure 2.18 shows the different mechanisms of the droplet formations presented by Reynolds and Ohnesorge numbers, where, at low outflow velocity, single droplets are directly formed at the exit of the nozzle (mechanism 0 and I), further increasing the input energy or kinetic forces develop the uninterrupted outflow of the jet which breaks up afterwards by symmetric vibrations and surface tension (mechanism II), and upon more increase in jet velocity leads to the statistical distribution of the droplet size (mechanism III) and jet is sprayed when high friction forces are present. For this research work, the exit velocity for the modelled device, is measured to be 14.9m/sec (grey line) and the corresponding dimensionless numbers were calculated and plotted for different property fluids (viscosity and density whereas surface tension was kept constant) and it can be seen that for liquids with low kinematic viscosity, droplet formation process falls under mechanism II and as the liquids gets dense the Reynolds number reduces and Ohnesorge number increases and formation moves

under mechanism 0 and I. In our study, the sinusoidal force at applied frequency supports the laminar jet breakup in the droplet's formation mechanism II for low viscous fluids. For the constant kinematic viscosity and variable surface tension,  $Re$  being constant, the  $Oh$  varied ( $Oh$  increased as the surface tension value decreases for the liquid). The difference in the  $Oh$  due to change in  $\sigma$  was not substantial and the same trend would be followed for the liquids with different  $\nu$ .

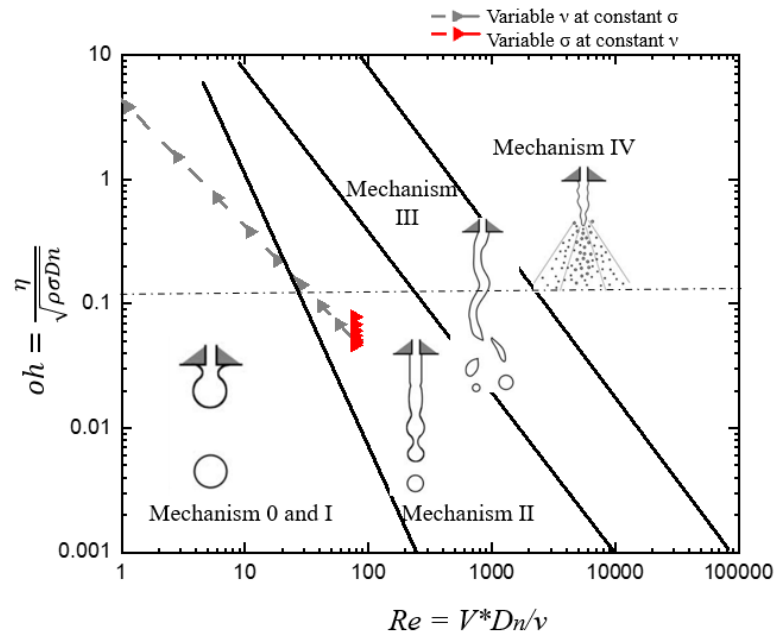


Figure 2.18 – Ohnesorge number versus Reynolds number graph for optimal working conditions [56].

## 2.4 Summary

Numerical simulations targeting dimension and gaining an understanding of the behavior of the membrane geometry on the device performance are presented in this chapter. Structural Mechanics, electrostatics, and two-phase flow in COMSOL are used for these simulations. The Resonance frequency, displacement, velocity, and mode shapes of the various dynamic modes of the atomizer were studied using finite element analysis and will be compared with the

experimental results to validate the model. Structural mechanics demonstrated the frequency responses and effect of physical parameters on frequency, vibration modes, and displacement of the membrane. The frequency related to the mode of operation depends on the design parameters of the device. The resonance frequency is higher for small membrane diameters with a smaller number of apertures. The frequency decreases when the membrane diameter increases as the overall stiffness of the membrane decreases. The thickness and membrane material can be changed to modify the frequencies. The device vibrates at a frequency, deforms repeatedly, and performs atomization by overcoming the liquid's surface tension and viscous forces. The membrane velocity provides the energy required to overcome these forces, and it is determined that speed depends on the resonance frequency and its displacement. The out-of-plane displacement varies linearly with the input supply voltage. Apertures have minimal impact on the 02-frequency mode, and devices with different hole sizes operate at almost the same frequency. Apertures have minimal impact on the frequency mode, and devices with different hole sizes operate at the same frequency.

The results of the two-phase flow simulations suggest that taper shape nozzle results in the lowest droplet diameter compared to other nozzle shapes such as straight, cymbal, and hourglass nozzle for the same exit nozzle diameter. Hence, a taper shape nozzle is chosen for further simulations. In terms of orifice diameter, the results suggest that low orifice diameter ejects the droplet at low velocity, and high orifice diameter requires more energy to form the droplet. At the maximum inlet, the rate applied orifice diameter below  $10\mu\text{m}$  is ideal for ejecting the droplets. Fluids with different dynamic viscosity are studied for a fixed orifice diameter, suggesting that liquid with a viscosity up to 5cPs can form and eject the droplet from the nozzle. Above this viscosity, the droplet bulges out of the nozzle but does not have enough

energy to separate and form droplets. This result confirms that the velocity of the membrane, i.e., the maximum inlet velocity of the fluid, is sufficient for fluid with low kinematic viscosity and that the device requires more energy to eject highly viscous liquids. To accomplish spray formation with very viscous fluids, high input energy to the membrane that increases the inlet velocity or decreases the fluid's viscosity with the same input velocity are viable options. Since this device has a constraint on the supply of input voltage and limiting input energy, the collection of heat energy to reduce the viscous forces in the liquid by implementing a microheater is achievable and is a proposed concept for further work.

# **CHAPTER 3**

## **FABRICATION AND CHARACTERIZATION OF VIBRATING MESH ATOMIZER**

This chapter focuses on microfabrication of vibrating mesh atomizer using semiconductor processes and characterization of the device based on its working and output. This fabricating the MEMS based atomizer, integrating the assembly and characterization of the device involves determination of operating frequency, input voltage required, deformation of the membrane, and size distribution of the droplets produced with different liquids. Later in the chapter, the microfabricated device is compared with the commercial metallic vibrating mesh atomizer and ultrasonic atomizer in terms of droplet distribution and then two types of VMA are compared based on geometry of the devices, distribution of the produced droplets for different property liquids, volumetric median diameter (VMD), temperature distribution over the surface.

The MEMS vibrating mesh atomizer developed in this study use a circular vibrating membrane with multiple apertures to produce droplets actuated through piezoceramic ring driven by the voltage supply provided. Silicon has been chosen for fabricating the micronozzles as it widely used in MEMS microfabrication, is resistant to chemicals, and low-cost. Also, it is compatible to various etching methods, both wet and dry. Silicon has young's modulus in the range of 140-180 GPa, comparable to steel (190-210GPa). Silicon on insulator wafer is chosen for the device fabrication to take an advantage of buried oxide as etch stop layer. The apertures can be fabricated out of Metal, silicon, glass, or polymers.

The process of fabrication starts with designing a photomask for photolithography process. Two masks were designed and used for fabrication of the device, one for the apertures on the front side of the wafer and second for the backside of the wafer. K-layout software is used to create the mask layout.

### **3.1 Photomask layout**

The photomask is the template of atomizer design transferred on to the quartz or glass substrate for optical photolithography system. The design on the quartz plate can be dark field where structures to be transferred is open and rest of the part is covered or dark or bright field in which the structures are dark, and the rest of the portion is opaque. The type is chosen depending on the type of photoresist will be used during lithography process step. The layout is prepared in the GDS file format with the K-Layout program for this device. Multiple layers, photos, rulers, switchable layer views, cell blanking, and browsable shape or instance make it simple to see complicated patterns. This program makes it simple to create masks by allowing users to create cells and layers with various forms such as polygons, boxes, wires, and more, as well as edit instructions such as move, rotate, and mirror chosen items. For the atomizer device, mask designing includes two-layer mask, one photomask for creating the base pattern for the nozzle array and second mask for defining the holder pattern on the opposite side of the wafer. The resultant mask was 5\*5 inch in which the pattern covers 4\*4 -inch area. Figure 3.1 shows the layout of each mask. Light part in the mask are open areas. The masks are designed to fit 75-80 devices per 4" wafer. Mask features at the center left and right are used for alignment purpose. Backside alignment method is used to align the surface of the wafer. Alignment marks in front side are the four squares to fit into the four cross lines in the backside mask.

The circular street is created at both sides of the mask. The front side has four tether to connect the membrane with the wafer and the rest of the circular part is to be etched in KOH etching. The backside of the wafer has circular street around the actual device that is to bulk etched during DRIE and later on while removing the device, the tethers can be pricked and be detached from the rest of the wafer to get the access of easy removal avoiding the dicing step. The devices are thin membrane and delicate enough to break by the blade and water pressure in the dicer and hence, tethers and circular street on both masks were designed so the devices can be easily removed by breaking the joints by pricking needle without dicer.

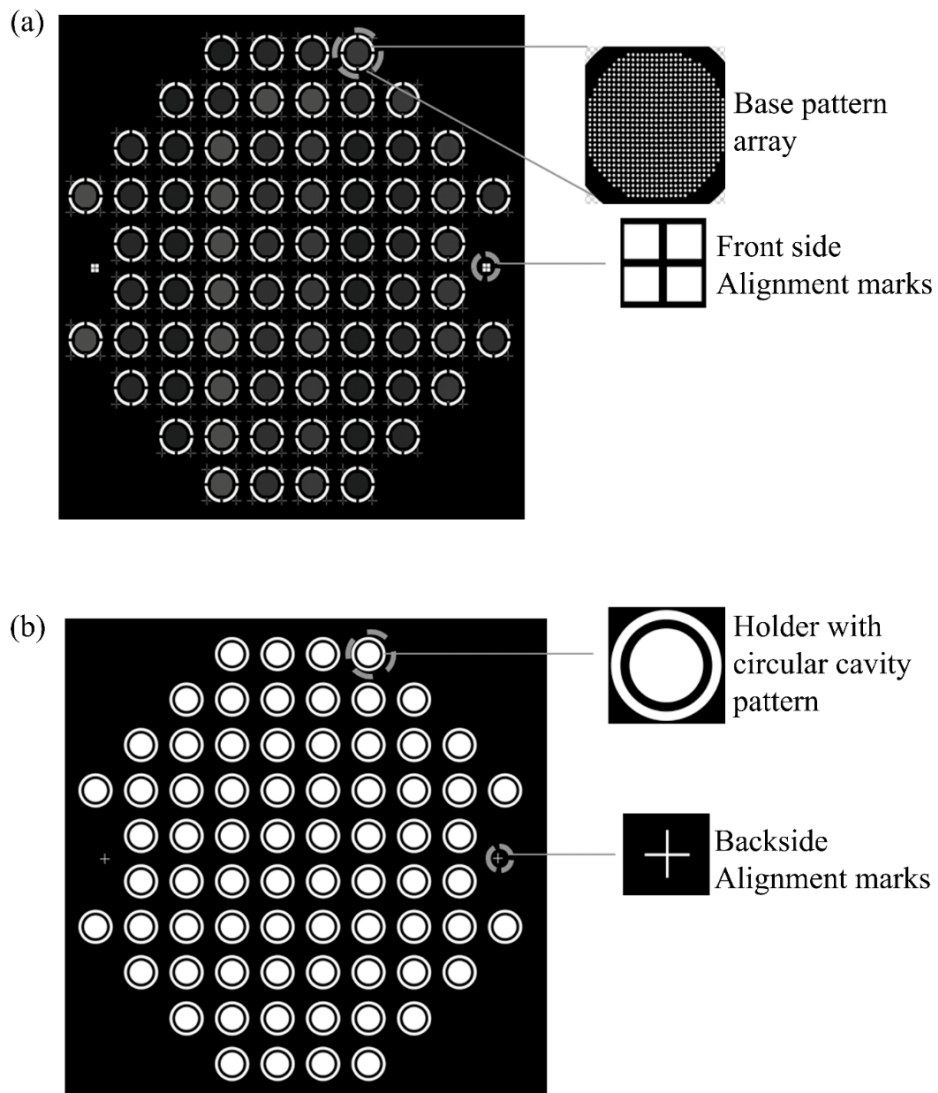


Figure 3.1 – Front and backside photomasks: (a) front side used to define the structure of nozzle arrays, (b) backside used to define the holder and cavity size with alignment marks.

### **3.2. Vibrating Mesh Atomizer Microfabrication**

The fabrication process comprises of number of photolithography, deposition and etching methods that are widely used in semiconductor industry. The silicon membrane of the MEMS atomizer was designed to be 30  $\mu\text{m}$  thick with a 5 mm diameter and apertures with 120  $\mu\text{m}$  pitch with an outlet dimension of 10, 20 and 30  $\mu\text{m}$ . The device was fabricated from Silicon-on-Insulator wafer with device thickness of 30  $\mu\text{m}$ , 1  $\mu\text{m}$  buried oxide and 300  $\mu\text{m}$  handle silicon. Buried oxide acts as an etch stop for the etching steps.

Before starting the fabrication process, the thickness of the silicon device is measured using Dektak profilometer (corners of the wafer has exposed silicon dioxide) to confirm the device thickness. The process flow is shown in figure 3.2. The SOI wafer was cleaned for 5 minutes in piranha solution which is 4:1 mixture of Sulfuric acid ( $\text{H}_2\text{SO}_4$ ) and hydrogen peroxide ( $\text{H}_2\text{O}_2$ ) at 100°C and then immersed in 6:1 BOE etchant to remove native oxide and spin rinse dried in DI water and then dehydrated on a hot plate at 100°C for 10 minutes. The fabrication process started with wet thermal oxidation growth of 1  $\mu\text{m}$  silicon dioxide mask layer on both sides of the wafer. Then, wafer is coated with vapor Hexamethyldisilane (HMDS) at 100°C for 20 seconds. The resist AZ10XT is spin coated at 3000 rpm for 45 seconds at an acceleration of 5000 rpm/sec to create 6-8  $\mu\text{m}$  thick layer and soft baked at 120°C for 2 minutes. The film is then exposed to UV light for 150 seconds at an intensity of 2.5W/m<sup>2</sup> and gap of 30  $\mu\text{m}$  between the mask and resist film. The exposed film is developed in AZ 400K 1:4 for 5 minutes as shown in figure 3.3(a). Patterned silicon dioxide mask layer with number of hole or apertures is etched using Reactive ion etcher (RIE). The anisotropic straight plasma etching of  $\text{SiO}_2$  layer

uses two gases for etching, 84% CF<sub>4</sub> flow of 50 standard cubic centimeters per minute (sccm) and 8% O<sub>2</sub> flow of 250 sccm. SiO<sub>2</sub> etching is carried out at 300 mTorr pressure, 250W power for 10 minutes at the etch rate of 1100 Å/min and after etching optical image is shown in figure 3.3(b). The apertures i.e., silicon is etched using KOH at 60°C for 1 hour and 15 minutes down to BOX layer with silicon etch rate of 22.3µm/hour and 81.61nm/hour for SiO<sub>2</sub> protecting the backside of the wafer using wet etch holder that exposes front side to the etchant and cover the other side. The etch profile of KOH is taken advantage of to create the taper nozzle shape. KOH being an anisotropic etching process, sidewalls of etch defined by <111> plane and the <100> plane is etched at a 54.7° angle related to <111> plane shown in figure 3.4 and formation of taper nozzle from circular cavity defined on the mask in figure 3.3(c). The etching of the nozzle is carried out until the buried oxide layer is reached so, the thickness of the device is important to achieve desired outlet size of the nozzle and is calculated as  $A = d + 2 \cdot h \cdot \cot 54.7^\circ$ , where A is feature size on mask, d is desired nozzle size on the processed wafer, h is the wafer or device thickness. The apertures patterned are circular structures and after KOH etch, resultant will be pyramid shaped cavity. This shape is regardless of the initial shape of the apertures chosen, a square, circle, diamond, or octagon all of them will result in a pyramid shaped cavity. Circular shape is chosen for this device due to its ease in mask designing.

Before, processing the other side of the wafer, the front side is covered and protected with resist coat (AZ1518 spun at 2500rpm for 45 seconds and soft baked at 110C for 1 minutes). The handle or backside of the wafer is spin coated with AZ10XT at 1000rpm for 45 seconds resulting in 10µm thick resist film and soft baked at 120°C for 120 seconds. The film is then exposed to UV light for 300 seconds and developed for 2 minutes in AZ 400K 1:4. The SiO<sub>2</sub> is etched in Buffered oxide etch (1:6) for 15-17minutes at an etch rate of 800Å/minute to open

the structures followed by QRD (quick rinse dried). Then the wafer is prepared for bulk silicon etch and 4" wafer is loaded on to the wafer holder facing the backside up and the holder sits on the chuck of DRIE. The gap between the wafer frontside and top surface of the holder is sealed with the fomblin oil. Fomblin oil helps to dissipate heat while etching and acts as a lubricant and coolant during the process. The handle silicon is etched using Deep reactive ion etching (DRIE) with SiO<sub>2</sub> and resist as mask layer. The gases used are SF<sub>6</sub> with 300 sccm and C<sub>4</sub>F<sub>8</sub> with 100 sccm flow rate at 50W power. Alternates etch and passivation steps of 5 second and 1 second is used during the process. After etching is completed, the wafer is removed from the tool and fomblin oil is cleaned using Isopropyl Alcohol and then the wafer is soaked in acetone to remove resist. Then the buried oxide and remaining mask layer is removed using BOE wet etch for 15 minutes. For further cleaning the devices and wafer, piranha is used after oxide etch at 100C for 10 minutes.

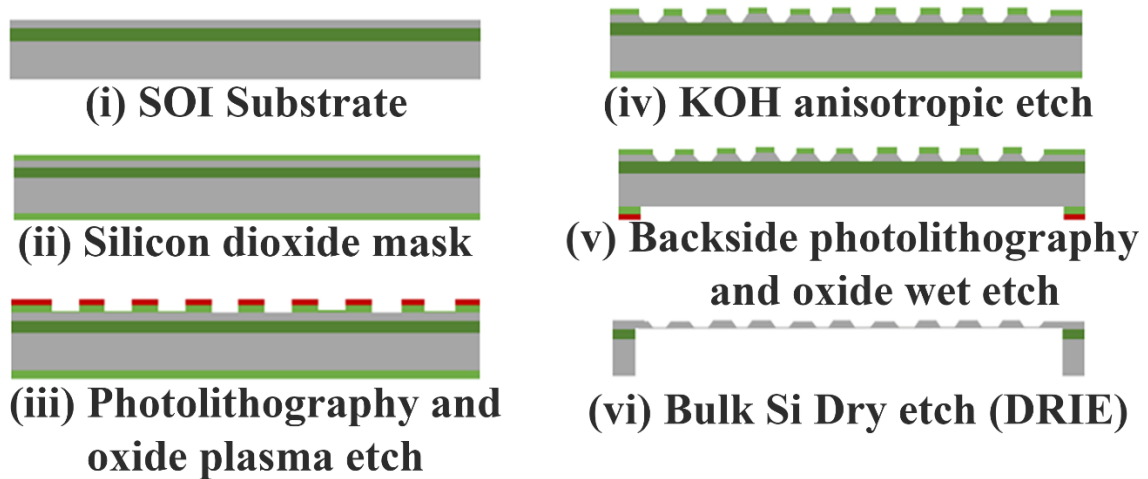


Figure 3.2 – Schematic view of fabrication process of vibrating mesh atomizer device.

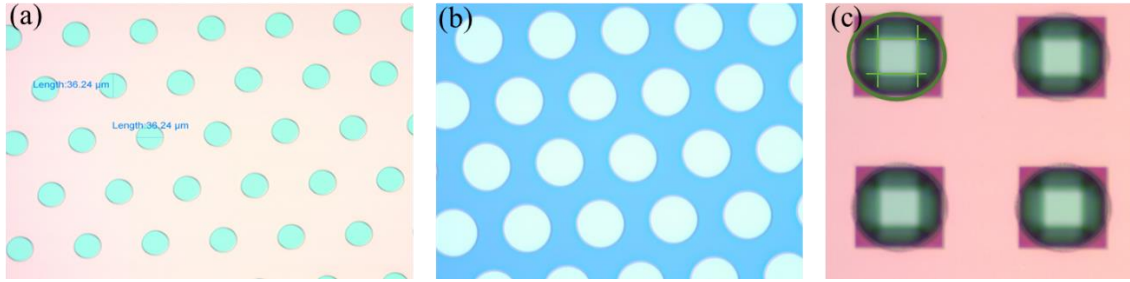


Figure 3.3 – (a) Aperture pattern after developing, (b) aperture after oxide mask etch (c) apertures after KOH etch to form nozzles.

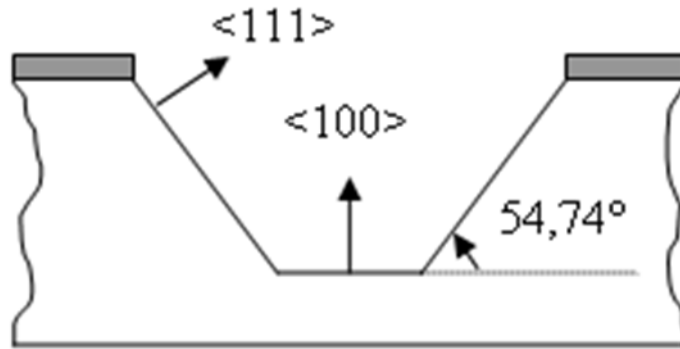


Figure 3.4 – Silicon crystal plane etch using KOH.

### 3.3 DRIE Characterization

For fabrication of the backside of the device, bulk silicon etching using Deep reactive Ion Etching (DRIE) that uses Bosch process is used which employs etching gas and passivation gas in alternate etch and passivation cycles. The etching gas i.e.,  $\text{SF}_6$  assures the etching of the silicon substrate and passivation gas i.e.,  $\text{C}_4\text{F}_8$  contributes towards polymer formation (poly-tetra-fluoro-ethylene) which act as a protective layer while etching silicon. The sidewall profile angle and grass development at the bottom surface of the silicon were the major concerns, therefore the influence of both gas flow rates is investigated, and the optimum parameters for operating the tool with no problems are identified. The challenges found when running the tool at the optimum recipe settings are explored, as well as the actions taken to resolve them.

Alcatel DRIE system housed at University of New Mexico Manufacturing Training and Technology Center (MTTC) is used to perform all the experiments. 100mm (4-inch) diameter, p-type, <100> orientation, and 525 $\mu$ m thick silicon wafers were used to perform all the experiments. Thermal oxide of 1 $\mu$ m thickness was grown on the silicon wafers as mask layer. Photolithography was performed to transfer the pattern on the wafer using AZ1518 photoresist. The wafer was coated with HMDS (Hexamethyldisilane) to make the surface hydrophobic and then resist was spin coated at 2500rpm followed by soft bake at 110°C for 1 minute and exposed to UV rays with the dose of 90mW/cm<sup>2</sup> and developed for 2 minutes. Metrology mask with different structures varying from 5 $\mu$ m to 20 $\mu$ m and various logos was used for patterning the wafer using Karl Suss MA06 aligner. The experiments were performed with DRIE system by varying the SF<sub>6</sub> and C<sub>4</sub>F<sub>8</sub> flow rate, etching and passivation cycle time as mentioned in table 3.1.

The SF<sub>6</sub> flow rate was varied from 200sccm to 350sccm in the step of 50sccm at constant C<sub>4</sub>F<sub>8</sub> flow rate of 100sccm. The C<sub>4</sub>F<sub>8</sub> flow rate was varied from 50sccm to 200sccm in the step of 50sccm at constant etch gas flow rate of 300sccm. The etching and passivation cycle time ratio were changed to see the effect on etching characteristics. All the samples were etched for 30minutes. After etching, the samples were diced using *UNO 7900 wafer dicer* and analyzed sectional profile and surface smoothness using scanning electron microscope (Phenom ProX). The SiO<sub>2</sub> thickness is measured using Nanometrics CTS 102 tool.

Table 3.1. DRIE parameters used in experiments.

Exp. No.	Etch: Pass time (sec)	C <sub>4</sub> F <sub>8</sub> Flow rate (sccm)	SF <sub>6</sub> Flow rate (sccm)
1	5:1	50	300
2	5:1	100	300
3	5:1	150	300
4	5:1	200	300
5	7:2	50	300
6	7:2	100	300
7	7:2	150	300
8	7:2	200	300
9	5:1	100	200
10	5:1	100	250
11	5:1	100	350
12	7:2	100	200
13	7:2	100	250
14	7:2	100	350

The characterization of DRIE etched silicon samples with SEM obtained images were performed. Table 3.2 and 3.3 demonstrates the etch rate of silicon of 20 $\mu$ m and 100 $\mu$ m structures, etch rate of SiO<sub>2</sub> mask layer and profile angle. The etch rates are calculated by the ratio of depth etched to the time of total etch and the profile angle is the slope of sidewalls with

respect to the bottom surface of the silicon. The positive profile angle is referred to the angle more than 90° and negative corresponds to the angle less than 90°.

Table 3.2. Etch rate and profile angle of trenches etched at different C<sub>4</sub>F<sub>8</sub> flow rate.

Exp No.	C <sub>4</sub> F <sub>8</sub> flow rate (sccm)	Etch: Pass time (sec)	Etch rate 20μm structure (μm/min)	Etch rate 100μm structure (μm /min)	SiO <sub>2</sub> etch rate (Å/min)	Profile angle (θ)
1.	50	5:1	1.77	2.76	138.3	104.5
2	100	5:1	1.69	2.42	100.4	90.1
3	150	5:1	1.64	2.31	89.26	91.6
4	200	5:1	1.26	1.79	75.7	92.7
5	50	7:2	1.79	2.65	98.8	90.74
6	100	7:2	1.70	2.33	117.4	91.1
7	150	7:2	0.87	1.42	227.8	92.9
8	200	7:2	0.85	1.24	250	96.5

Table 3.3. Etch rate and profile angle of trenches etched at different SF<sub>6</sub> flow rate.

Exp No.	SF <sub>6</sub> flow rate (sccm)	Etch: Pass time (sec)	Etch rate 20μm structure (μm/min)	Etch rate 100μm structure (μm /min)	SiO <sub>2</sub> etch rate (Å/min)	Profile angle (θ)
1	200	5:1	1.31	1.76	88.43	93.1
2	250	5:1	1.4	2.11	103.7	92.5
3	300	5:1	1.69	2.42	100.4	90.1
4	350	5:1	1.95	2.65	120	89.6
5	200	7:2	0.95	1.31	90	94.1
6	250	7:2	1.04	1.39	111.6	92.4
7	300	7:2	1.70	2.33	117.4	91.1
8	350	7:2	2.59	3.4	127	89.8

### 3.3.1 Effect of C<sub>4</sub>F<sub>8</sub> and SF<sub>6</sub> on Side wall profile

Effect of C<sub>4</sub>F<sub>8</sub> flow rate on etched profile of the structures is shown in figure 3.5. Figure 3.5(a) shows the profile of the structures at varying flow rate at the etch and passivation cycle ratio of 5:1 and constant SF<sub>6</sub> flow rate of 300sccm. It is observed that at low flow rate of 50sccm, the profile angle is positive with an angle of 104.5° and as flow rate increases and at 100sccm, the profile angle is changed from positive to vertical profile i.e., 90° and when further increased, the side angle changes to positive profile with broad top opening and narrow bottom side of the etched structure. The low flow rate of C<sub>4</sub>F<sub>8</sub> means the quality of passivation layer is low and is not sufficient to prevent the sidewalls from etching during the etching cycle and therefore, the type of etching was highly isotropic at 50sccm flow rate. When, the flow rate increased, the passivation layer was quality was enhanced to protect the walls while etching that lead to the profile angle changing to almost straight sidewalls with angle of 90° at maximum flow rate of 100sccm. At flow rate of 150 and 200sccm, the polymer coating was more than required to protect the sidewalls and therefore, the fluoride ions etching the surface was unable to etch the entire thick layer of polymer leaving the positive profile of the etched structure. When the C<sub>4</sub>F<sub>8</sub> flow rate is varied at 7:2 cycle time, the vertical straight sidewalls were observed at 50sccm and any gas flow higher than 50sccm resulted into maximum positive profile angle of 96.5° at 200sccm as seen in figure 3.5(b).

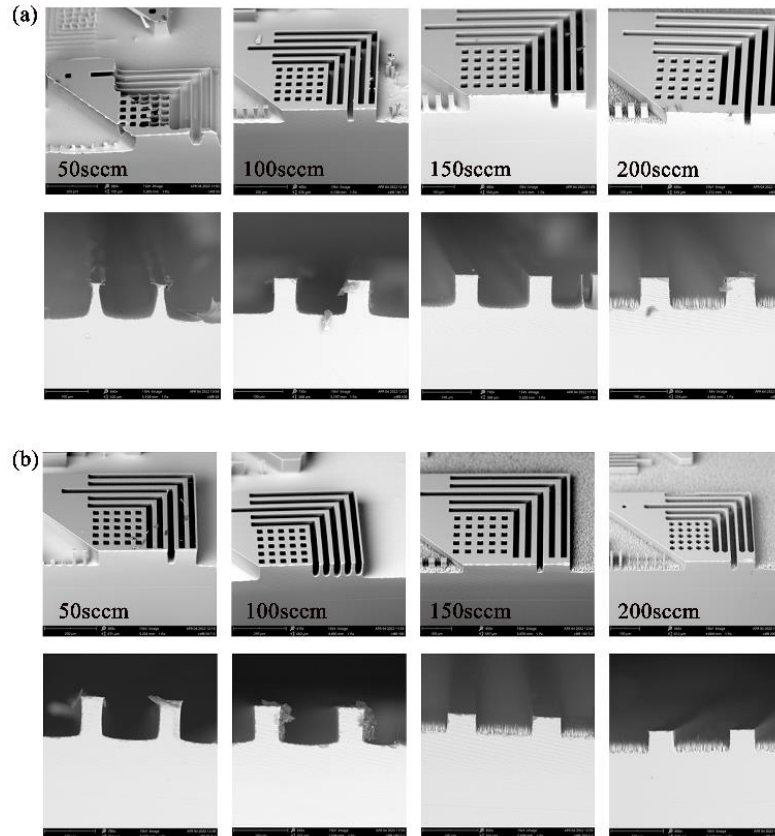


Figure 3.5 Shape profile of trenches etched with variable  $C_4F_8$  flow rate with etch and passivation cycle ratio of (a)5:1, (b)7:2.

Figure 3.6(a) demonstrates the effect of varying  $SF_6$  flow rate on etched profile of the structures at the cycle ratio of 5:1 and constant  $C_4F_8$  flow rate of 100sccm. It is observed that the sidewall angle is positive (broad top opening and narrow bottom opening) at low  $SF_6$  flow rate of 200sccm at angle of  $93.1^\circ$  and approaches to the vertical straight profile of  $90.1^\circ$  at increased  $SF_6$  flow rate of 300sccm and it changes to negative profile angle of  $89.6^\circ$  when flow rate is further increased to 350sccm. The profile angle follows the same pattern at a 7:2 cycle ratio, with a positive profile ( $94.1^\circ$ ) at 200sccm and negative profile ( $89.8^\circ$ ) at 350sccm flow rate. The low etching capability of fluoride ions reaching the bottom surface to remove the passivation layer and reach silicon sidewalls is the reason for the positive profile at low  $SF_6$

flow rates. The negative profile at a maximum flow rate of 350sccm is owing to decreasing passivation layer quality as etch depth increases, as well as increasing fluoride ion effect on sidewalls. Because fluoride ions are isotropic (they etch in all directions at the same rate), if the SF<sub>6</sub> flow rate is increased further, lateral etching will begin alongside vertical etching.

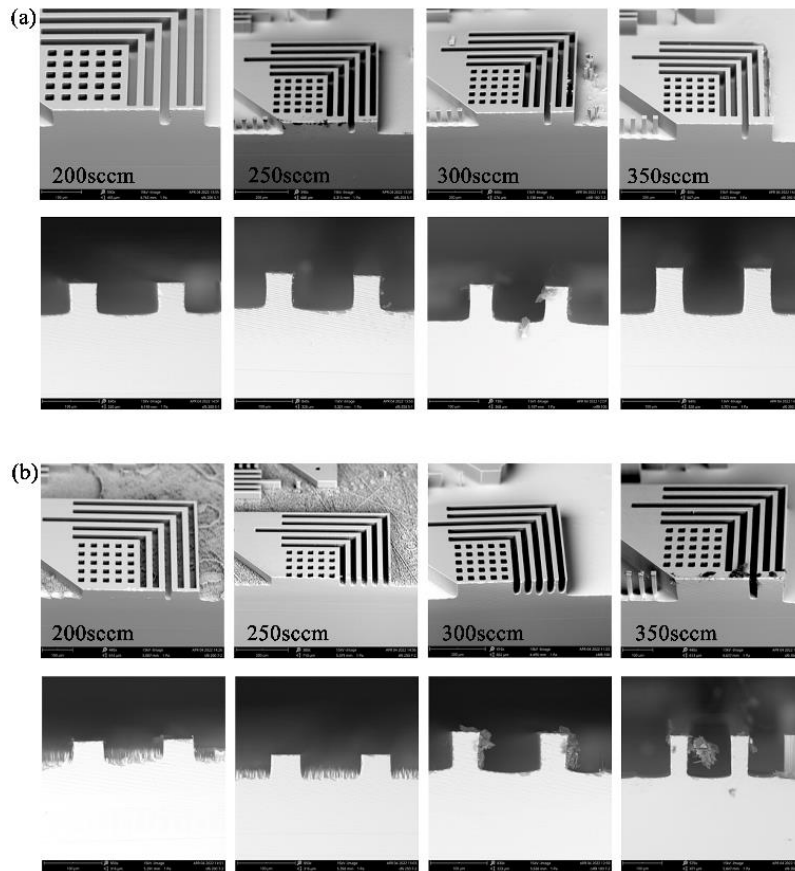


Figure 3.6 Shape profile of trenches etched with variable SF<sub>6</sub> flow rate with etch and passivation cycle ratio of (a)5:1, (b)7:2.

### 3.3.2 Effect of C<sub>4</sub>F<sub>8</sub> and SF<sub>6</sub> on Grass formation

One of the major defects during anisotropic etching of silicon in DRIE is grass production, which is needle-like silicon structures also known as black silicon. The influence of gas flow rates on grass formation is also investigated in this work with the goal of determining the ideal parameters to avoid or entirely eliminate grass formation. Both the gases contribute towards

this defect and is demonstrated in figure 3.7. At a 5:1 cycle and 300 sccm SF<sub>6</sub> flow rate, no grass was observed at C<sub>4</sub>F<sub>8</sub> gas flow rates of 50 and 100 sccm, but when the flow rate was increased to 150 sccm, grass appeared with a grass length of 5-6µm, and at 200 sccm, grass density increased and was visible throughout the sample. There was no grass at 50sccm for the 7:2 cycle ratio, but it began to develop as the flow rate increased. The reason for this is that when the C<sub>4</sub>F<sub>8</sub> flow rate increases, more polymerizations occur, causing the etching cycle to be insufficient to etch through the polymer layer resulting in the production of grass.

No grass production was observed when the SF<sub>6</sub> flow rate was varied at a constant 100 sccm C<sub>4</sub>F<sub>8</sub> rate and a 5:1 cycle ratio. Due to localized concentrations of fluoride ions, slight grass was seen at the bottom and edges of the structures at high flow rates (350sccm). This means that when the etch stage is preliminary, the incoming fluoride ions distribution is high, preventing grass formation, but as the etch depth increases, the ion angular dispersion flux sharpens, causing grass to form at the bottom surface or at the corners of the structures. Grass formation was noticed at 200, 250, and 300 sccm flow rates with a cycle ratio of 7:2. Density of the grass was high at low flow rates, but no grass was observed at 350 sccm flow rate. The explanation for this might be that at low flow rates, the fluoride ions are insufficient to remove the polymer layer, resulting in grass, whereas at higher flow rates, the number of fluoride ions available to etch the surface increases, resulting in no grass.

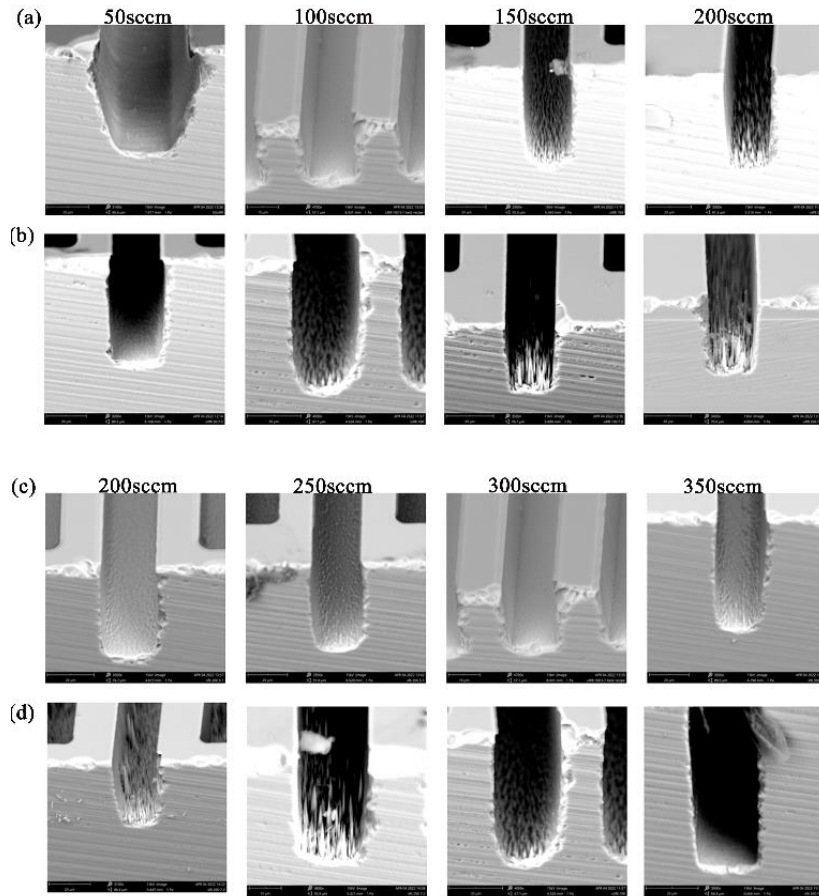


Figure 3.7 (a), (b) Effect of  $C_4F_8$  on grass formation with etch and passivation cycle ratio 5:1 and 7:2, (c), (d) effect of  $SF_6$  on grass formation with etch and passivation cycle ratio of 5:1 and 7:2.

Apart from the gas flow rates that affect grass development, the etching and passivation cycle duration also has an impact. For all of the gas flow rates examined, a 5:1 ratio was determined to be superior to a 7:2 ratio. The grass is often generated as a result of the micro masking effect, which occurs when the etching time is insufficient to completely remove the bottom polymer layer, and the leftover polymer acts as a mask, preventing the underlying silicon from etching. This produces silicon structures that look like needles or grass. In comparison to the cycle of 7 seconds etching and 2 second passivation, less bottom grass was detected for various gas flow rates when the etching cycle period was 5 seconds and 1 second of passivation.

### **3.3.3 Effect of C<sub>4</sub>F<sub>8</sub> and SF<sub>6</sub> on etch rates**

The etch rates of silicon and mask layer as mentioned in table 3.2 and 3.3. It is strongly dependent on the C<sub>4</sub>F<sub>8</sub> flow rate, SF<sub>6</sub> flow rate and etch and passivation cycle time. As the C<sub>4</sub>F<sub>8</sub> flow rate or the time of passivation increases the etch rate of silicon and silicon dioxide slows down as the availability of polymer is more to be etched to reach the underneath surface and when the SF<sub>6</sub> flow rate or etch cycle time increases, the etch rate increases due to availability of fluoride ions to etch. The maximum etch rate of silicon for this study is 3.4μm/min at 350sccm SF<sub>6</sub> and 100sccm C<sub>4</sub>F<sub>8</sub> at 7:2 cycle. The etch rate is also affected by the structure's opening size, broad openings have a greater etch rate than narrow opening, that the etch rate of a 100μm opening is higher than a 20μm opening due to a decrease in fluoride ion availability due to sidewall scattering when etching the high aspect ratio structure.

### **3.3.4 Effect of cooling on the etch profiles**

The Alcatel system wafer loading chuck is designed for 6-inch wafers, and 4-inch wafers are processed using an aluminum plate with a 100mm diameter groove to accommodate the wafer as shown in figure 3.8. The plate is loaded on top of the clamp and transferred onto the chuck where the etching process takes place and the temperature inside the chamber reaches 150°C and ideally the chuck temperature is maintained at 20°C but since the 4-inch wafer is not directly loaded onto the chuck, a good thermal contact between the cathode and wafer is important because if the wafer gets too hot (50°C and above) and heat does not get dissipated due to poor thermal contact, the polymer layer deposited gets desorbed and hot wafer etches isotropically in all the directions instead of anisotropic. To address this issue, fomblin oil is utilized as a coolant to assist disperse heat and ensure that the wafer does not become too hot

to etch properly. Figure 3.9 compares a heated wafer etched isotropically to one etched anisotropically with fomblin oil between a wafer and an aluminum plate.

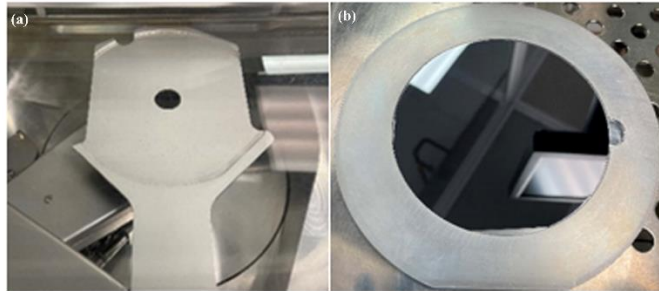


Figure 3.8 (a) DRIE loading chuck for 6-inch wafer, (b) A 150mm diameter Aluminum plate with 100mm diameter groove for holding 4-inch wafer.

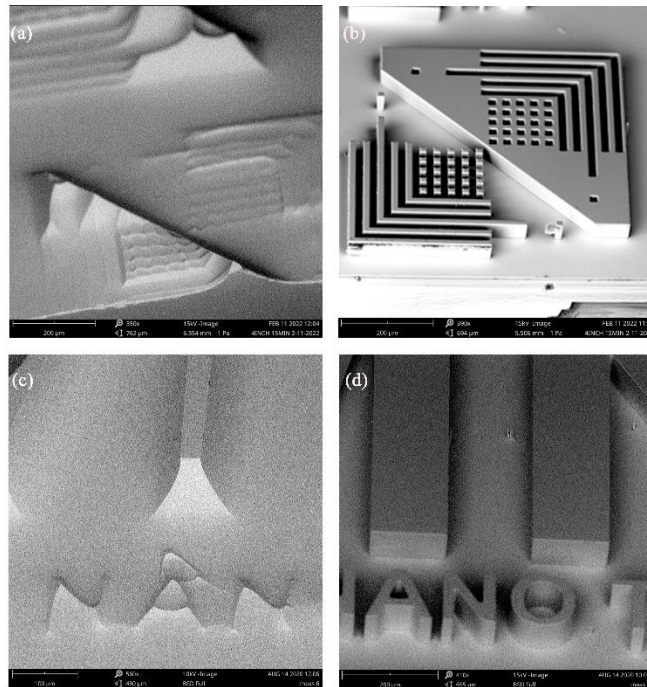


Figure 3.9 Using optimum recipe parameters - (a), (c) Etched structures with no fomblin oil (no cooling) (b), (d) Etched structures with fomblin oil.

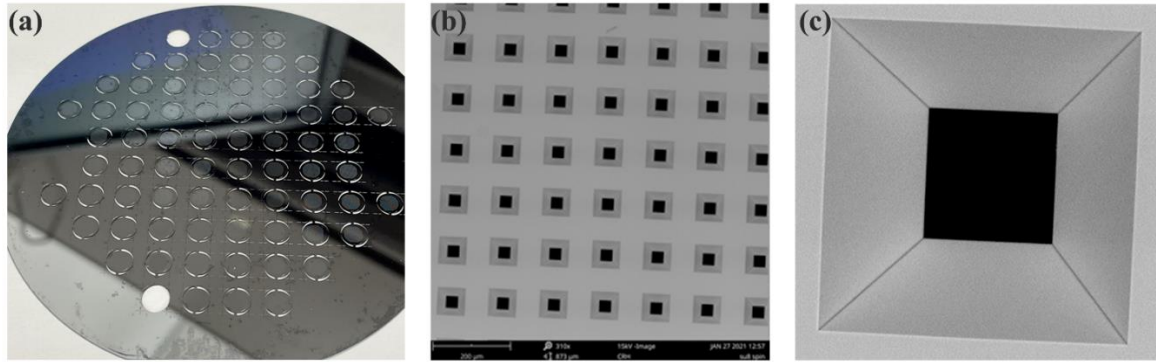


Figure 3.10 – (a) wafer with 80 fabricated atomizer devices, (b) SEM image of array of micro nozzles, (c) SEM image of individual KOH etched nozzle.

Figure 3.10(a) shows the finished 4-inch wafer consisting of 80 devices and figure 3.10(b, c) shows the SEM image of array of nozzle and individual cavity. The individual devices were removed by breaking the tethers. The assembled device consists of stainless-steel washer of 16.6mm OD and 3.5mm ID and PZT ring of OD 16 mm and ID 6 mm and MEMS device. Both the MEMS VMA and PZT rests on top of the stainless-steel washer holder and is bonded using conductive epoxy. Then, the wires are attached on the top of PZT ring and bottom of washer holder as they act as electrodes using the same conductive epoxy.

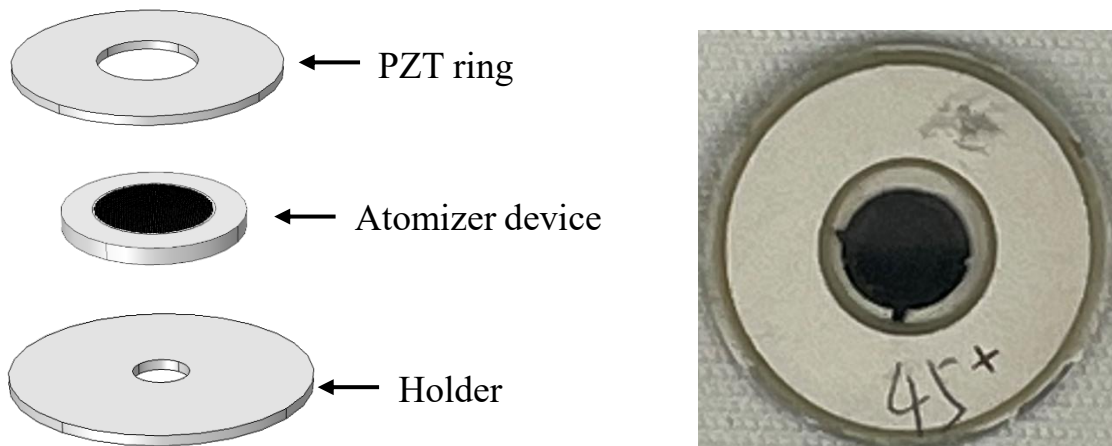


Figure 3.11 – Schematic and image of assembled device.

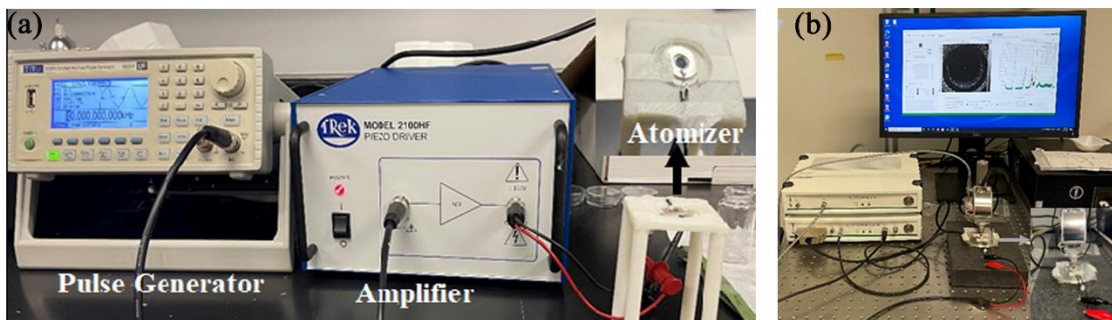
### **3.4 Experimental setup and Characterization of Vibrating mesh atomizer**

The setup for characterization of the fabricated device is discussed in this section. Then, for various liquids, tests are carried out to illustrate the basic functioning of liquid atomization. The requisite amplitude and frequency modes for aerosol production are determined and measured which gives the details of membrane velocity and acceleration. The spectrum of liquids that might be atomized with the standalone device is determined by testing variations in supply voltage and frequency.

#### **3.4.1. Experimental Setup**

A schematic and image of the experimental setup for power supply to the device is shown in figure 3.12(a). The microfabricated atomizer assembly is mounted over the 3D printed stand to hold the device still. To generate the appropriate waveform for driving the PZT actuator, a pulse generator (TG5011 AIM TII Instruments) is programmed to generate a sine waveform at particular frequency at a set amplitude. The frequency sweep is performed to determine the resonant frequency at which the device operates. The output of the function generator is connected to the amplifier (Model 2100HF Trek) with fixed gain of 50V/V and 150V peak voltage to amplify the waveform amplitude necessary to drive the piezoelectric actuator. Once the actuator is activated, the vibration in vertical direction ( $d_{33}$ ) is transferred to the membrane and the ones in lateral direction ( $d_{31}$ ) is negligible due to fixed boundary condition. The ejection cavity diameter expands which creates the positive pressure and pulls the fluid into the nozzle and when the pressure become negative for the negative part of the wave, the fluid is squeezed out in form of aerosols. A visual control was implemented to control and adjust the input parameters.

Figure 3.12(b) shows the image of the setup for measuring the vibration mode of the atomizer. The amplitude, mode shapes and frequency spectrum of the atomizer membrane with apertures is obtained using Picoscale vibrometer (SmarAct GmbH). It is a contactless laser-based method that measure displacement directly at any position on the device by creating an interference pattern of the reflected laser signal from the device surface and reflected signals obtained from beam splitter inside the laser head. To identify the resonance modes, the laser spot is initially positioned at the center of the membrane and series of its vibrations are recorded at a sampling rate of 5MHz. The vibrations are induced by shaker output connected to the amplifier to amplify the amplitude which further becomes the input to the atomizer device. The resultant output signal gives the details of the membrane resonating frequencies and displacement amplitude when measurements are carried in frequency domain setting. This helps the visualization of different vibrational modes of membrane. The velocity and acceleration information can also be achieved in time domain setting. The device is well focused before performing any measurements by creating Lissajous plot having a complete circle suggesting its fully focused. This can be achieved by adjusting z-axis of the laser head to find an optimal coordinates. Once, this plot is achieved the entire device is scanned optically to adjust the reflectivity of the surface, value less than 100% is preferred and considered optimum for further frequency and modal analysis.



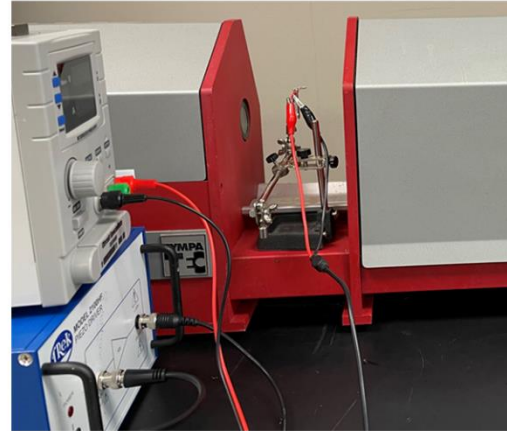
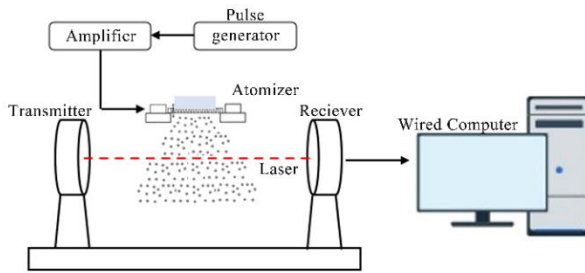


Figure 3.12 – Atomizer testing setup with pulse generator and piezo amplifier and atomizer device.

The particle or droplet size distribution is measured by using Sympatec HELOS system. The system uses laser diffraction in the parallel laser beam to evaluate the particle size distribution. R3 lens with a size range of  $0.9\mu\text{m}$  -  $175\mu\text{m}$  with universal dispenser for 1 sec measurement time. The atomizer device forming aerosols is placed between the laser beam as shown in figure 3.12(c) and the laser passes through the droplets which in results provides information about droplet size and distribution. The frequency and amplitude are set fixed for all the liquid testing. The measurements are done in triplets to reproduce the similar results.

### 3.4.2. Experimental Demonstration of Vibrating Mesh function

The ability of the vibrating mesh atomizer to generate aerosol is tested here. Initially, the devices are tested for water at  $20^{\circ}\text{C}$  and viscosity  $1\text{cP}$  and supply voltage of  $50\text{Vpp}$ . Figure 3.13 shows the aerosols out of the device. The liquid supply method can be either pipetting or using cotton wick as both the methods result in same flow rate and does not harm the atomization process.

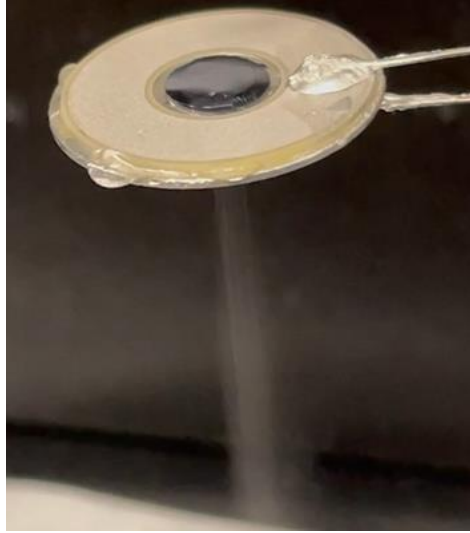


Figure 3.13 – Image showing aerosol generation from working atomizer.

### **3.4.3. Characterization of Atomizer**

The atomizer is characterized by determining the operating frequency range and droplet formation and atomization rate at the range of applied voltage. Atomization of various liquids are tested for aerosol generation and drop size distribution determination.

#### **3.4.3.1. Operating Frequency and Mode**

The frequency spectrum curve of the vibration amplitude for both the simulated FEM and experimental MEMS VMA device is shown in Figure 3.14. The vibrational modes with largest out of plane displacement were the (0,1) mode and (0,2) mode. The measurement results shows that the first resonant frequency (0,1) of the simulated device was 24.5 kHz while the next largest amplitude peak was observed at 99 kHz which corresponds to (0,2) mode. The other modes have lower out of plane displacement. The experimental frequency measurements of the MEMS VMA device were in good agreement with the FEM results as demonstrated. The results validate the accuracy of the FEM to the experimental work for analyzing mode shapes and frequencies. Experimentation on the MEMS VMA demonstrated that the device was not able to atomize water when operating in the (0,1) mode. The atomization of the liquid

gradually starts when the frequency approaches (0,2) mode i.e., between 95 kHz and 102 kHz. As the frequency was increased beyond 102 kHz the atomization rate decreased significantly. When the frequency increases, the nozzle membrane deformation becomes complex which means that the rate of deformation curvature changes increases that indicates that there is larger change in dynamic cone angle which makes the pumping effect more stronger and results in an increased atomization rate. So, elastic deformation and vibrations of the nozzle membrane allows the micro cone angle to act as pump in whole process of atomization. Increase in tapered aperture volume change supports more fluid to pump in and result in more atomization. Reduction of atomization at 115KHz and next resonant frequency can be due to two possible reasons. First being the overall displacement amplitude decreases which means that the rate of change decreases so, not enough pumping effect to perform the atomization process. Second reason is that the flow velocity in the nozzle apertures increases with the increasing frequency which may lead to increased flow resistance[57].

The atomization process of the MEMS VMA is determined by the velocity of the membrane which involves a combination of operating frequency and displacement of the membrane. For (0,1) mode, the peak displacement of the membrane was high ( $\sim 3 \mu\text{m}$  at 100 V) but the vibrational frequency was low, therefore no atomization was observed due to low velocity of the membrane and hence the liquid did not have enough momentum to break the surface tension force and form droplets. However, when the device was operated in the (0,2) mode, the frequency was higher (approximately 4x), but displacement was only slightly lower ( $\sim 2.1 \mu\text{m}$  at 100 V) resulting in higher velocity which had enough force to break the surface tension and produce atomization.

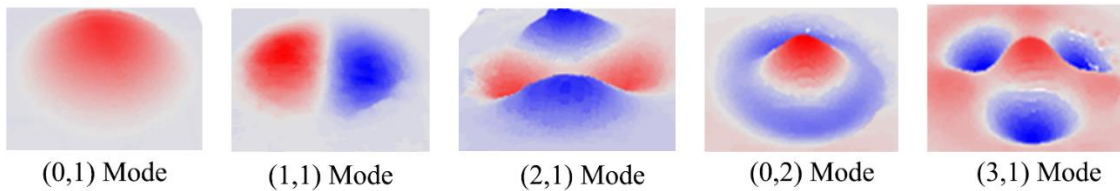
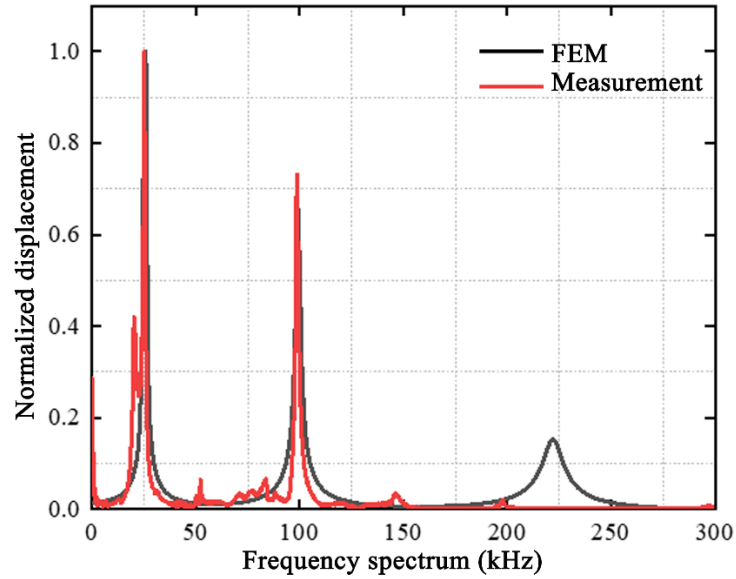


Figure 3.14 – Frequency spectrum of a vibrating mesh atomizer.

The velocity of the membrane as a function of frequency is shown in Figure 3.15 and it was demonstrated that the velocity was highest at the (0,2) mode frequency. The (0,1) mode velocity has the largest displacement, but the velocity was very low compared to (0,2) mode. The velocity at each mode follows the same curve as displacement resulting in the highest velocity at the center of the membrane and lower velocity/displacement at the edges. The maximum velocity at the center of the membrane varies linearly with varying voltage as demonstrated in Figure 3.15(b).

No atomization was observed below 30V which shows that the displacement and velocity were not enough to begin the droplet formation process and the velocity corresponding to 30V i.e., 1.02m/sec was measured as the threshold value for atomization of water. Therefore, velocity of the membrane near the center appears to be the critical feature that influences atomization.

The peak displacement of the MEMS VMA device when operating in the (0,2) mode was ( $\sim 2.01 \mu\text{m}$ ) at 100 V which agreed with FEM results ( $1.99 \mu\text{m}$ ) and it follows the same trend as shown in Figure 3.16(a). Other higher order frequency modes resulted in peak displacements in the nm range. The atomization rate was also affected by the operating parameters due to a change in volume of the apertures and the membrane due to varying displacement at different voltages. As shown in Figure 3.16(b) the atomization rate, using water as the working fluid, reached a maximum rate while the device operated in the (0,2) mode. The atomization of water started at 85 kHz and stopped at frequencies  $>117 \text{ kHz}$  due to altering the vibration mode and velocity of the membrane. At 85 kHz operating frequency the flow rate for water at 40 V input voltage was  $5.33 \mu\text{L}/\text{min}$  and increased to  $37.5 \mu\text{L}/\text{min}$  at 80 V. As the frequency was increased to the peak (0,2) mode operation the flow rate increased reaching a maximum flow rate at 99 kHz frequency, with a flow rate of  $12 \mu\text{L}/\text{min}$  at 30 V and  $265 \mu\text{L}/\text{min}$  at 80 V. At 117 kHz frequency the flow rate decreased to  $8.57 \mu\text{L}/\text{min}$  at 30 V and  $78.32 \mu\text{L}/\text{min}$  at 80 V. The flow rate was highly dependent on the dynamics of the membrane but also on the liquid and its properties such as surface tension, density and viscosity. Therefore, atomization of liquids with larger surface tension, density and viscosity will likely need higher velocity to atomize the liquid.

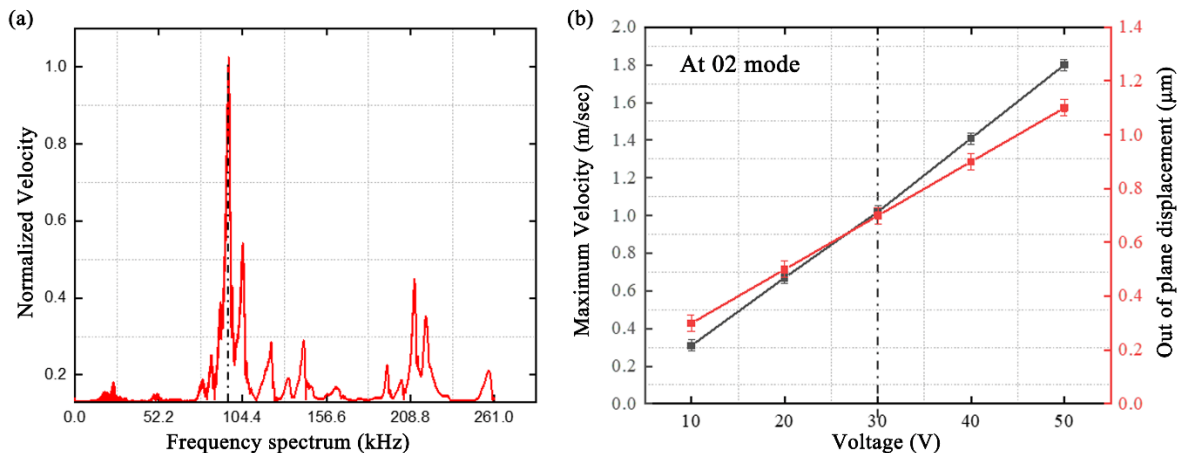


Figure 3.15 – Velocity measurement of the atomizer.

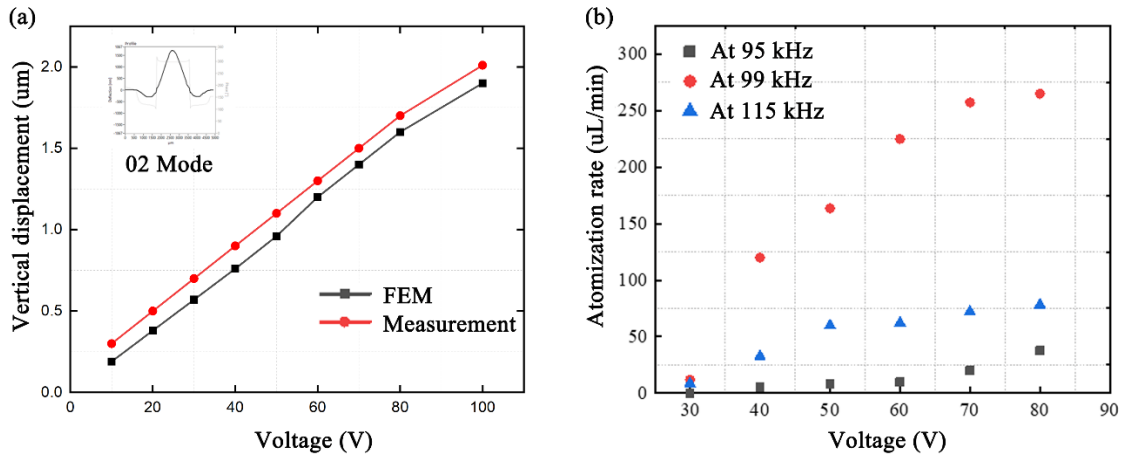


Figure 3.16– Comparison of measured deformation at different voltage with FEM results.

### 3.4.3.2 Droplet Distribution of Different Liquids

Droplet size distribution is the measure to determine the droplet sizes and density produced from any atomizer device. Droplet distribution was determined by the width of the distribution calculated by the Span number which is given by:

$$Span = \frac{X_{90} - X_{10}}{X_{50}} \quad (1)$$

Where  $X_{10}$ ,  $X_{50}$  and  $X_{90}$  represents droplet size distribution of 10%, 50% and 90% of total cumulative percentage of volume of all the droplets produced respectively. The Fine particle fraction (FPF) was defined as the fraction of droplets that had sizes between 1  $\mu\text{m}$  and 5  $\mu\text{m}$ . The volume median diameter (VMD) is the midpoint or median droplet size where half of the spray volume are smaller droplets and half are larger droplets.

The atomizer device operating at resonance frequency at 99KHz and driving voltage at 50Vpp for a variable hole size device is used to perform the droplet size distribution measurement for different liquids. For initial testing of the device low viscous liquids are chosen for different application such as DI water, Spin on Glass, photoresist SU-8, albuterol, water-based

cannabidiol solutions. Spin on glass is the solvent-based solution with Silicon dioxide mostly used as dielectric layer, sacrificial layer in microfabrication, SU-8 is the negative resist used in lithography process, both are used for additive manufacturing applications. An experimental based application study of spin on glass has been worked presented in later chapter. Albuterol is an inhalation drug used to treat bronchospasm, asthma, or chronic obstructive pulmonary diseases. CBD solutions (water and methanol based) can be used for therapeutic process as it has anti-inflammatory properties and is natural pain reliever.

A detailed comparative study based on the droplet size distribution has been performed using the fluids mentioned above and is discussed here.

### **3.5. Comparison of Silicon based and commercial vibrating mesh atomizer**

In this section, we investigated three types of atomizers initially i.e., Ultrasonic, commercial stainless steel VMA and MEMS based VMA based on droplet distribution and then later droplet size distribution for the two types of VMA is investigated for liquids with different physiochemical properties.

#### **3.5.1. Materials and methods**

The ultrasonic atomizer is based on the Faraday excitation principle, as illustrated in figure 3.17(a), and employs electronic high frequency oscillation to convert liquid into gas. Ultrasonic waves are created on the vibrating liquid by a piezoceramic transducer horn, and the vibration peak caused by the amplitude separates and splits the droplets from the surface. VMAs create droplets by vibrating a membrane with various apertures, as illustrated in figure 3.17(d). The membrane vibrates at a frequency of 100 kHz when driven by the piezoelectric actuator. The ultrasonic and metallic VMA were purchased from STEMiNC (Steiner and Martins Inc.). The ultrasound mist generator (SMUTK900LV110V, STEMiNC) operated at 1.7 MHz and two

types of stainless steel VMA were used with varying outlet nozzle size 10  $\mu\text{m}$  (SMMOD20F113H10, STEMiNC) and 5  $\mu\text{m}$  (SMMOD10F190, STEMiNC) and had a (0,2) resonant frequency mode of 113 kHz and 190 kHz respectively are used for this study.

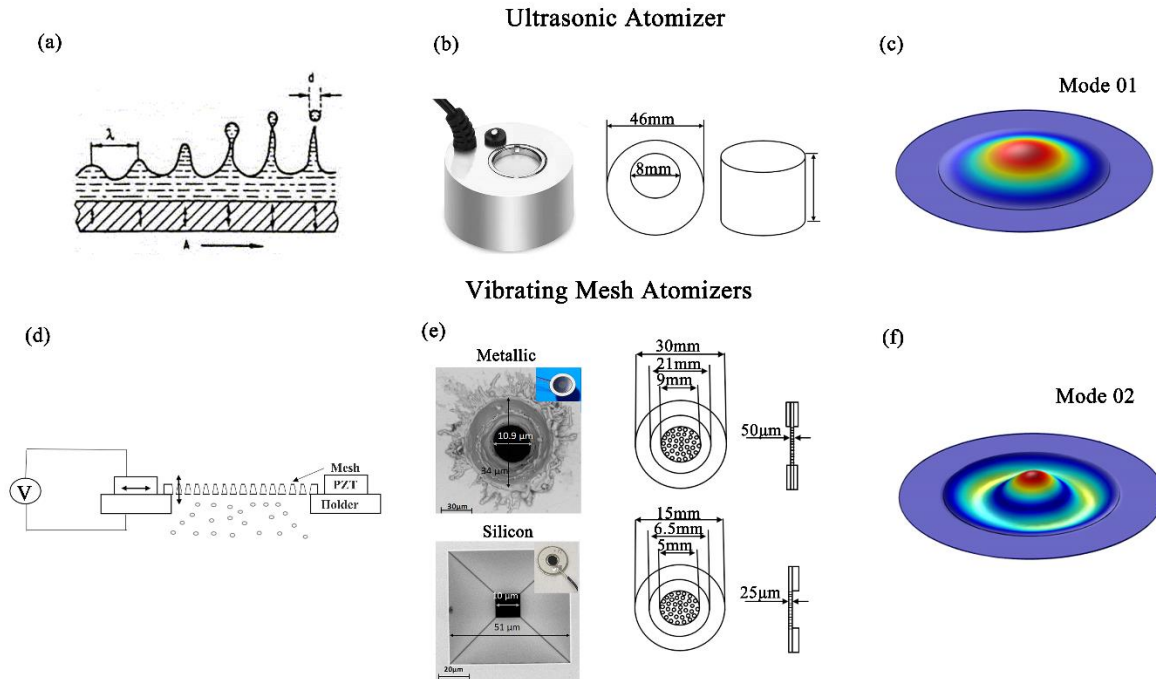


Figure 3.17 - Atomizer type investigated. (a, b) Working principle of ultrasonic mist maker and device image, (c) Vibrational mode of ultrasonic device (0,1), (d) Working principle of vibrating mesh atomizer, (e) SEM image of single nozzle - metallic VMA and MEMS VMA, (f) Vibrational mode of VMA device (0,2).



Figure 3.18 –Nozzle outlet shape of (a) MEMS VMA and (b) Metallic VMA.

Initially all three types of atomizers i.e., ultrasonic, VMA (metallic and MEMS) with orifice diameter 10  $\mu\text{m}$  were tested with DI water. The ultrasonic atomizer was placed 10 cm below the laser beam due to size of the ultrasonic mister and the two VMA were placed 1 cm above the laser beam as it was the optimum place of measurement. Based on the results obtained, the two VMA were selected for further investigation, whereas the ultrasonic device produced both ultrafine ( $< 1 \mu\text{m}$ ) and large particles ( $>100 \mu\text{m}$ ) and therefore was not selected for further investigation. Four different liquids with different properties such as DI water, Albuterol, 20% Glycerol, and 10% Cannabidiol water-based liquid isolate (Mile High Labs) were systematically investigated for droplet distribution, VMD, and flow rate for the two VMA devices. The temperature profile of the two VMA was measured using an IR microscope camera (Optris Pi640). The heating rate was determined by measuring the peak temperature across the membrane as a function of time. The viscosity of the liquids was measured using a Cannon-Fenske viscosity tube. The surface tension of the liquids was measured using a goniometer (Ossila).

### **3.5.2 Droplet distribution results**

Initial droplet distribution of three different atomizers (ultrasonic, metallic VMA, and MEMS VMA) were investigated using DI water and the results are demonstrated in Figure 3.19. Both types of VMA had an outlet nozzle of 10  $\mu\text{m}$ . In the case of ultrasonic device, the  $X_{10}$  was 1.71  $\mu\text{m}$ ,  $X_{50}$  was 123.78  $\mu\text{m}$  and  $X_{90}$  was 142.36  $\mu\text{m}$  resulting in a VMD of 90.04  $\mu\text{m}$ . This demonstrates the droplets produced by ultrasonic atomization were either ultra-fine  $<1 \mu\text{m}$  or very large  $>100 \mu\text{m}$ , representing a very wide distribution. Therefore, the ultrasonic atomization method is not ideal for applications requiring small droplet distribution. The ultrasonic devices readily available on the market guarantee droplets with a size of less than

5 $\mu$ m because the system includes a baffle, an additional system component that functions as a filter to prevent big droplets from escaping the device; however, no baffle is employed in this investigation. Mesh atomizers are beneficial over ultrasonic atomizers due to their capacity to produce output droplets smaller than 5 $\mu$ m without requiring a baffle as a subcomponent. The characteristics of devices tested is summarized in table 1 which clearly shows ultrasonic atomizer is more power consuming than other two atomizers. The ultrasonic atomization was therefore not further investigated due to the wide droplet distribution, its inability to atomize higher viscosity liquids, and high-power consumption. The metallic VMA had a droplet distribution where  $X_{10}$  was 8.59  $\mu$ m,  $X_{50}$  was 17.10  $\mu$ m, and  $X_{90}$  was 30.68  $\mu$ m resulting in a VMD of 18.73  $\mu$ m. The VMD and  $X_{50}$  were larger than the outlet nozzle dimension of 10  $\mu$ m. The MEMS VMA had droplet distribution where  $X_{10}$  was 4.30  $\mu$ m,  $X_{50}$  was 7  $\mu$ m, and  $X_{90}$  was 13.64  $\mu$ m resulting in a VMD of 8.33  $\mu$ m. Unlike the metallic VMA the VMD and  $X_{50}$  of the MEMS-VMA was smaller than the nozzle diameter of 10  $\mu$ m. Figure 4(c) demonstrates a much narrower distribution compared to the other atomization methods for DI water. Therefore, initial results with DI water demonstrate a significant enhancement in droplet size distribution for the Si-MEMS VMA compared to metallic VMA and ultrasonics. The nozzles of the two VMA devices before any atomization are shown in Figure 1(e). The MEMS-VMA was visually much smoother due to the KOH etching compared to the metallic VMA which resulted in significant residue and surface roughness around the nozzle. The roughness could result in poor surface tension control thus affecting the droplet properties.

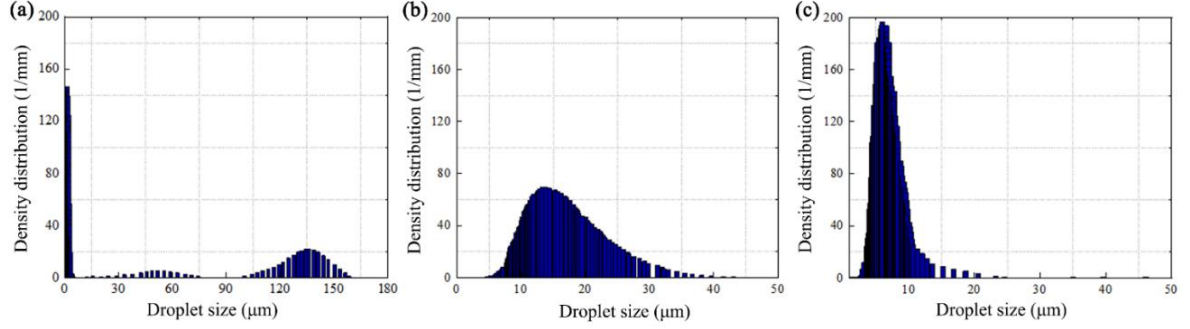


Figure 3.19. DI water droplet distribution by devices (a) ultrasonic device, (b) Metallic VMA and (c) MEMS VMA.

Both VMA devices follow a normal distribution where the probability density function of a normal random variable is given by

$$f(x|\mu, \sigma^2) = \frac{1}{\sqrt{2\pi}\sigma} e^{-\frac{(x-\mu)^2}{2\sigma^2}}, \quad -\infty < x < \infty, \quad -\infty < \mu < \infty, \quad \sigma > 0 \quad (2)$$

Where  $E(X) = \mu$  and  $\text{Var}(X) = \sigma^2$ .

### 3.5.2.1 Comparison of vibration dynamics of VMA Devices

The global deformation in the membrane defines the change in micro aperture angle and atomization rate by affecting the volume change at the liquid chamber [58]. The experimental vibration modes corresponding to resonance frequency of various modes are presented in Figure 3.20 for VMA devices. The frequency spectrum for metallic VMA shows multiple peaks indicating the displacement of the membrane at different frequencies. The first resonant frequency (01) mode was observed at 25 kHz followed by the (11) mode at 60 kHz. The VMA operates in the (02) without liquid and (03) mode with a liquid load [59]. The atomization frequency range was thus approximately 93-113 kHz for the metallic VMA. The MEMS VMA was designed to have similar dynamics as the metallic in order to compare device performance without affecting the atomization dynamics. The (01) resonant mode was measured at 23 kHz compared to the metallic at 25 kHz. The (02) mode was measured at 99 kHz for the MEMS-

VMA. The atomization mode for both devices had an operation of approximately 100 kHz. The MEMS-VMA dynamics could be easily altered by changing the dimension or thickness of the silicon membrane. Fine tuning of the silicon membrane could be accomplished by controlling the thermally grown oxide thickness which consumes 46% of the silicon. The number of nozzles also slightly affects the stiffness and can be used to fine tune the resonant frequency.

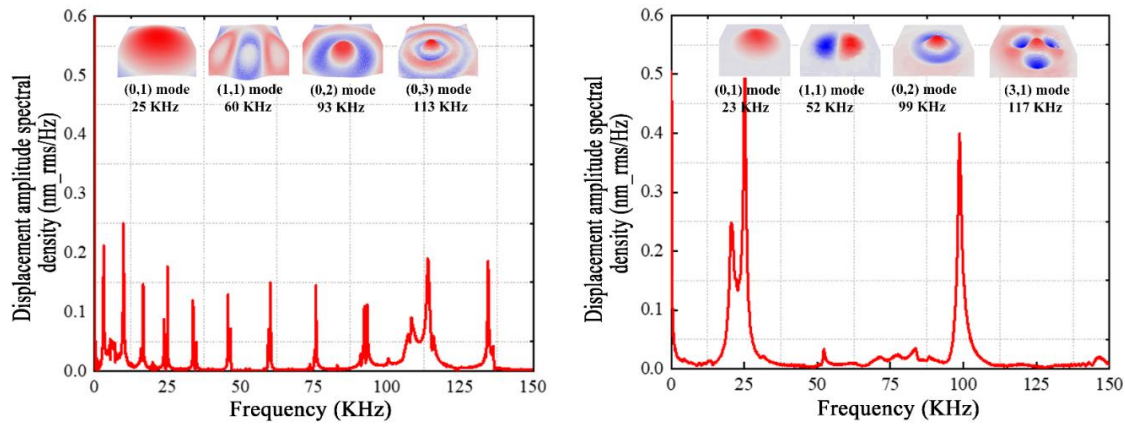


Figure 3.20. Frequency spectrum of (a) Metallic VMA, (b) MEMS VMA.

No atomization was observed when the VMA devices were operated in the (01) mode, but this mode was used in the ultrasonic device which operated at significantly higher frequency than the VMA. The VMA started to atomize liquid when the frequency approached the (02) mode (~85 kHz) and was maximum between 90 kHz and 102 kHz for the MEMS VMA and near 100 kHz for metallic VMA. Further increasing the frequency resulted in a significant decrease in atomization as the dynamics changed to the (31) mode. The frequency increase caused the deformation of the membrane to become complex, which causes the rate of deformation curvature to increase. This indicates that there was a larger change in the dynamic cone angle which makes the pumping effect stronger and affects atomization rate. Elastic deformation and vibrations of the nozzle membrane allows the micro cone angle to act as pump during the

atomization process. Increasing the tapered aperture volume requires more fluid to be pumped in which results in larger and wide range of droplet formation. This is demonstrated by the larger droplet distribution of the metallic VMA compared to the MEMS VMA, as the metallic VMA has a much wider taper than the MEMS VMA (54.74°).

### 3.5.2.2 Droplet Size distribution of metallic VMA and MEMS VMA

Table 3.4 demonstrates the physiochemical properties of the liquids investigated. Each liquid had relatively low viscosity (< 3 cP). The water-based CBD had the lowest density and surface tension but the highest viscosity. Low viscosity liquids were investigated as previous studies have determined that the atomization of metallic VMA were limited to viscosities [60] of <2 cP. However, density and surface tension also have a significant impact on the atomization capability.

Table 3.4. Physiochemical properties of the liquids used.

Liquid	Density (kg/m <sup>3</sup> )	Viscosity (cP)	Surface tension (mN/m)
DI water	997	0.9	72.7
Albuterol	1000	1	72.7
20% Glycerol	1039	1.87	71
10% CBD W-B	807	2.69	53.5

The droplet distribution of the atomized liquids listed in Table 3.4 from both the metallic and the MEMS VMA devices is shown in Figure 3.22(a-d). The devices were operated at the same frequency (100 kHz) and same drive voltage (50 V<sub>pp</sub>), both devices had an outlet nozzle size of 5 μm, and similar peak displacement. The results of the width of the size distribution (span) and FPF are shown in Table 3.5. The span of the metallic device was approximately 1 across

all liquids with an average span of 1.023, but median droplet size increased as the viscosity increased. The MEMS-VMA device had a significantly lower span with an average of 0.54 for low viscosity (< 2 cP) liquids with no significant change in median droplet size. The span increased for the water-based CBD, which is believed to be due to the increase in viscosity and particles within the liquid. The difference in VMD for both the devices could be explained by their change in volume in the chamber created by the thin film vibration which depends on oscillation frequency, nozzle diameter and thickness of the membrane [61]. The total volume change in the cone apertures is given by equation 3[62] where, where h is the thickness of the membrane,  $\alpha$  is the angle between the taper hole line and surface normal,  $\theta_{down}$  is the increase in  $\alpha$  during positive cycle (bending downwards) and  $\theta_{up}$  is the decrease in  $\alpha$  during negative cycle (bending upwards).

$$\Delta V = \frac{\pi h^3}{16} [\tan^2(\alpha + \theta_{down}) - \tan^2(\alpha + \theta_{up})] \quad (3)$$

$$Q = \Delta V n f \frac{\overline{\xi(x)}_- - \overline{\xi(x)}_+}{2 + \overline{\xi(x)}_- + \overline{\xi(x)}_+} \quad (4)$$

$$\xi_{(x)+} = \frac{1}{T} \int_0^T \xi_{(x)+} dT \quad (5)$$

$$\xi_{(x)-} = \frac{1}{T} \int_0^T \xi_{(x)-} dT \quad (6)$$

And the flow rate is given by equation 4[63], where  $\Delta V$  is the volume change in the micro cone, f is the operating frequency, n is number of apertures and h is the thickness of the membrane and  $\overline{\xi(x)}_+$  and  $\overline{\xi(x)}_-$  are average flow resistance during positive (forward) and negative (reverse) cycle calculated by equation 5 and 6.  $\xi_{(x)+}$  and  $\xi_{(x)-}$  nozzle loss coefficients during positive and negative cycle and their values can be interpreted by the curve shown in figure 3.21. These flow resistance values depend on the taper angle of the micro-cone shows that the flow resistance is greater when the taper angle is greater than 30° and hence, the flow

through the nozzle with taper angle greater than  $30^\circ$  is less than the nozzle with taper angle less than  $30^\circ$ .

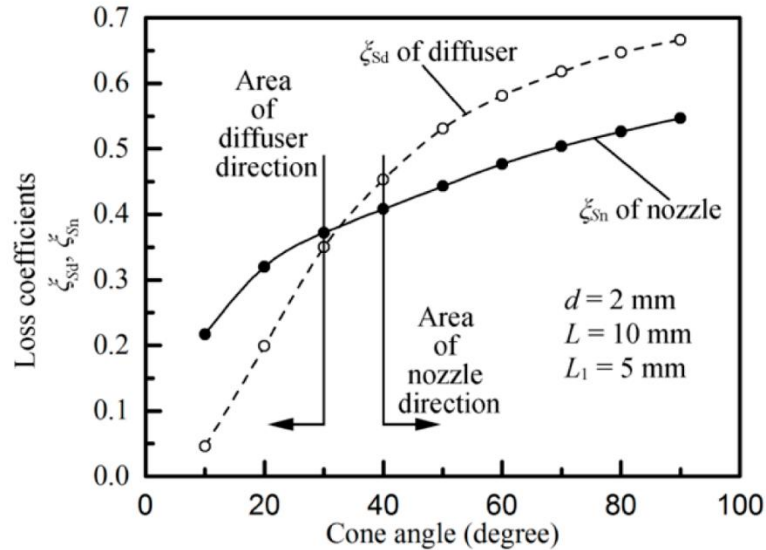


Figure 3.21 – Empirical curves of cone angle and loss coefficients in the nozzle.

The difference in taper angle and thickness of the two devices are responsible for change in volume of the liquid pumped in at each cycle and also changes the flow resistance values. Commercial atomizer taper angle ( $\alpha$ ) is  $11.3^\circ$  with thickness of  $50\mu\text{m}$  has low flow resistance in comparison to MEMS atomizer with a taper angle ( $\alpha$ ) of  $35.5^\circ$  and thickness of  $25\mu\text{m}$ . The difference in operating frequency, which is  $190\text{kHz}$  for the metallic atomizer and  $99\text{kHz}$  for the MEMS atomizer, may also explain the wide dispersion of droplets and larger VMD of the metallic atomizer, as total flow is dependent on frequency, change in volume of each cone per cycle, and flow resistance values.

Thickness of the metallic membrane ( $\sim 50\mu\text{m}$ ) was thicker than the MEMS device ( $25\mu\text{m}$ ) so, with each cycle of the oscillation the metallic VMA pumps and pushes out more liquid than the MEMS VMA, resulting in wide distribution of droplets and larger VMD. The FPF was

significantly higher (4.22x, 3.84x, 14.1x, and 15.6x) for the MEMS VMA compared to the metallic VMA for water, Albuterol, 20% Glycerol and 10% CBD respectively. The FPF decreases as the viscosity increases for both devices, but the decrease is less significant with the MEMS-VMA, which means the MEMS-VMA could be better at controlling droplet distribution of higher viscous liquids. The FPF reduces with increased viscosity as larger force is needed to squeeze the higher viscosity liquids through the nozzle, but if the force is constant then droplets increase in size until the forces can overcome viscosity. The MEMS device has a narrower and more controlled droplet distribution and VMD which is nearly equal to the outlet dimension, resulting in higher FPF. Figure 3.22 demonstrates that in all cases the MEMS-VMA resulted in enhanced size distribution and smaller VMD when compared to metallic VMA.

Table 3.5. Comparing Span and FPF for metallic and MEMS VMA devices.

Liquids	Span		Fine particle fraction (%)		VMD ( $\mu\text{m}$ )	
	Metallic	MEMS	Metallic	MEMS	Metallic	MEMS
DI water	1.06	0.59	22	93	7.6 $\pm$ 0.3	5.79 $\pm$ 0.4
Albuterol	1.09	0.54	25	96	8.1 $\pm$ 0.2	5.82 $\pm$ 0.3
20% Glycerol	0.96	0.49	6.1	86	14.37 $\pm$ 0.6	5.16 $\pm$ 0.5
10% CBD W-B	0.98	1.02	3.52	55	15.72 $\pm$ 0.4	5.8 $\pm$ 0.6

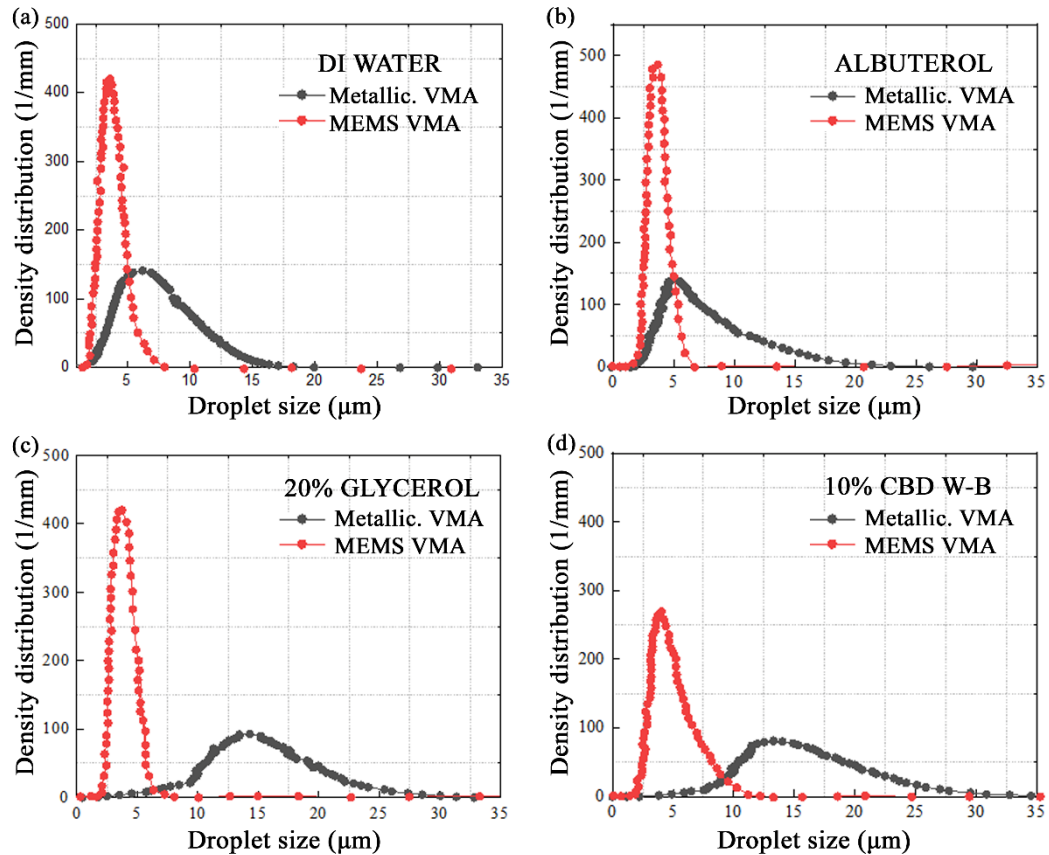


Figure 3.22. Droplet distribution for Metallic and MEMS VMA for (a) DI water, (b) Albuterol, (c) 20% Glycerol and (d) 10% CBD Water-based.

Liquids with varying fluid properties were investigated to determine the effect of fluid viscosity. For the metallic device, fluid viscosity was inversely proportional to the VMD of the droplets produced which was in good agreement with the results shown previously [17] whereas the MEMS VMA was not significantly affected by the fluid viscosity in regards to the VMD. Even though both devices have the same working principle, frequency, outlet nozzle size, and displacement amplitude they produced different droplet distribution results with varying liquids. This is believed to be due to i) varying nozzle shape, ii) mechanical properties of silicon compared to stainless steel, and iii) surface roughness. The MEMS VMA produced

more uniform droplet sizes and was able to have increased control across a wider range of viscosities. Figure 3.23 demonstrates the VMD for the two devices with varying liquids. As the viscosity was increased beyond 1 cP the VMD increased significantly for the metallic VMA whereas the viscosity had little impact on the VMD for the MEMS-VMA. This demonstrates that the MEMS-VMA could potentially atomize higher viscosity liquids with narrow droplet size distribution.

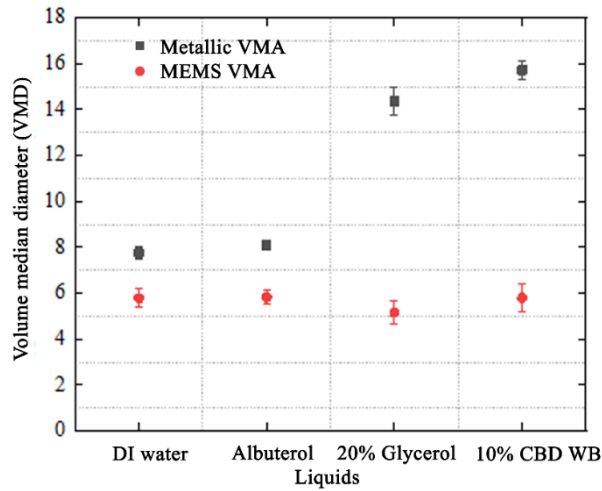


Figure 3.23. VMD of two devices used for DI water, Albuterol, 20% Glycerol and 10% CBD W-B.

The data was statistically analyzed using an ANOVA (Analysis of Variance) model. Multiple comparisons were made using Tukey’s simultaneous confidence intervals and insights on best performing factor levels was provided. Analysis of the experimental design requires fixed effect 3-factor ANOVA model [64, 65]. Device factor was set at 2 levels: (1) MEMS and (2) metallic. Outlet nozzle size diameter was at 4 levels: (1) 5  $\mu\text{m}$ , (2) 10  $\mu\text{m}$ , (3) 20  $\mu\text{m}$ , and (4) 30  $\mu\text{m}$ . Liquid factor was at 4 levels: (1) DI water, (2) albuterol, (3) 20% glycerol and (4) CBD 10 % W-B. An additive ANOVA model shown in equation (3) along with the Hasse diagram demonstrated in Figure 3.24 summarizes the design of experiment.

$$Y_{ijklt} = \mu_{..} + \alpha_i + \beta_j + \gamma_k + \varepsilon_{ijklt} \quad \text{where } i = [1, 2], j = [1, 2, 3, 4], k = [1, 2, 3, 4], t = \{1, 2, \dots, 32\}, \sum_{i=1}^2 \alpha_i = \sum_{j=1}^4 \beta_j = \sum_{k=1}^4 \gamma_k = \sum_{i=1}^4 (\alpha\beta)_{ij} = 0, \varepsilon \sim iid N(0, \sigma^2). \quad (3)$$

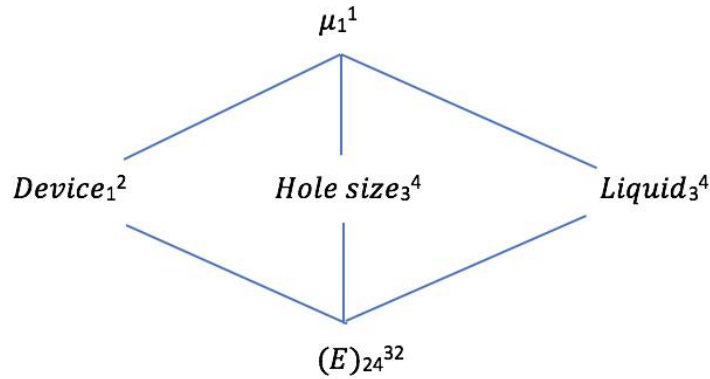


Figure 3.24. Hasse diagram for VMD experiment.

Where  $\alpha_i$  is the main effect due to  $i^{th}$  device,  $\beta_j$  is the main effect of  $j^{th}$  hole size,  $\gamma_k$  is the main effect due to  $k^{th}$  liquid. Analysis at 5% experimental error demonstrates that i) main effect due to device and outlet nozzle size on VMD are both statistically significant, while the main effect due to liquid was statistically insignificant and 2) metallic devices have larger VMD than MEMS based device. A 95% Tukey's confidence interval with a difference of (2.79, 7.79). Pairwise comparisons of outlet nozzle size using Tukey's procedure are shown in Table 3.6.

Table 3.6. Pairwise comparisons of hole size factor levels. Case 6 implies that hole size of 30  $\mu\text{m}$  produces higher VMD compared to hole size diameter of 20  $\mu\text{m}$ .

Case	Hole size $\mu\text{m}$	Result	Hole size $\mu\text{m}$	95% CI for difference
1	10	Higher VMD	5	(0.16, 9.62)
2	20	Higher VMD	5	(9.95, 19.41)
3	30	Higher VMD	5	(22.15, 31.61)
4	20	Higher VMD	10	(5.06, 14.51)

5	30	Higher VMD	10	(17.26, 26.71)
6	30	Higher VMD	20	(7.47, 16.92)

The flow rate of the VMA devices as a function of applied voltage at (02) resonance frequency mode was investigated, and the results are shown in Figure 3.25(a, b). The results demonstrate that as driving voltage increases the flow rate for both devices increase. As voltage increases the peak displacement of the membrane increases from 1.2  $\mu\text{m}$  at 50  $V_{pp}$  to 2.29  $\mu\text{m}$  at 100  $V_{pp}$ . As the mesh membrane deformation increases the variation in the tapered volume exerts more pumping effect leading to higher atomization rates. The flow rate of DI water and albuterol was  $50 \pm 2 \mu\text{L}/\text{min}$  at 50  $V_{pp}$  for both devices and reaches  $170 \pm 5 \mu\text{L}/\text{min}$  for metallic VMA and  $130 \pm 5 \mu\text{L}/\text{min}$  for MEMS VMA at 100  $V_{pp}$ . The flow rates for 20% glycerol were  $30 \pm 3 \mu\text{L}/\text{min}$  for both devices at 50  $V_{pp}$  and reaches  $120 \pm 3.5 \mu\text{L}/\text{min}$  for metallic VMA and  $80 \pm 3.5 \mu\text{L}/\text{min}$  for the MEMS VMA at 100  $V_{pp}$ . For 10% CBD the flow rate was reduced to  $24 \pm 1 \mu\text{L}/\text{min}$  at 40  $V_{pp}$  and increased to  $75 \pm 2 \mu\text{L}/\text{min}$  for metallic device and  $54 \pm 3 \mu\text{L}/\text{min}$  for the MEMS VMA. The flow rate of low viscosity, low density liquid was the same for both the devices at low voltages but at higher voltages the metallic VMA had slightly higher flow rate ( $\sim 30 \mu\text{L}/\text{min}$ ) because the droplet distribution was wider, and the droplets produced were larger in size in comparison to the MEMS VMA. The increased liquid viscosity resulted in decreased flow rate for both devices.

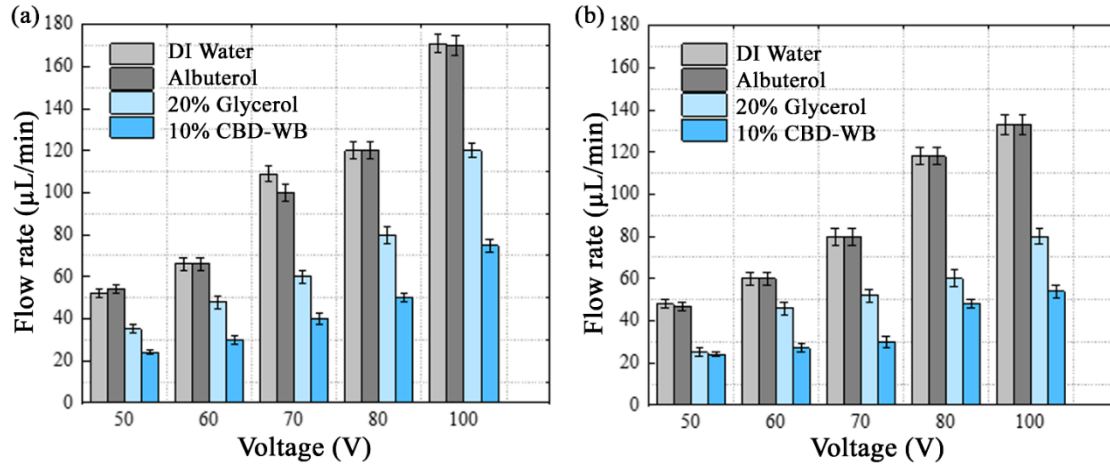


Figure 3.25. Flow rate of (a) Metallic VMA and (b) MEMS VMA.

Based on the results the MEMS VMA demonstrated significantly enhanced droplet distribution, VMD, and FPF for various liquids with different physiochemical properties. The MEMS VMA was selected for further investigation to determine effects of varying the outlet nozzle diameter, pitch of the inlet nozzles and distance of measurement from the laser source on droplet distribution. Outlet diameter was varied by changing the mask dimensions, but the taper remained the same. The various outlet nozzles investigated had dimensions of  $4\ \mu\text{m}$ ,  $6\ \mu\text{m}$ ,  $8\ \mu\text{m}$ , and  $10\ \mu\text{m}$ . The droplet distribution and VMD of the varying outlet dimensions of the MEMS VMA are shown in Figure 3.26(a). The distribution curve shifts to the left (smaller) as the outlet nozzle was reduced. The peak value of the distribution curve had similar size as the outlet nozzle dimensions. The  $4\ \mu\text{m}$  nozzle had a VMD of  $4.53\ \mu\text{m}$  and as the nozzle diameter increases the distribution curve shifts away from the axis. Figure 3.26(b) demonstrates the VMD as a function of outlet nozzle, which demonstrates a linear relationship for various liquids. The VMD value was in range of  $4.53\pm 0.4\ \mu\text{m}$  to  $5.43\pm 0.4\ \mu\text{m}$  for the  $4\ \mu\text{m}$  nozzle size,  $6.08\pm 0.5\ \mu\text{m}$  to  $6.46\pm 0.5\ \mu\text{m}$  for  $6\ \mu\text{m}$  size,  $7.92\pm 0.3$  to  $8.91\pm 0.3\ \mu\text{m}$  for  $8\ \mu\text{m}$  size,  $9.23\pm 0.5\ \mu\text{m}$  to  $11.2\pm 0.4\ \mu\text{m}$  for  $10\ \mu\text{m}$  size. This demonstrates that as outlet nozzle

increases the distribution of the VMD becomes wider along with an increase in VMD size. Therefore, the MEMS VMA device was able to have a narrower droplet size distribution, as the outlet nozzle dimensions can be very accurately produced with high reliability, as it is dependent on the anisotropic etching of silicon for which the taper depends on the crystal planes. The (100) crystal plane intersects the (111) plane at  $(54.74^\circ)$  which is the angle of the taper, because the KOH etching is negligible for the (111) plane. Thus, the taper of (100) Si is always going to produce a  $54.74^\circ$  angle, so by altering the mask dimensions the outlet nozzle can be accurately predicted and is very repeatable.

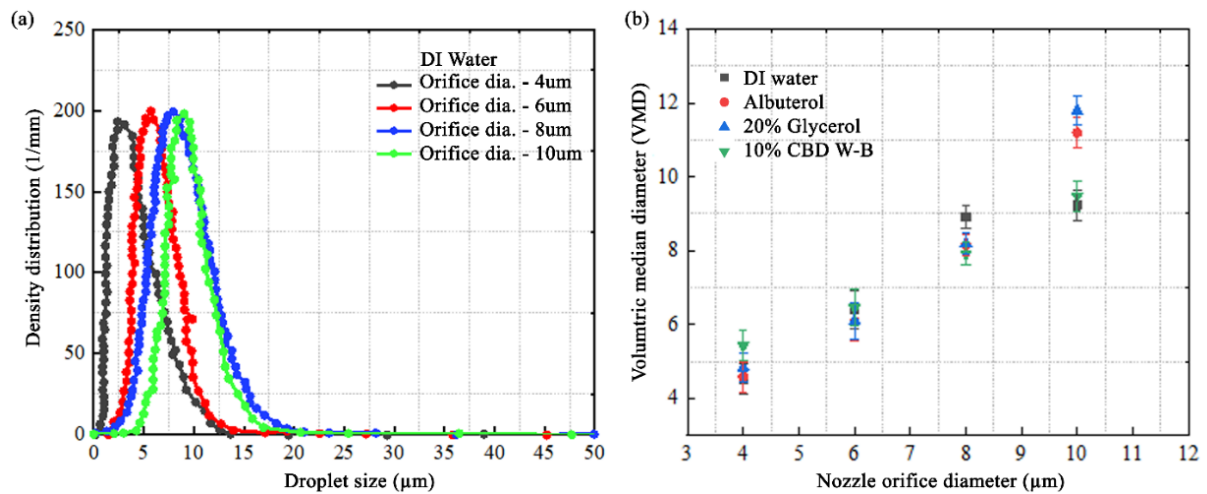


Figure 3.26. Effect of orifice outlet diameter on (a) Droplet distribution and (b) VMD.

The effects of nozzle pitch on distribution were investigated for the MEMS VMA device with  $4 \mu\text{m}$  nozzle size and the results are shown in Figure 3.27(a). The results demonstrate that the device with  $60 \mu\text{m}$  pitch had narrow distribution with span of 0.63. The distribution widens as the pitch was increased to  $90 \mu\text{m}$  and  $120 \mu\text{m}$  with a span of 1.16 and 1.2 respectively. This agrees with the metallic VMA devices which had a larger span and larger pitch than the Si-VMA. Nozzle pitch was also directly related to the number of nozzles on the membrane as lower pitch values correspond to more holes ( $4000$  holes for  $60 \mu\text{m}$  pitch) compared to  $2000$

and 1000 holes for 90  $\mu\text{m}$  and 120  $\mu\text{m}$  pitch. The distance of VMA to the laser on the particle analyzer results in varying VMD as demonstrated in Figure 3.27(b). If the VMA was positioned close to the laser the VMD results were lower than if the device was positioned approximately 30 mm away. This was likely due to coalescing of multiple small droplets resulting in large droplet formation.

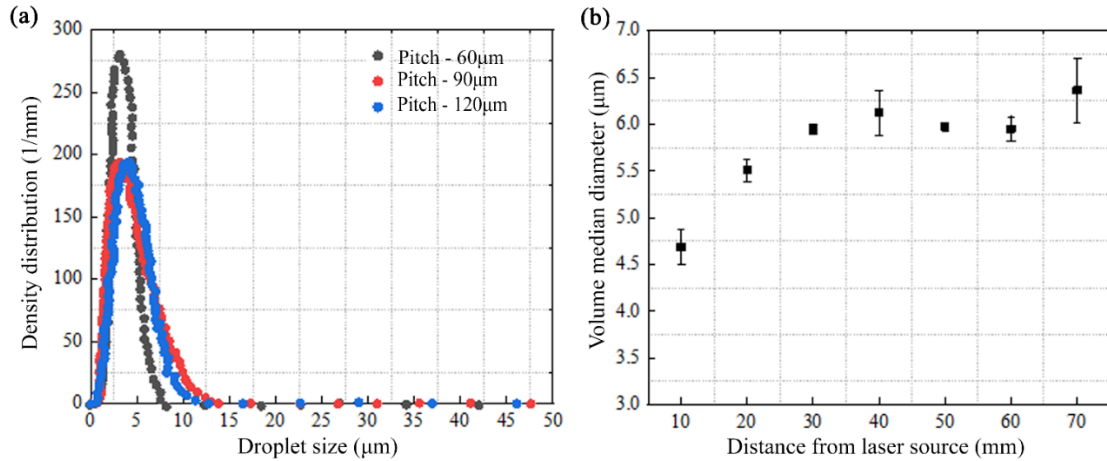


Figure 3.27. (a) Effect of hole pitch on the droplet distribution , (b) Distance of device from laser source on VMD.

### 3.5.2.3 Temperature Distribution

Temperature of the membrane through friction and piezoelectric material can affect the liquid properties and lead to degradation of the liquid or change the chemical composition of the liquid. Average temperature distribution across the membrane of the two VMA devices was investigated at a driving voltage of 50  $V_{pp}$ , and the results are shown in Figure 3.28(a-c). The heat from the piezoelectric actuation causes a significant increase in the metallic VMA, which reached an average temperature of 87.9 $^{\circ}\text{C}$  in about 40 s. This is significantly higher than the heating of the MEMS VMA (34.6 $^{\circ}\text{C}$ ) for the same duration. This is believed to be due to the difference in thermal conductivity difference of the two materials and to the bonding mechanism. The heat transfer rate was demonstrated in Figure 3.28(c). Increased surface

temperature for the atomizer device can affect the liquid as it may react and deteriorate the physical and chemical properties therefore the use of metallic VMA may not be suitable for certain liquids and applications as it could lead to degradation of the liquid. The heating was less controllable compared to the MEMS VMA.

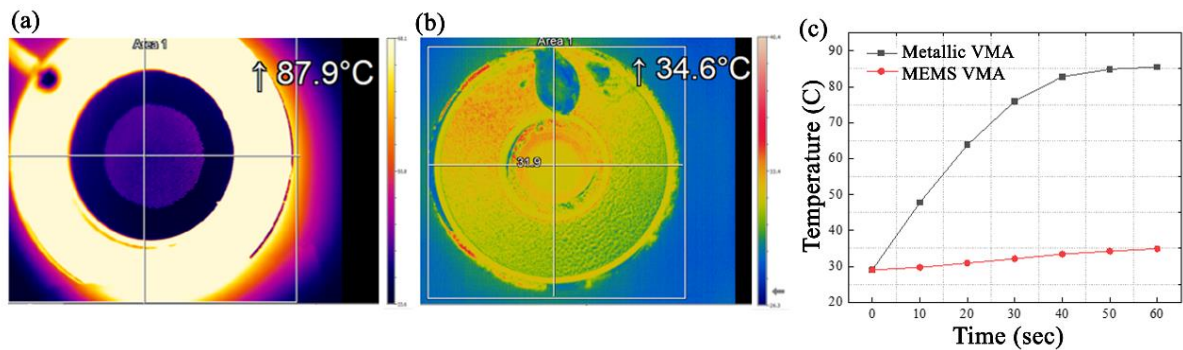


Figure 3.28. Surface temperature of (a) metallic VMA, (b) MEMS VMA, (c) Time temperature for both the device after 1 minute of operation.

### 3.6 Summary

This chapter presents the microfabrication process and characterization of the studied vibrating mesh atomizer. The atomizer device's microfabrication is economical compared to the other atomizer techniques and commercially available vibrating mesh atomizer with a metal mesh membrane. A wafer with 70 atomizer devices processing costs approximately \$100 in university laboratory fabrication per wafer, i.e., \$1.42 per device compared to a \$20 commercial device. So, it has the potential to reduce the total cost and has a high yield, high volume, and uniform process.

The characterization of the fabricated device in terms of operating frequency, membrane deformation, and atomization process is also presented here. These devices can atomize a variety of liquids such as DI water, photoresist, inhalation drugs, and droplet size distribution shows that more than 50% of the volume of the droplets is the same as the orifice diameter.

Later in the chapter, three types of atomizers, including ultrasonic, metallic VMA, and MEMS VMA, were investigated. The results demonstrate that the ultrasonic device produced a wide range of droplet sizes and could not atomize higher viscosity liquids, which agrees with previous research. The VMA devices were compared dynamically to have similar frequency modes and displacement with applied voltages. However, the material, thickness, nozzle shape, outlet nozzle shape, and surface roughness varied. These variations lead to statistically significant effects on droplet size, distribution, and device performance.

The aerosol performance, including droplet size distribution, VMD, and output rate, was dependent on fluid characteristics for both VMA devices. Regardless of the fluid, the metallic VMA generated aerosols with broader distribution, larger VMD, and smaller FPF than MEMS VMA. For MEMS VMA, droplet size did not change with varying viscosity, but the output rate was decreased due to flow resistance. The flow rates were significantly reduced for higher viscosity liquids in both devices. Further studies on MEMS VMA were carried out to study the effects of outlet nozzle size, pitch, and measurement distance from the laser source on the VMD. Outlet nozzle size and median drop size follow a linear relationship for all the liquids tested, and the average drop size corresponds to the outlet nozzle size. Since the MEMS VMA was fabricated in a clean-room environment, it can be customized and the pitch size of the nozzles could be varied. Varying the pitch size of the nozzles resulted in varying the density of nozzles on the membrane, and it was observed that an extensive array of nozzles resulted in enhanced density distribution. This study has shown that both VMA devices are not only affected by the fluid properties but also perform differently due to their design and dimensions, despite the same working principle and dynamics. The ability to easily customize sizes and

nozzle dimensions using micro-fabrication techniques offers unique advantages compared to metallic VMA.

Fluid with dynamic viscosity below 3cPs was easily atomized, and above 3cPs did not atomize, suggesting that either viscosity reduction of the liquid or applying additional pressure or energy is required to atomize viscous fluids. Therefore, micro-fabrication of the electrical microheater and assembly with the micro-fabricated device are the following steps for the device to be capable of new applications.

## **CHAPTER 4**

### **FINITE ELEMENT MODELLING AND MICROFABRICATION OF THE MICROHEATER**

MEMS based microheater have received great attention in last few years not only for the researchers but also for the industries due to their extensive applications in pressure sensor, gas sensors, flow rate sensors, micro ignition of micro propulsion systems etc.[66-70]. A microheater is a resistive heater with resistive filament ranging from 100nm to 100um made with MEMS fabrication techniques. Filaments are generally made of metal layer characterized as low power consumption, fast response, mechanical stability, and yield. MEMS microheater have become an increasingly vital in portable devices that operates on low voltage and power. Furthermore, the triggering rapid temperature changes of the localized thermal area of micromachined devices has opened up new perspectives for development of field sensors [71]. Microheaters have been used in both 2D and 3D printing systems such as inkjet printing[72] and thermal printing[73] and heat sintering. One of the promising additive manufacturing technologies is thermal inkjet which uses microheater to create pressure pulse to eject the droplets by vaporizing the ink material. High operating temperature of the microheater increases the capability of vaporizing high viscous ink with 40cPs viscosity value [74, 75]. And increasing operating temperature of the device offer multiple benefits such as high jet frequency, wide choice of materials. Extensive research has been done on microfabrication, materials, failure modes and other performance parameters. Gas sensors use microheater as an important component to heat up the sensitive layer at specific temperature to promote the reaction between targeted gas and sensing layer. Metal oxide-based gas sensors are widely

used in automotive and industrial applications [76]. Different layer resistive temperature detector membrane has been studied to improve the performance of the sensor including response time, stability, and sensitivity [77, 78].

MEMS microheater works on the principle of Joule's heating. Joule heating is the phenomena in which the heat is generated from the conductive material when electric current is passed through the conductor. The power consumed is directly proportional to the resistance of the conductor and square of the current passed. The device has an advantage of localized heating and optimized energy consumption. Resistive heater is used in various applications that requires localized heating and temperature control at micro scale such as gas sensing device [79], moisture controlling [80] and local growth of nanostructures [81]. The traditional approach of photolithography is employed to pattern the conductive layer and removing certain parts to form required shape of the film. Additive manufacturing is also a promising way to fabricate the micro heaters as this eliminates the complexities of microfabrication process.

#### **4.1 Microheater Design**

A microheater is a sophisticated MEMS device and it involved multiple physics, materials, and geometry designs. Basic design of a microheater consist of three components: (1) conductive pad, (2) resistive heating element, and (3) substrate. If source voltage is connected across the heater, results in current through the circuit.

The heat produced by the heating circuit is dissipated in the surrounding air. The thermal losses are through conduction, convection, and radiation but the maximum operating temperature for the device in our study is 100-150°C therefore, the radiation losses can be neglected. During operation, the fluid near the surface of the heater is superheated by the current and becomes less viscous.

Microheater with different heating circuit design such as meander, driving wheel, double meander and S-shape are shown in figure 4.1 is made for this study to get the best design for controlled temperature profile on the surface and low power consumption. The width of the heating circuit ranges from 230-250  $\mu\text{m}$  and the conductive bond pads are 1\*1 mm. The substrate selected is to be circular in shape with diameter of 7mm.

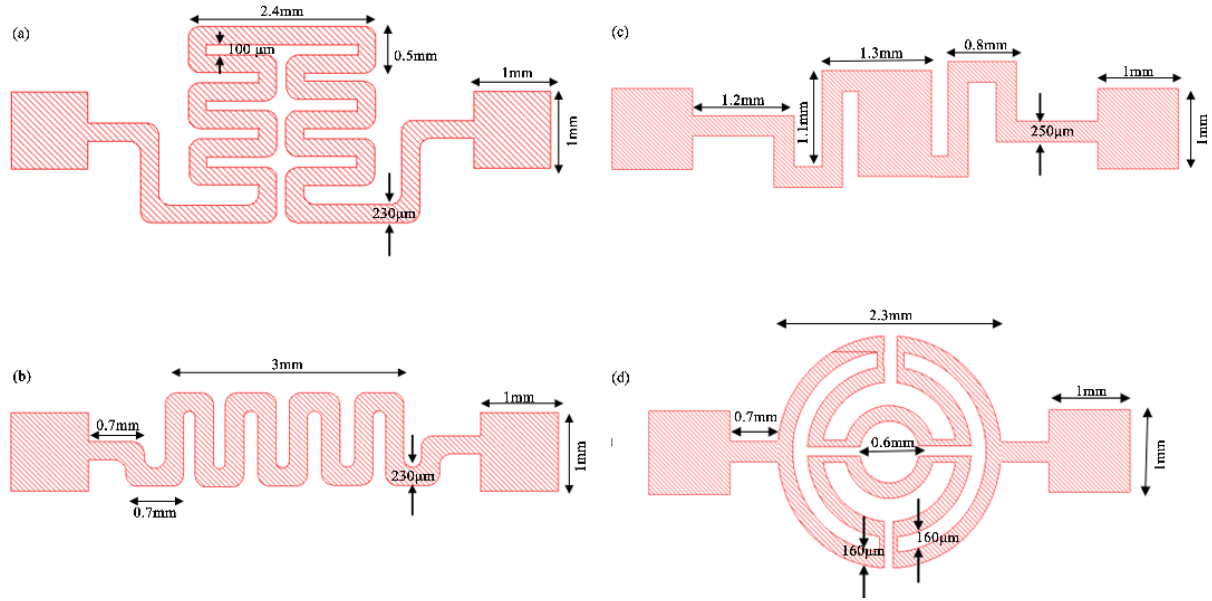


Figure 4.1 – Schematic of adapted microheater design: (a) Meander, (b) Double meander, (c) Driving wheel, (d) S- shape.

## 4.2 Microheater Materials

The substrate is the foundation for the microheater, and many materials have been researched by researchers for substrate and heating circuit. Typical substrate material widely used are silicon, glass [82], stainless steel, and ceramics [83, 84]. High temperature range can be easily handled by silicon and ceramics than glass and steel. Ceramics typically have high thermal conductivity resulting in high power consumption. Usually, MEMS fabrication is carried out on silicon wafer which requires a lot of etching work which makes it time consuming and costly. Polymer membranes have gained a lot of attention recently due to its robustness, low

thermal conductivity, and simple fabrication steps [85]. The thermal coefficient of expansion of polyimide is quite similar to silicon, makes it compatible for IC fabrication process.

The conducting layer is the main source of heat. Most researched materials include platinum (Pt)[44, 76, 85-88], gold[89], titanium[90], tungsten, and molybdenum[91]. Maximum operating temperatures of platinum and titanium are between 600-700°C. Tungsten also has high operating temperature range of 1200°C but it is only stable in oxygen rich environment till 400°C. Molybdenum also suffers oxidation issues at temperature of 300°C[92]. Platinum is commonly used as a heater or electrodes because of its high sheet resistance and less reaction with oxygen and harsh gases[93, 94].

In our study, polyimide membrane is chosen as flexible substrate due to its good mechanical and thermal properties to achieve high temperature uniformity and short thermal response time. The heat will quickly be transferred to the periphery and whole surface through conduction and to the fluid in contact through convection. Also, layer thickness is easily controlled in comparison to another layer. A platinum resistor and bond pads are utilized to release Joule heat and supply current due to its stability at high temperatures.

### **4.3 Numerical simulation using COMSOL**

The heat transfer module is used by product designers, developers, and scientists to investigate the effects of heating and cooling in devices and processes using accurate geometrical representations. The Heat Transfer Module aids in the analysis of the impacts of heating and cooling in devices, components, and processes. The module provides us with simulation tools to investigate heat transmission processes such as conduction, convection, and radiation, which are frequently studied in conjunction with other sciences such as structural mechanics, fluid dynamics, electromagnetics, and chemical reactions. The Heat Transmission Module serves as

a platform for all sectors and applications where the formation, consumption, or transfer of heat or energy is the focus of or significantly contributes to the process being examined. The device consists of electrically resistive layer which heats up due to Joule's heating when a voltage is supplied to the circuit. For a successful design of the device some important design considerations are uniform heating, minimum deflection of the device and avoidance of overheating of fluid. Avoiding overheating the fluid reduces the risk of self-ignition of the fluid. The Multiphysics uses electric current module with heat transfer module.

### 4.3.1 Heat Transfer Governing Equations

This section describes about the governing equations used to predict the electrical and thermal response of a microheater.

#### 1. Current Conservation

Joule heating is produced by running current through the resistive material. The constitutive relation is described by Ohm's law:

$$J = \sigma E \quad (1)$$

J is the current density and E is electric field strength

The electrical conductivity,  $\sigma$  of the microheater is given by :

$$\sigma = \frac{1}{\rho_0(1+\alpha(T-T_0))} \quad (2)$$

Where  $\rho_0$  is the resistivity at reference temperature,  $T_0$  and  $\alpha$  is the coefficient of resistivity.

Based on conservation of charge and continuity equation, electric potential through the heater can be described by:

$$-\nabla_t \cdot d(\sigma \nabla_t V) = 0 \quad (3)$$

d is the layer thickness, V is electric potential applied and  $\nabla_t$  is the gradient operator. Resistive heating is produced from the resistivity in the circuit. The heat produced, Q can be given by:

$$Q = \sigma |\nabla_t V|^2 \quad (4)$$

## 2. Heat Transfer

In microheaters, heat produced by Joule heating is transferred away by conduction and convection for low temperature as radiation mode can be ignored. The first law of thermodynamics can be reduced down to the governing equation given by:

$$\rho C_p \left( \frac{\partial T}{\partial t} \right) - \nabla(k\nabla T) - h\nabla T = Q \quad (5)$$

Where  $\rho$  is the density,  $C_p$  is specific heat,  $k$  is thermal conductivity,  $h$  is convection coefficient,  $\nabla T$  is change in temperature and heat source,  $Q$ .

## 3. Structural Mechanics

When microheaters are heated, change in temperature result in thermal expansion of material inducing stress. The governing equation is given by:

$$\rho \left( \frac{\partial^2 u}{\partial t^2} \right) = \nabla s + F_v \quad (6)$$

$s$  is the stress tensor, material displacement is represented as  $u$  and  $F_v$  is the volume force vector.

At steady state, the metal layer dissipates the heat generated in two ways: on the side of the fluid and other to the substrate through conduction. In order to evaluate heat transfer from the heater, material properties and parameters of substrate, heater are listed in table 4.1.

Table 4.1 – Material properties used in the simulations.

Property	Platinum	Polyimide
Thickness	100 [nm]	10 [ $\mu\text{m}$ ]
Density	21450 [ $\text{kg}/\text{m}^3$ ]	1300 [ $\text{kg}/\text{m}^3$ ]
Thermal conductivity	71.6 [ $\text{W}/\text{m}^*\text{K}$ ]	0.15 [ $\text{W}/\text{m}^*\text{K}$ ]

Coefficient of thermal expansion	8.80e-6 [1/K]	5e-5 [1/K]
Young's modulus	168e9 [Pa]	3.1e9[Pa]
Poisson's ratio	0.38	0.34

### 4.3.2 Simulation Model

A 3D model with microheater is modelled for simulations. For simulations, model developed has platinum microheater on silicon substrate shown in figure 4. In the model, Pt resistor layer is centrally located on the substrate. The convective heat loss is applied to all other side walls as they are exposed to air so, convective coefficient is set as 5W/m\*K. Top surface is exposed to working fluid so, convective coefficient is set as 200W/m\*K.

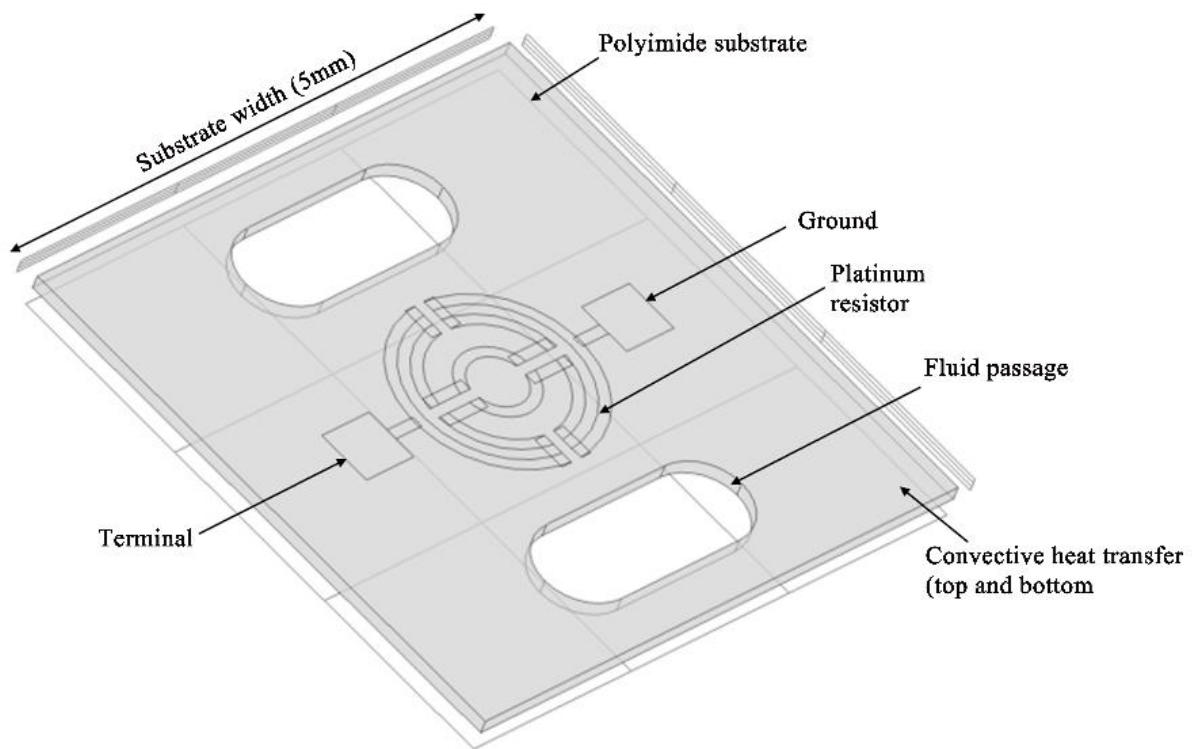


Figure 4.2 – 3D simulation model of microheater.

### 4.3.3 Physics and Boundary conditions

Both stationary and time dependent study was performed. The joule heating is stimulated as result of application of voltage,  $V$  on one heater pad as terminal and the other one is ground. In time dependent study, continuous voltage is supplied. A convective heat flux with ambient air ( $20\text{ }^{\circ}\text{C}$ ) was the primary source of heat loss on the external surface of the sample and heater assembly. Top side of the microheater had a convective heat flux of  $100\text{W/m}^2\text{*K}$  and all the other sides had heat flux of  $5\text{W/m}^2\text{*K}$ . Temperature-dependent resistance changes were not predicted since no resistance changes were detected in experiments while heating to relevant temperatures.

The Joule heating is simulated as a result of input voltage applied at the bond pads. Natural convective heat transfer was assumed for all sides of the substrate i.e., air at  $27^{\circ}\text{C}$  except the top surface which is exposed to working fluid. Heat dissipated from the microheater surface is greater than heat dissipated from the vertical walls of the substrate. Hence, heat dissipation from other sides i.e., lateral sides can be neglected considering thermally insulated boundaries. The contact resistance between electrode pads and connected circuit is regarded insignificant in electric current physics. Radiation effects were eliminated from the final model since they were considered to be minor since the maximum temperature is less than 300 degrees Celsius. Building the right mesh for the research is a critical step before performing the simulations. Mesh may be built manually in COMSOL by selecting various portions with varying maximum element sizes, or it can be created automatically by the software for the full geometry. Meshing is done manually in this study since it contains two pieces, a substrate with a larger thickness than the microheater, which is  $100\text{nm}$ . The entire substrate was meshed with 3-D tetrahedral components that split the domain, each element having a minimum size of  $100\mu\text{m}$ , for meshing.

The microheater has a thickness of 100nm, for this reason chose a different mesh strategy. Free triangular mesh with maximum element size of 10 $\mu$ m is chosen. The surface of a microheater with a thickness of 100nm was meshed with 2-D triangular components swept along the thickness.

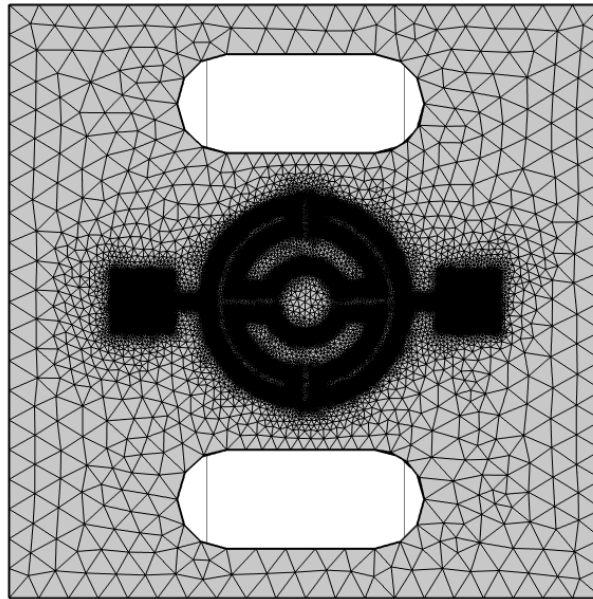


Figure 4.3 –Meshing configuration of microheater.

#### 4.3.4 Study Configuration

Once the mesh is defined, stationary study with a parametric sweep of the voltage to the microheater is chosen. Parametric sweep is a function that gives a possibility to analyses the problem varying a specific parameter in a specific range. We chose to vary voltage and thickness of heater layer with the fluid heat flux value kept constant to know the behavior of microheater and temperature that could be achieved and the power associated with it. The final and most essential option is "Solver Configuration," which allows the user to select the solver type prior to calculation. There are two primary types, each with its own set of characteristics:

- Solvers that solve problems directly - Direct
- Solve iteratively - Iterative

MUMPS, PARDISO, and SPOOLES solvers are the direct solvers utilized by COMSOL. These solvers generally arrive to a certain solution for all well-conditioned finite element problems, which is their main benefit, and they can even solve certain problems that aren't well-conditioned. It makes no difference which of the direct solvers we use in terms of the solution because they all provide the same result. The main distinction between the direct solutions is their speed. All these solvers are capable of taking advantage of all processor cores on a single setup, however PARDISO is the fastest and SPOOLES is the slowest. Although all of the direct solvers demand a large amount of RAM, MUMPS and PARDISO may store the answer out-of-core, allowing them to transfer portion of the issue to the hard drive. The MUMPS solver likewise enables cluster computing, which allows us to employ more memory than would normally be accessible on a single system.

Iterative solvers get at the answer in little steps rather than in one big leap. As a result, while using this approach to solve the issue, the estimated error in the answer lowers as the number of iterations grows. If we're working on problems that aren't as sound, convergence will be delayed. The oscillatory behavior of an iterative solution is usually a hint that the problem isn't properly set up, such as when the problem isn't constrained enough.

## **4.4 Simulation results**

The objective of the simulation is to estimate the temperature distribution and power required to reach certain temperature. We performed simulations on four different shapes of microheaters to determine the temperature distribution on the top and bottom membrane surface. Thermal profiles along X-axis (horizontal) are always better to investigate the temperature distribution as they give a better understanding of temperature uniformity on the surface.

### **4.4.1 Temperature distributions**

In figure 4.4, thermal maps of top surface and bottom surface of driving wheel shape of resistor is presented to give the better understanding of temperature distribution on the entire surface with color gradient at 1V. With application of different voltage, we start from a temperature of 20°C and could reach to 1000°C. The maximum temperature on the surface depends on the length, area, resistance of the resistor and current supply to the circuit. The temperature profile required for our application is to be maximum at the center of the membrane and remaining part to be at room temperature and these simulations helps to estimate the results.

Figure 4.5 shows the temperature distribution for all types of heater designs. To exhibit temperature variations, a line graph is plotted for temperature over the membrane's surface from one end to the other. These line plots show that the temperature is stable and maximum in the region of resistors and minimum at the place with no circuit. The temperature varies 3-4C at the different width of the circuit, but the average temperature of the surface remains constant. The topside and bottom sides of the membrane are examined, and it is determined that the average temperature on both sides of the membrane is same and does not fluctuate.

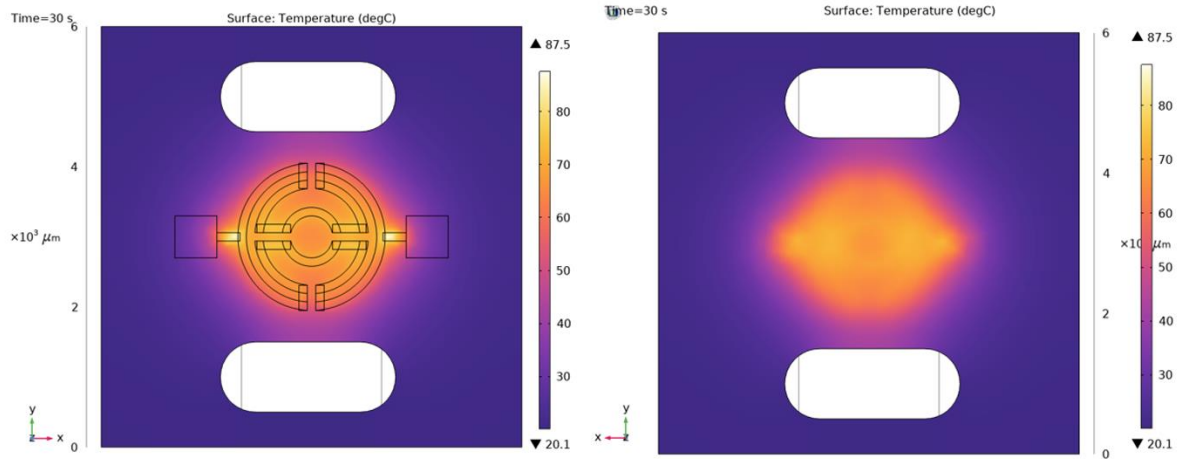


Figure 4.4 – Thermal maps of top and bottom of D-wheel microheater at 1V.

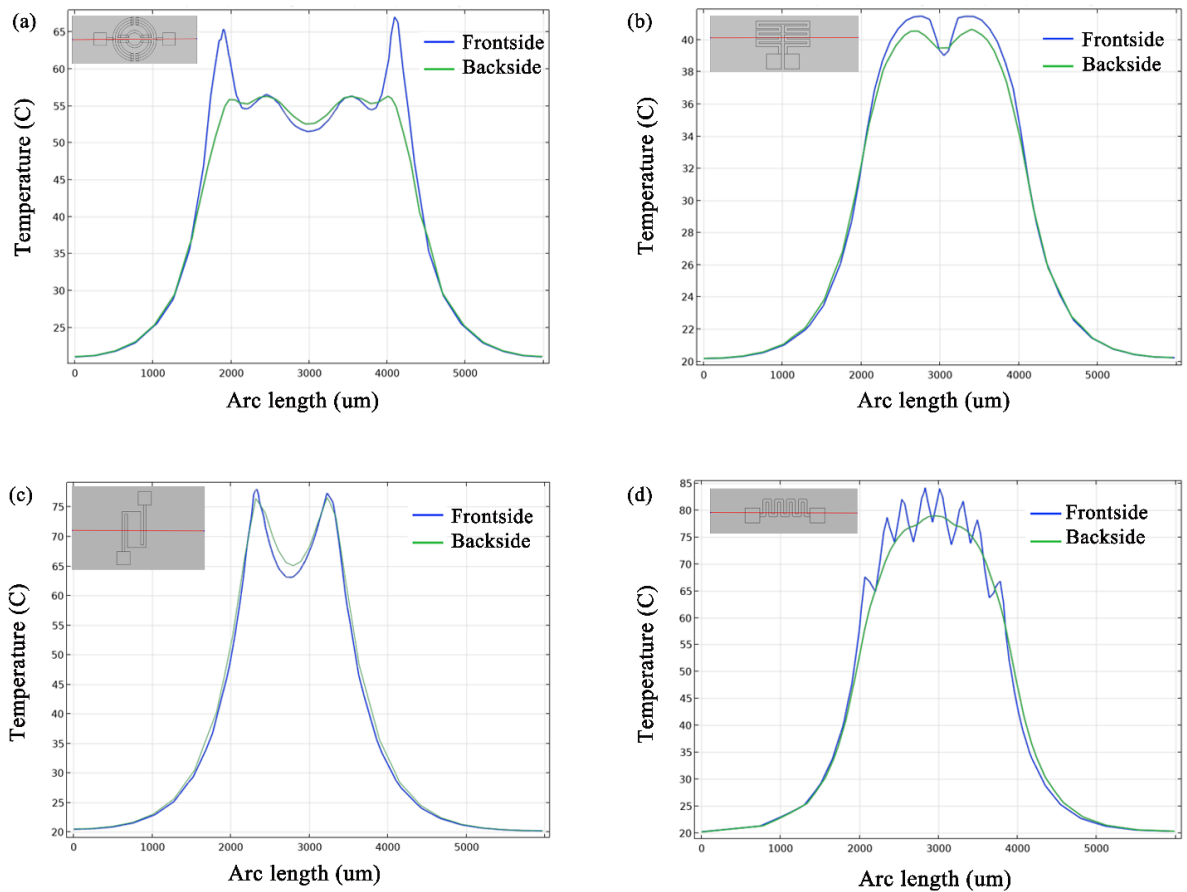


Figure 4.5 – Thermal maps of top and bottom surface of microheater substrate along X direction for (a) double meander, (b) driving wheel, (c) meander and (d) S-shape for applied voltage of 1V.

Detachment is one of the principal causes of device failure in general heating circuits or resistors on top of any substrate, which is generally induced by interfacial tensions. Once it starts to detach, localized warming speeds up the process, potentially leading to circuit overheating and burning. As a result, it's critical to consider interfacial stresses when examining the device's functioning, which might vary depending on the kind of resistor layer, its thermal coefficient of expansion, and the heater's design. The greatest interfacial stresses found very little at the circuit's corners are 6.5MPa for all of our designs as seen in figure 4.6(a). Polyimide (substrate) yield strength is 40 MPa, while platinum yield strength is 70 MPa. This suggests that the maximum interfacial stress is far lower than the substrate and resistor's yield strength, implying that the individual component stays structurally intact under the simulated power input loads.

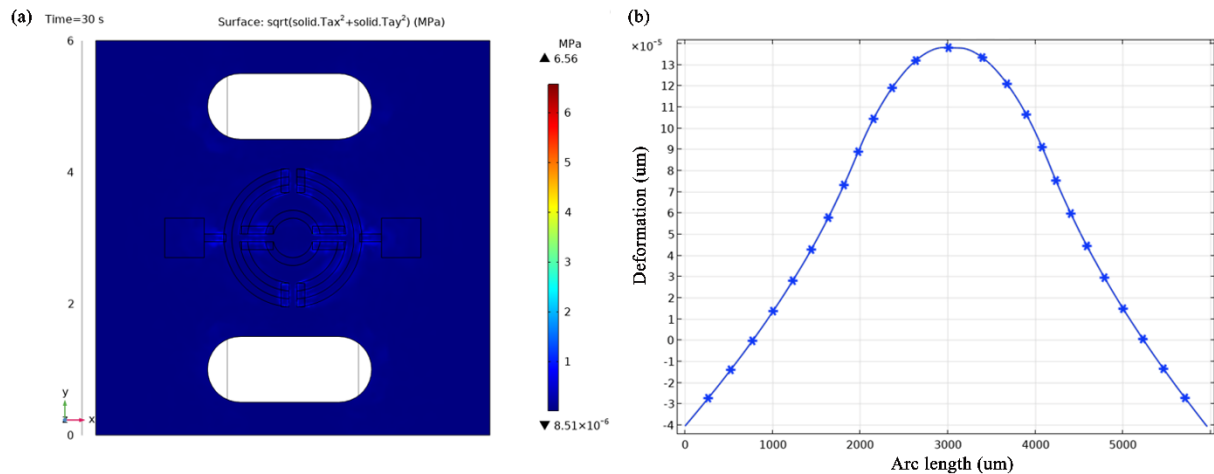


Figure 4.6 – (a) The thermally induced von Mises stresses, (b) Deformation of the planar surface on the fluid side of the membrane.

The temperature rise induces thermal stresses on the device due to material different thermal expansion coefficients. This gives rise to mechanical stresses and deformation in the layer of the resistor and substrate. After getting heated, the membrane tends to bend towards the air

side. Figure 4.6(b) shows the resulting deformation in the membrane for driving wheel design. The magnitude of the deformation is in range of  $10^{-5}$   $\mu\text{m}$  at the center of the membrane. For our application, this value is not significant that could affect the device working performance.

#### 4.4.2 Heater Height Simulations

Figure 4.7 represents the effect of  $\mu\text{H}$  layer thickness on the temperature profile at varying applied voltage. Thickness is varied from 100nm to 1000nm at the step of 200nm and it is expected that the maximum temperature of the surface will increase at high value of thickness with varying voltage. It has been observed that a high voltage supply and a thicker resistor result in the highest temperature. The resistance value is inversely proportional to the area of the resistor, which relies on the thickness, hence temperature rises as the resistor thickness increases. When the thickness of the circuit is increased, the resistance across the circuit decreases, allowing more current to flow through it and, as a result, the temperature curve grows linearly.

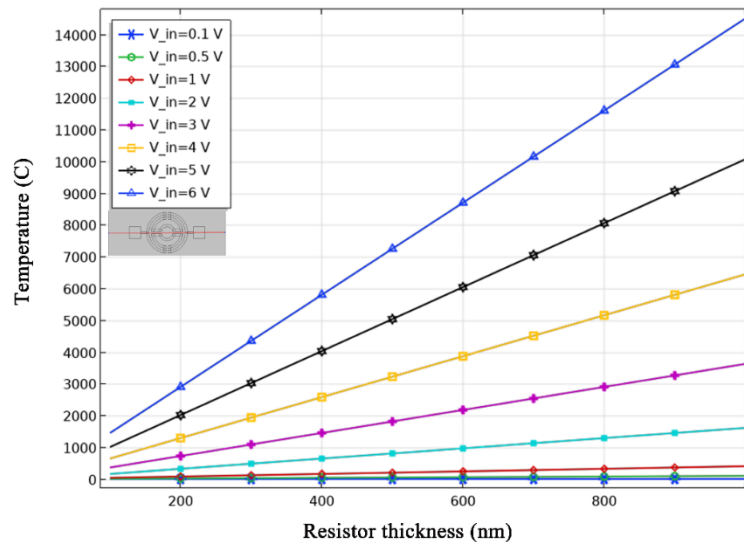


Figure 4.7 – Temperature variation for different microheater thickness at varying applied voltage for D-wheel resistor.

### 4.4.3 Heat transfer coefficient Simulation

Heat transfer coefficient value depends on the heat carrying capacity of the fluid and effect of heat transfer coefficient is shown in figure 4.8 for 100nm thick platinum metal and all types of microheater at constant applied voltage of 1V. The high heat transfer coefficient suggests that the liquid may absorb more energy from the heated circuit in the form of heat. As a result, when a fluid with a high  $h$  is used, the surface temperature is lowest. The reason for this is that energy is delivered to the liquid more often and continuously, resulting in a lower surface temperature than a liquid with a lower heat transfer coefficient. This trend is true for all types of resistors designs however the temperature value depends on the resistance of the circuit.

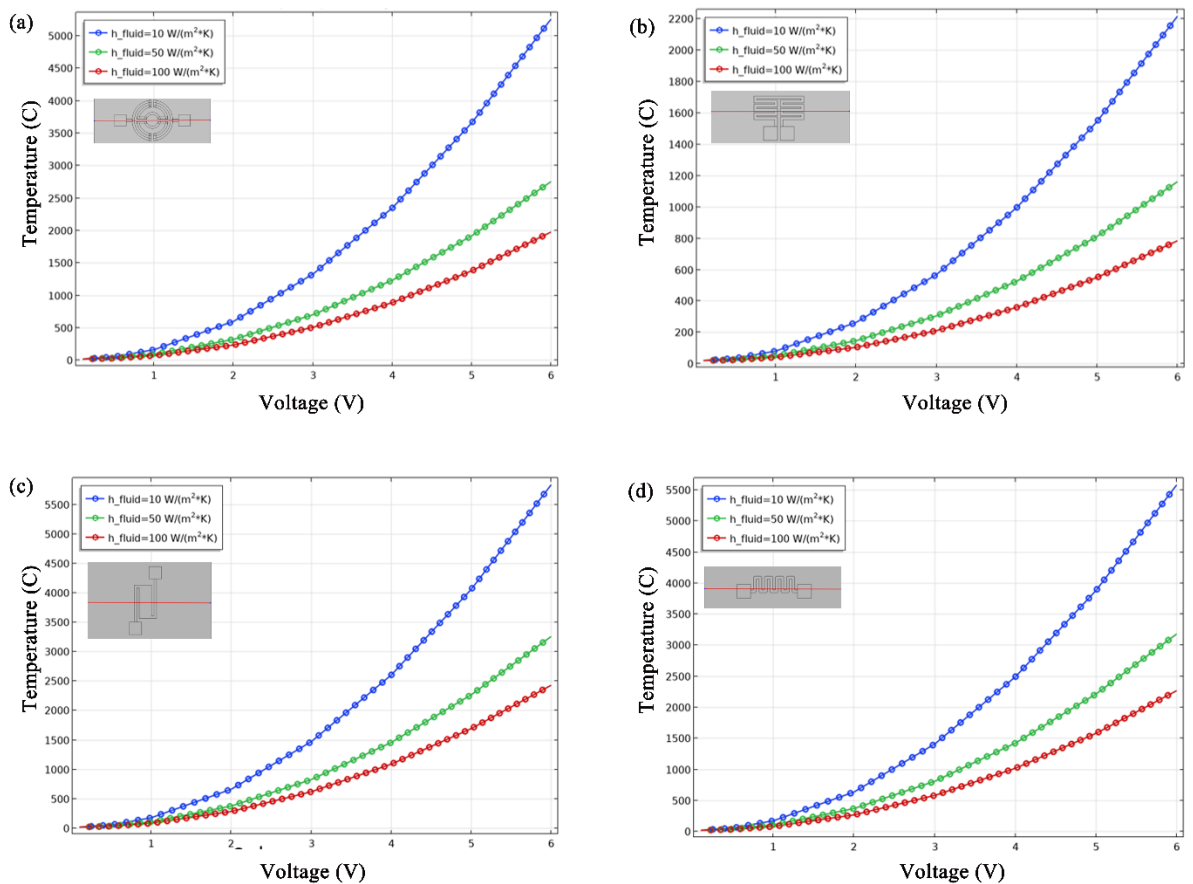


Figure 4.8 – Effect of heat transfer coefficient on surface temperature.

## 4.5 Fabrication Method

In this study, the microheater's substrate must be light weighted, thus a polymer-based membrane is preferable, and it must have superior mechanical and thermal characteristics in order to achieve high temperature uniformity and quick time response. Polyimide is thus chosen for microfabrication, and its compatibility with semiconductor processes makes it simple to deal with. Platinum is used as electrodes and resistors due to high sheet resistance and less reaction with oxygen.

The fabrication of microheater involves use of semiconductor processes like patterning, etching and deposition. Photolithography is the basic process that involves transferring the pattern from mask on to the substrate and is an important step used in production of any device. This process has several sub-steps starting from coating the substrate with vapor HMDS (Hexamethyldisilane) to make the substrate hydrophobic followed by spin coating of photoresist (photo sensitive solvent-based solution used to transfer the pattern), soft bake step to bake the resist to get rid of the solvents present and harden the photo sensitive organics involved. Then, the resist is exposed exposing it to UV light at certain intensity and time to supply the dose to clear. During this step, for positive type of resist the part exposed to UV rays (with the wavelength range of 300-400nm) gets soft and become soluble in developer during developing step. Once, the wafer is developed, it is rinsed with Deionized water five times and then spin rinse dried and inspected. All the tools including spin coater, hot plate, Karl Suss MA06 exposure tool, caustic bench (for developer) and SRD (spin, rinse, and drier) used for carrying out the steps towards photolithography process is shown in figure 4.9.

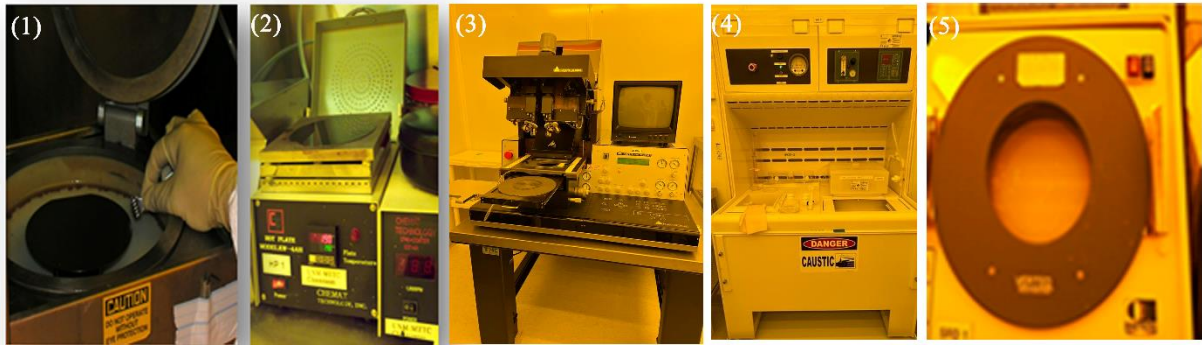


Figure 4.9 – Steps and tools for photolithography process.

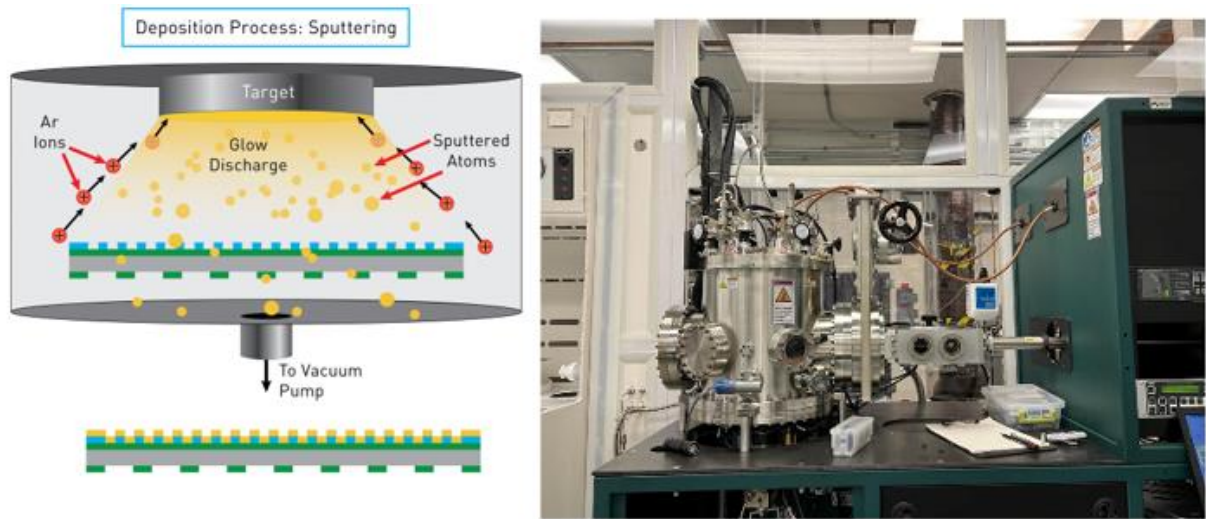


Figure 4.10 – Schematic of sputter tool working and AJA sputter machine.

The next semiconductor process employed for the fabrication of microheaters is deposition and etching. Physical vapor deposition method is the method in which solid material is vaporized under vacuum environment with the supply of power and gas flow to deposit on a substrate as thin film. AJA sputter tool is used here for metal deposition (i.e., platinum and aluminum). This system consists of target also known as cathode, which is the material to be deposited and substrate i.e., anode on which the material needs to be deposited. The working principle is as when Argon gas is supplied under vacuum and high voltage is supplied between target (cathode) and substrate (anode), the electrons present in the sputtering gas are accelerated away from target resulting into collisions to nearby atoms of gas causing

ionization. The positive atoms move towards the cathode leading to high energy collision with the target surface making the target material atom to be ejected with high kinetic energy to reach the substrate surface under vacuum environment. The schematic and the setup used is shown in figure 4.10. After deposition, another important process involved is etching. Reactive ion etching with March plasma etcher shown in figure 4.11 is the one used here. In the system, plasma is created by application of strong radio frequency electromagnetic field, typically of 13.56 MHz to the wafer holder. The etching gases are ionized by oscillating electric field creating strong plasma. The ions drift towards the wafer colliding the samples to be etched by application of high voltage. This is also called dry etching or anisotropic usually used for directional etching where the profile created after etching is in one direction. It is usually used to etch resist, silicon dioxide, silicon nitride etc. however in current work, this etching method is used to etch polymer thin film



Figure 4.11 March plasma Etcher (Reactive ion etching).

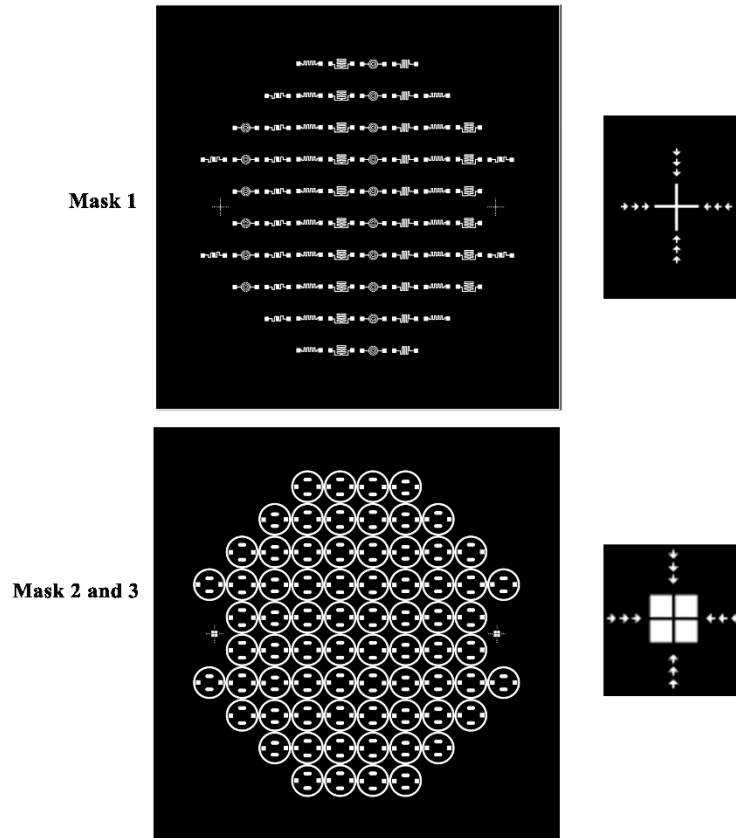


Figure 4.12 – Photomask layout for microheater devices and etch profiles with alignment masks.

The photomask is the either opaque quartz or glass plate with open areas or transparencies that allows UV light to pass through the defined pattern to transfer the design on to the substrate through lithography process. In current work, transparencies were used created by Fineline Imaging company. Figure 4.12 shows the photomask pattern used for fabrication of devices. The first mask i.e., mask 1 is the metal or resistor layer mask that is used with lift off process to create the heater pattern. The mask 2 and 3 are used twice, once to pattern the polyimide and other time to create pattern for hard mask for etching step.

The fabrication process of microheater involves photolithography and different deposition and etching process as shown in figure 4.13. The process starts with the spin coating of polyimide

(PI-2611) on silicon at the speed of 1000rpm for 45 seconds and cured at temperature starting from 50°C with ramp of 5°C/min until 350°C and kept for 60 minutes and slowly ramped down the temperature to room temperature. Then the photolithography is performed with lift off resist (nLOF2070) is spin coated at 3000rpm and soft baked at 110°C for 120 seconds. The resist film is exposed to UV light with intensity of 365nm from the mask and then developed. Platinum metal with 100nm thickness is deposited by sputtering at 300W power, 3mTorr pressure and 13sccm argon gas flow. The extra metal is removed by soaking the wafer in acetone by lift off process and the metal heater remains. The metal is needed to insulate to avoid any direct contact or chemical reaction with the fluids in contact. To insulate the metal heater the photo definable polyimide (HD4100) layer is spin coated at 2000rpm, soft baked at 90°C and 120°C for 3 minutes each and then cured at 375°C for 60 minutes with ramp rate of 5°C/min starting at 150°C using hot plate to obtain the thickness of 8µm. Next, the polyimide layer is patterned to create the openings for circular streets for detaching individual devices, electrodes, and fluid passage cavities and developed using puddle process with developer PA-401D for 60 seconds and blow dried with nitrogen. Then, the lift off resist was spin coated and patterned, developed and metal deposition and lift off process was performed to have aluminum metal hard mask (areas except fluid cavities, streets, and electrodes). The passage holes and the peripheral streets are etched with the Reactive ion etching method using CF<sub>4</sub> and O<sub>2</sub> gas flows. Once etched, aluminum hard mask is removed using aluminum wet etchant and the microheater devices are easily separated from the silicon substrate.

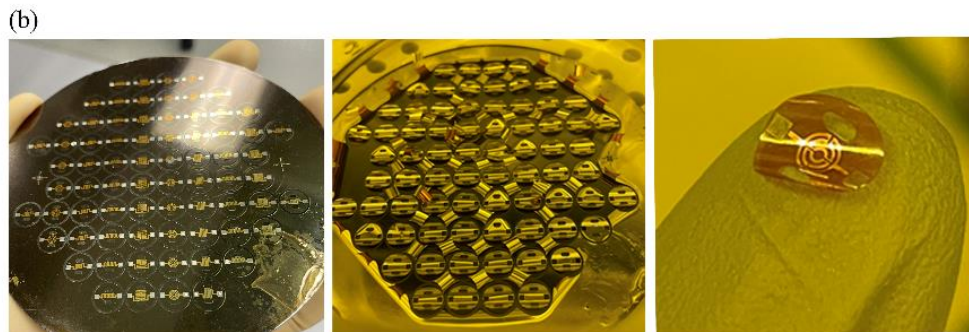
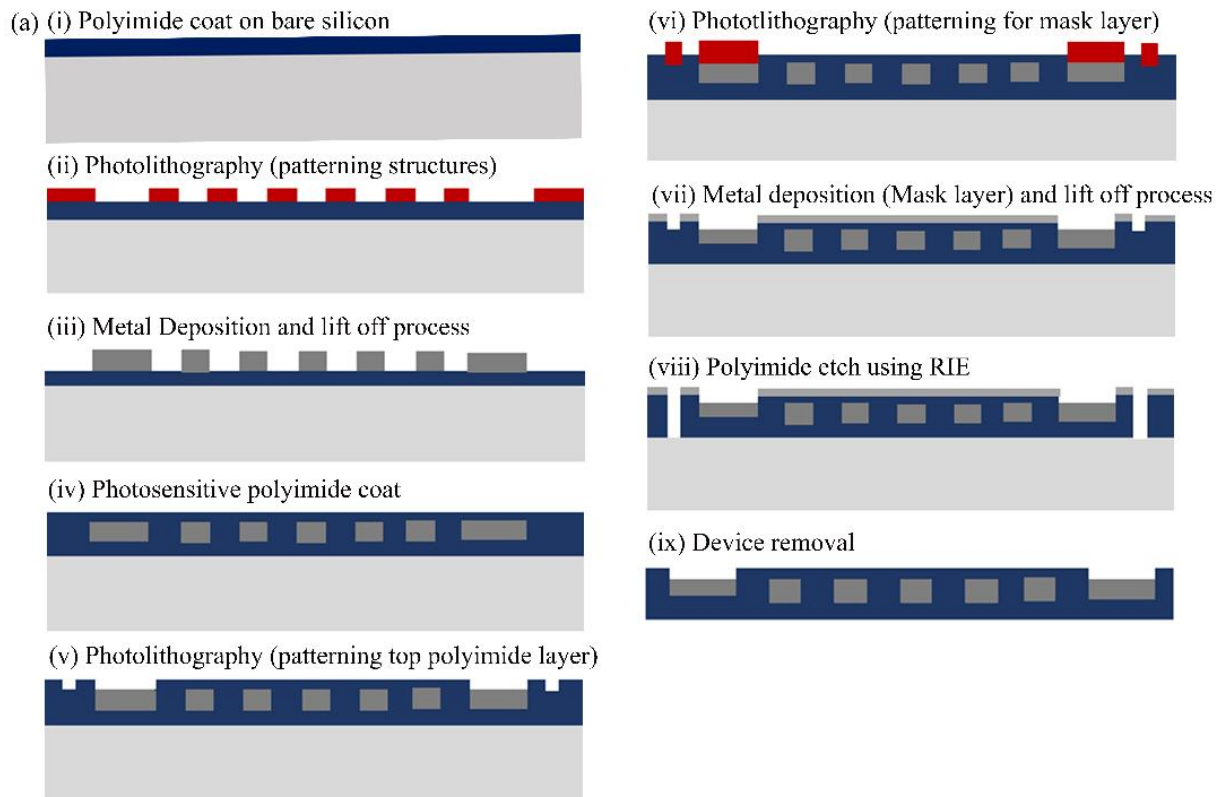


Figure 4.13. (a) Microfabrication steps polymer based microheater, (b) Device images during fabrication steps (after second polyimide layer, during aluminum etch, individual device).

## 4.6 Characterization

The heating characteristics of microheater will be measured with a thermal imaging camera. The uniformity of the heating characteristics of the microheater will be evaluated by measuring the average temperature and the size of the area >90% of the maximum temperature. Individual microheaters were tested with a multimeter (Fluke 6.5-digit precision bench digital multimeter)

to assess initial resistance and then retested before each usage. To assess the initial and long-term heating of the microheaters, an infrared (IR) thermal imaging camera (PI 640i Microscope optics) with a DC power source (0-30V, 0-5A Programmable DC Bench Power Supply) was utilized. These instruments were used to determine the temperature distribution and time response.

Resistive heating is the conversion of electrical energy in the form of current into heat as it runs through a resistive substance. The microheater device was well fabricated without any cracks in the substrate and insulation polyimide layer and the metal layer was defect free with no breaks in the circuits. The resistance is 39 Ohms for double meander shape, 22 Ohms for single meander, 20 Ohms for driving wheel and 13.78 Ohms for S microheater design. The double meander has highest resistance due to high value of path length in comparison to other and hence will require more power to reach the same temperatures as other designs. The series of measurements were performed to determine the relation between power consumption and voltage and surface temperature using water as working medium. We used driving wheel design and varied the voltage to obtain the current, I and surface temperature which was monitored with IR camera. The I-V characteristics of the heater is shown in figure 4.14. The power consumed is calculated as follows:

$$P = I^2 * R = V * I \quad (7)$$

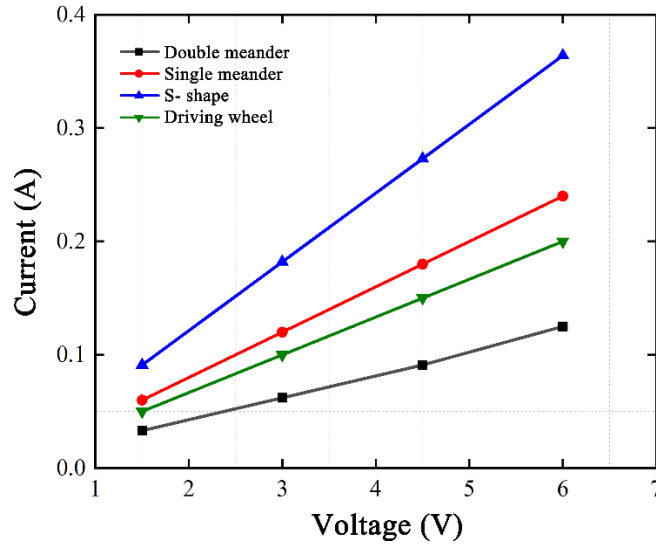


Figure 4.14. I-V characteristics for four microheater designs.

The infrared heating profiles for varied power input were measured in relation to overall microheater performance of the four microheater designs employed in further application-based studies, as shown in Figure 4.15. It displays the IR photos of a 1V input, demonstrating an equal heating profile along the heater with no hotspots, indicating that a liquid in contact with this microheater would be heated evenly. The maximum average temperature of the rectangular region (outlined in black in IR images) has an average temperature of 50°C for double meander, 79°C for meander, 78°C for driving wheel and 94°C for S shape of microheater design at 1V input. Higher power settings may be necessary for the liquid to attain the same temperature as reported in IR thermal analysis due to heat dissipation via the polyimide thin layer with thermal conductivity (0.12 W/(m\*K)) and heat transfer into various viscosity liquids. These microheaters have a short reaction time, reaching the ultimate temperature in less than 3 seconds, indicating that the liquid will not take longer to heat. As long as power is supplied, the profile retains its ultimate temperature. During IR heating

testing, no resistance drift was detected, as evidenced by no change in current draw from the initial contact with the power source during heating. Therefore, both temperature and power levels can be easily managed since these resistors have no resistance drift. Furthermore, the results show that for a given range of voltage inputs, the low resistance microheater (S shape) produces a wide range of temperatures when compared to the high resistance microheater (double meander). To conquer out any inconsistencies in initial heating, the low resistance microheater was heated for 10 minutes for ten trials and time temperature curves were produced, with no significant differences between heating trials. The microheater was able to attain the average temperature repeatedly within the first few seconds of power input and maintain it with a steady power source. This demonstrates that the microheaters are very constant and reusable, with no resistance shift as a result of frequent heating.

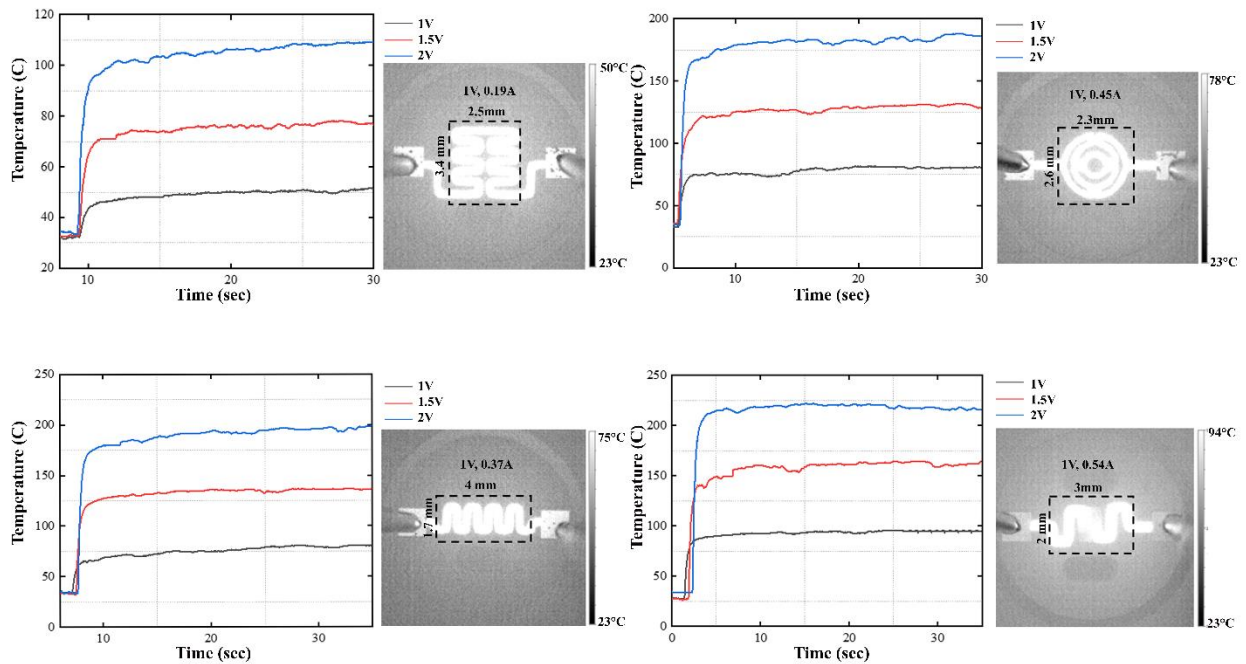


Figure 4.15. Microheater performance for different designs.

The simulated model shows how microheater designs can create a wide range of temperatures in liquid medium. The fluid is heated at the top of the microheater, then is meant to travel through the cavity being on the other side of the membrane, where a similar heating effect at the same temperature maintains the viscosity of the liquid and participate in the atomization process. At 1V supply, the surface temperature of the driving wheel design spans from 20°C at the edge or periphery of the membrane to average temperature of 84°C around the resistor design and at the center of the membrane where the liquid is placed. Similarly, for other designs, same trend is observed in terms of temperature distribution profile.

In addition to the stationary study, time dependent analysis was performed to determine the time response of microheater. Continuous voltage was applied for 30 seconds at 1 second intervals, and the highest temperature obtained in the transient investigation reveals identical results for simulated and experimental studies as shown in figure 4.16.

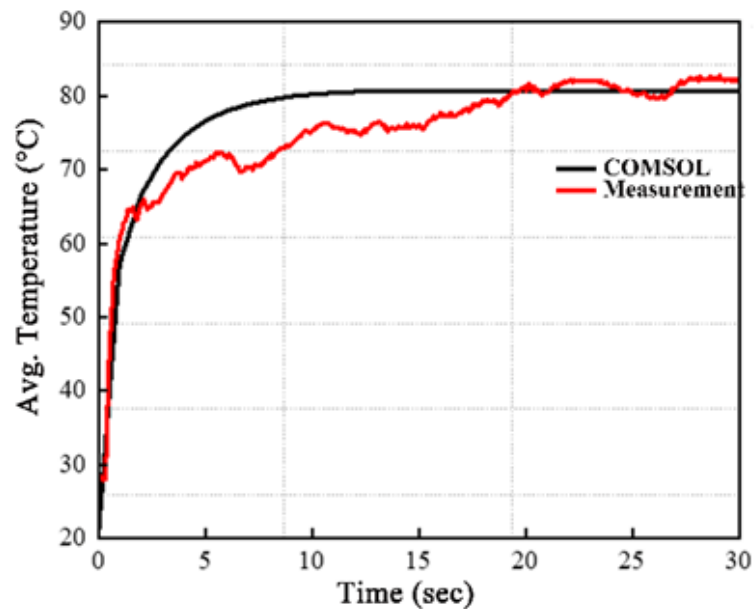


Figure 4.16. With Driving wheel design, Comparison of FEM, and measurement temperature-time results for the microheater at 1V supply.

The modelling was a valuable tool that helped in determining the temperature profile and response time of the real devices and the COMSOL results, and the measurements obtained were in good agreement of each other.

#### **4.7 Summary**

The heat transfer FEM results suggest that all four resistor designs on a polyimide substrate can provide the required heating temperature with variable input voltage. The temperature profile requirement of heating at the center portion of the membrane can be achieved with either of the circuit designs. Simulations with platinum metal circuits and variations in metal thickness demonstrated that a thickness of 100 nm of platinum is sufficient to provide heat energy to the vital parts of the membrane. Different applications employ liquids with other properties and heat dissipation capacity, so maximum surface temperature also depends on the heat transfer coefficient of the fluid. The microheater is fabricated using the appropriate process parameters and micro-fabrication processes involving patterning structures, metal deposition, and etching procedures. A sturdy and stable device is fabricated and characterized based on surface temperature and response time to heat the surface and liquid in contact.

## **CHAPTER 5**

### **INTEGRATION OF VIBRATING MESH ATOMIZER AND MICROHEATER**

The microfabrication and performance analysis of the atomizer and microheater were dealt with separately in the previous chapters. While working independently in their own ways, the two stand-alone devices yielded promising results. However, the goal of this project is to create a monolithic device that can work with a variety of liquids for a variety of applications, and in order to accomplish this, it's critical that the two devices work well together as an integrated system. This chapter covers the creation of an integrated device, as well as its testing and analysis for liquids with various physiochemical properties.

#### **5.1. Integrated device and working concept**

The integrated device operates on the principle of heating the viscous liquid with the microheater device to lower viscosity while atomizing at the same time. The microheater membrane has two fluid passage cavities that allow fluid to move from the top surface of the membrane to the rear side after heating and thinning. The two devices are separated by a spacer, which serves as a fluid chamber for the atomizer device when its viscosity decreases as shown in figure 5.2. To facilitate atomization by capillary action, the fluid chamber is quite small (thickness in range of microns). After the fluid reaches the backside of the microheater membrane, the atomizer activates and increases the pressure in the liquid in contact with the mesh, pushing it through the apertures during the positive half cycle of actuation and pinching off the liquid at the device's outlet during the reverse cycle of actuation.

To complete the microfabrication of the device, a separate spacer is required to be fabricated with SU-8 is to be placed at the periphery of the atomizer. The SU-8 spacer is fabricated using

photolithography process which involves spin coating, soft baking, exposure and developing the photosensitive resist. SU-8 is a negative type of resist in which the part exposed to UV rays gets hardened and stays during developing process. For spacer thickness of more than 300 $\mu\text{m}$ , the SU-8 2150 was used and spun at 1500rpm for 60 seconds, soft bake for 7minutes at 65C and then 120minutes at 95C. This spin speed will result into thickness of 400-425 $\mu\text{m}$ , so exposure energy required is 500mJ/cm<sup>2</sup>. Negative resist requires post exposure bake step after exposure to carry out the cross-linking process between the polymers which were exposed to UV rays thus, making it hard and rest of portion (unexposed to UV) dissolving during developing process step. So, the post exposure bake was carried at 65C for 5 minutes followed by 25minutes of baking at 95C. The last step of lithography involves developing using SU-8 developed (solvent based) for 30 minutes or until SU-8 clears followed by spin, rinse, dry and inspect. The photomask layout is shown in figure 5.1 which is designed with the alignment marks to align with heater masks in case the alterations are made in fabrication process in future.

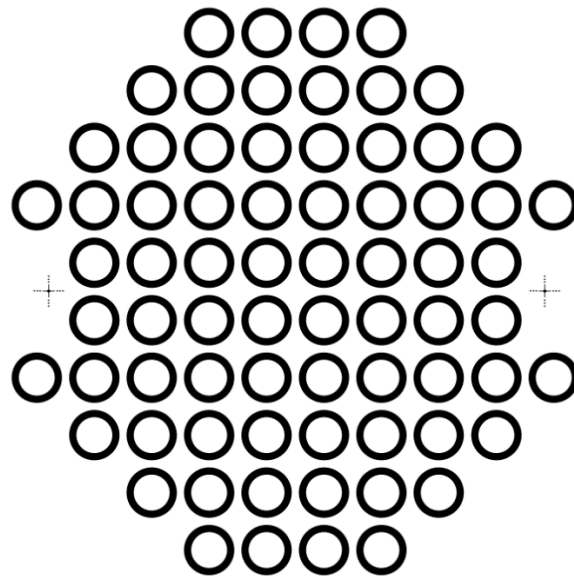


Figure 5.1 Photomask layout for spacer rings.

This spacer could also be 3D printed with regular filament, and 3D printing makes it simple to change the dimensions at any time. As shown in the diagram below, the spacer acts as a separator between the atomizer and the microheater. The vibrating mesh device is put together using conductive epoxy in the traditional way. Manually plucking the microheater-designed polyimide layer off the substrate wafer, bringing it into contact with the spacer, and bonding it with epoxy adhesive. Because the polyimide layer is quite thin, after bonding to the spacer, a small weight is placed on top of it to ensure that the thin film sits perfectly on top until it is completely dried. Now that the microheater device is perfectly balanced on top of the spacer, the spacer is made to fit between the MEMS atomizer and the PZT using epoxy. The empty space between PZT ring and atomizer is used well in this integration process without hampering the individual working of the atomizer device. The spacer does not add any extra mass on the base washer holder to alter any frequency working range.

Following the bonding of the various components including stainless-steel washer holder, silicon-based membrane with apertures, piezoceramic ring, spacer ring, and polymer based microheater, the thin silicon membrane beneath the microheater is ensured to be intact and to work very well when tested with DI water. The circuit wires of 5-10cm length are attached on the top surface of PZT which has thin aluminum layer working as top electrode and washer holder bottom surface as bottom electrode bonded using conductive epoxy. The 3D model created in Solid Works depicts the entire integrated device, and the cross-sectional view depicts the atomizer's deformation mode while in contact with the liquid.

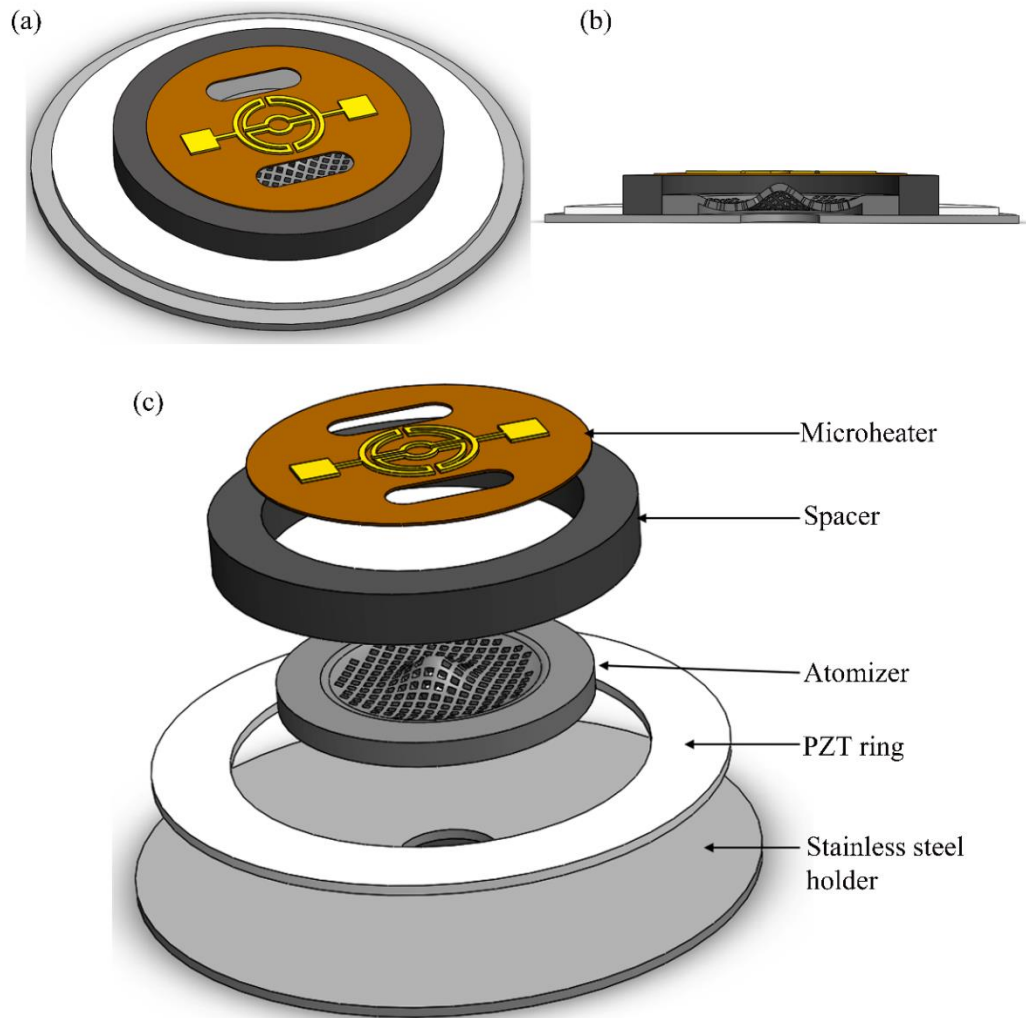


Figure 5.2. (a) Isometric view, (b) Cross-sectional view, (c) Exploded view of 3D model of microheater integrated device.

## 5.2. Experimental setup

The characterization of the device involves its testing and performance study in terms of working ability with different liquids. In this study, different glycerol concentration solution is considered for testing. The temperature or power required is another aspect to be determined for various concentration solution. IR thermal camera is used to determine the temperature distribution and time response. The atomizer operates at a frequency of 99kHz, which is powered by a waveform generator with a high frequency amplifier. The droplet size

distribution of different glycerol concentration solution using integrated device is determined using a laser particle analyzer (Sympatec HELOS KF) based on the laser diffraction principle and measuring sizes ranging from  $0.9\mu\text{m}$  to  $175\mu\text{m}$  by analyzing the scattered laser light intensity. The photographic analysis was performed using the photos recorded by the D3500 Nikon NIKKOR 18-55mm lens with the backdrop was darkened to maintain the image's contrast. The viscosity measurements of the liquids were measured using calibrated Cannon-Fenske viscosity tube (P4520-6 for 20-80cSt and P4500-5 for range of 7-28cSt and P4500-2 for 0.8-3.2cSt).

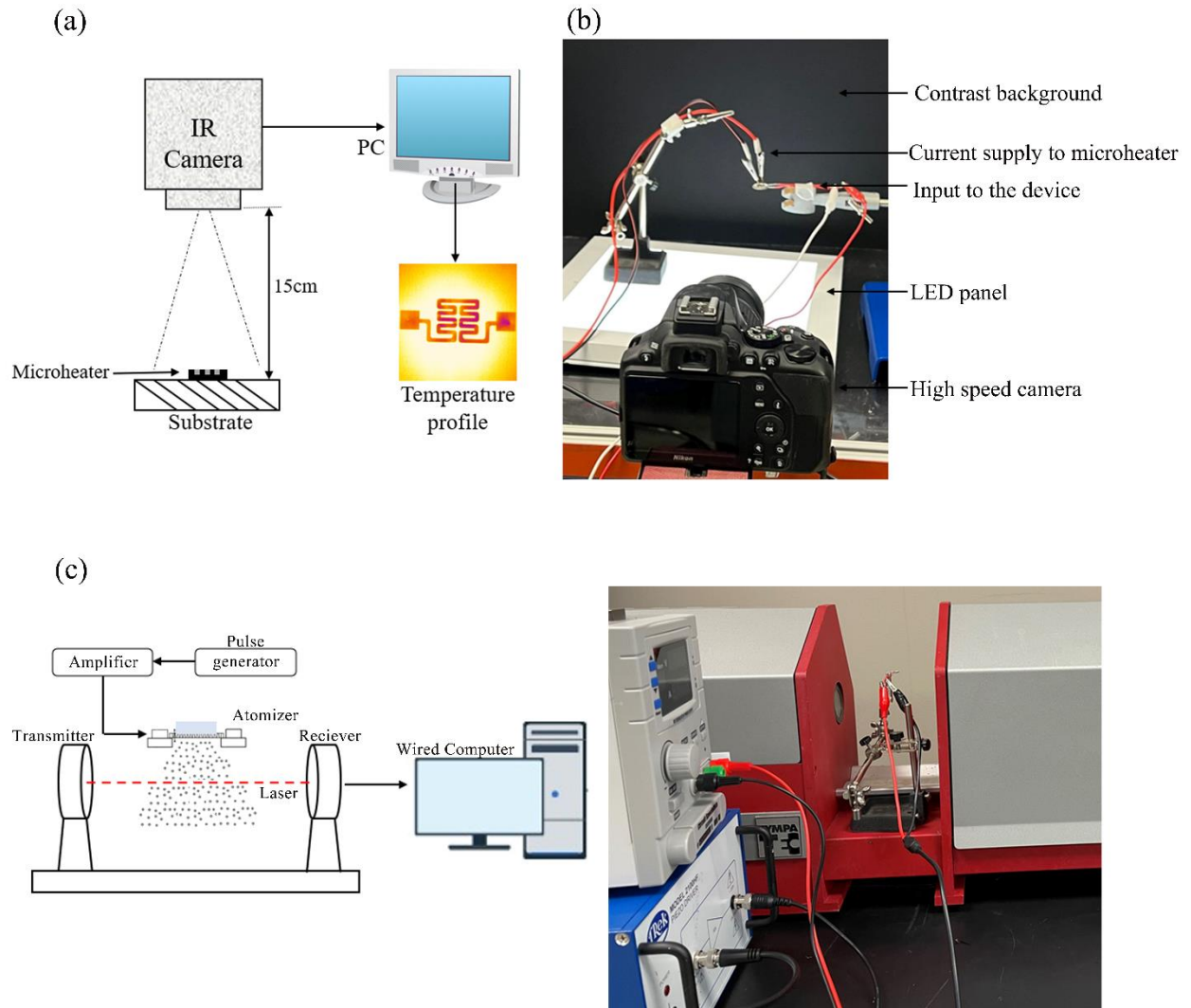


Figure 5.3. Tool used for characterization (a) Infrared camera setup, (b) Photographic setup and (c) Sympatec laser setup.

### 5.3 Results and Discussion

The density, surface tension, and viscosity values of the liquids tested are mentioned in table 5.1. These fluid qualities have a substantial impact on droplet formation, and it is feasible to aggregate these properties to establish a dimensionless number,  $Z$ , which is an inverse of Ohnesorge number ( $Oh$ ), that defines the mechanics of droplet formation given by:

$$Z = \frac{\sqrt{d\rho\gamma}}{\eta}$$

Where  $d$  is a characteristic length usually nozzle outlet radius,  $\rho$  is the density of the fluid,  $\gamma$  is the surface tension and  $\eta$  is the viscosity. The range of  $4 < Z < 14$  is considered as optimal for stable droplet formation[95]. The greater value relates to noncontrolled droplet creation in the form of satellites, which are tiny droplets detached from the primary drop. Lower values equate to viscous force dominance and drop ejection difficulties owing to fluid viscous dissipation. The values of fluid properties are measured at room temperature and calculated for a characteristic length of  $5 \mu\text{m}$  (nozzle radius). As,  $Z$  decreases (i.e.,  $\eta$  increases), the drop ejection is expected to be more difficult and after a certain value, impossible. The transition between distinct operating zones, marked by satellites, ideal droplets and viscous dissipation is slow and not only determined by  $Z$  but also depends on geometry and the design of the nozzle and the entire system. According to  $Z = 9.6$  for 20% glycerol, the MEMS device is predicted to form ideal droplets, which is justified because the device produces aerosol under typical operating conditions. However, at greater concentrations, such as 30 and 40, the  $Z$  value falls within the desirable range of 4 to 14, but the device does not achieve atomization or perfect drops indicating the viscous force dominates even if the  $Z$  falls in the optimal range mentioned

in literature. At concentrations at and above 50%, the Z value is less than 4, indicating viscous dissipation, and the device is ineffective in forming droplets without applying additional pressure. Increased input voltage can be used to provide extra pressure, but this will result in high displacement and velocity, as well as a high risk of the membrane failing at the center. As a result, heating the liquid reduces the density and viscosity of the liquid, causing the value of Z to fall into the range of 4-14 for those that fall outside of this range.

Table 5.1. Properties of the liquids used for tests.

Glycerol%	Density, kg/m <sup>3</sup>	Surface tension, mN/m	Viscosity, cP	Z
20	1047	71.7	1.9	9.6
30	1070	71	3	6.5
40	1100	70	4.1	4.9
50	1128	69.3	7.45	2.4
60	1156	68.5	13.9	1.6
70	1190	68	29.8	0.7
80	1210	67	50	0.4

The integrated device was made out of a standalone VMA device and a microheater separated by an 3D printed spacer ring bonded by epoxy. The device was then tested with various glycerol concentration solutions from 30% to 70% with variable density and viscosity at room temperature. The completed device ran at the same frequency as the separate atomizer devices, which was 99kHz. Since additional velocity of the membrane was required to break the surface

tension of the viscous liquid in contact, the voltage peak to peak amplitude used to drive the assembly was raised from 50Vpp to 100Vpp.

For experimental series, a small droplet was placed on top of microheater membrane just enough to cover the microheater portion so, that when device turned on the viscosity reduces and expands and flows towards the cavity and transfers to the other side of the membrane (top of atomizer) and then it atomizes. For driving wheel design, the temperature required to atomize a 30% glycerol concentration with a viscosity of 3cP is 34°C and 0.034W power, while a maximum concentration of 70% with a viscosity of 29.8cP requires 105±5°C and 0.369W, as shown in figure 5.4. The temperature requirement remains the same for the same viscous liquid with different microheater designs, but the power changes due to resistance variations. Higher concentration requires more power to reduce the viscosity and atomize. For all the concentration, the power consumed to atomize was less than 1W. During the whole process, the surface tension and viscosity of the liquid decreases with increasing temperature. The microheater's immediate increase in temperature causes it to have low viscosity, which means that less energy is viscously dissipated, and fluid goes to the opposite side, where it is pushed out by the atomizer. The heater achieves a constant temperature after a few seconds of turning on the power, and the heating and atomization processes take around five seconds. The height of the spacer ring was designed to keep the gap between the bottom of the microheater membrane and the top of the atomizer as narrow as possible, allowing capillary action to create tiny sheet-like quantities of liquid. The atomization procedure did not work at concentrations more than 70% through the atomizer. The liquid began to evaporate as a result of the vaporization process caused by heating events.

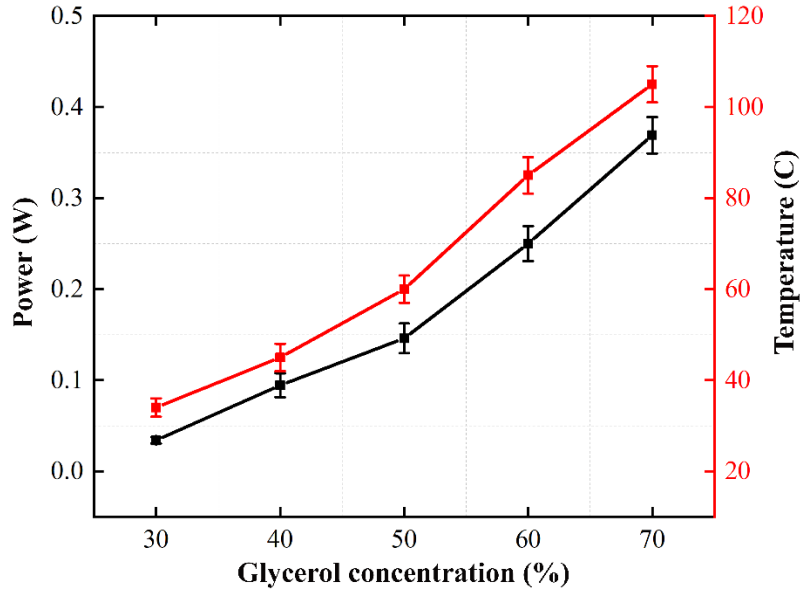


Figure 5.4. Power and temperature profile for different glycerol concentrations with driving wheel microheater design.

Figure 5.5 shows the photographic analysis of the atomization process for different liquids at various times. The process was monitored from  $T=0$  sec till it was atomized completely. The shots were selected at different times,  $T=5, 10, 15$  seconds. The atomization process barely started after first few seconds of heating, so formation of vapor was noticed at  $T=5$  seconds and propagation of the droplet formation was observed at  $T=10$  and  $15$  seconds. For the low % glycerol, i.e., 30, 40 and 50 the atomization after 15 seconds was in full flow and as seen in the image that the entire membrane was forming the droplet efficiently whereas for higher % glycerol i.e., 60 and 70 the flow was observed at some section of the membrane demonstrating that the atomization process was supported at the middle portion of the device since the device operates at (0,2) mode and the movement of the membrane shows that it has maximum displacement and velocity at the center of the membrane. The remaining section of the membrane needs more displacement to create enough force to break the surface tension of the liquid in contact in order to obtain the same flow density as low concentration. The thinning

of the liquid along with capillary effect and highest amplitude of displacement contributed towards atomizing dense liquid. This also affected the spray angle which was determined by post processing the images. The spray angle with 30% is  $17.94^\circ$  and as the concentration gradually increased to 70%, the spray angle reduced to  $10.42^\circ$ . These results are supported by the literature as liquid viscosity decreases the spray cone angle [96] and the nozzle require more pressure or liquid flow rate to increase the spray cone angle[97]. In this integrated device, the way to increase spray angle is to increase the velocity of the membrane which depends on input voltage and operating frequency of the device.

Figure 5.6 shows the droplet distribution of various percent concentrations with a 10m nozzle exit size. The volume median diameter (VMD), which represents the size of 50% of the entire population of droplets, is used as a criterion for comparing findings. For 30% glycerol, the aerosols contained droplets of  $4.63\mu\text{m}$  (X10) to  $17.17\mu\text{m}$  (X90) and VMD of  $10.22\mu\text{m}$  which is almost equal to the nozzle outlet size with the span (width of the distribution) of 1.34 and as the concentration of glycerol increased to 70%, the range of droplet size is  $2.84\mu\text{m}$  (X10) to  $23.55\mu\text{m}$  (X90) and VMD increased to  $13.46\mu\text{m}$  and the span increased to 1.6. When the viscosity is low (up to 30% glycerol), the VMD is unaffected; however, when the viscosity is raised with a higher percentage of glycerol, the VMD increases. When viscosity is low, surface tension is dominant and dependency on viscosity is minimal in the atomization process and when viscosity is high, surface tension weakens, and viscosity becomes the dominating factor[1].

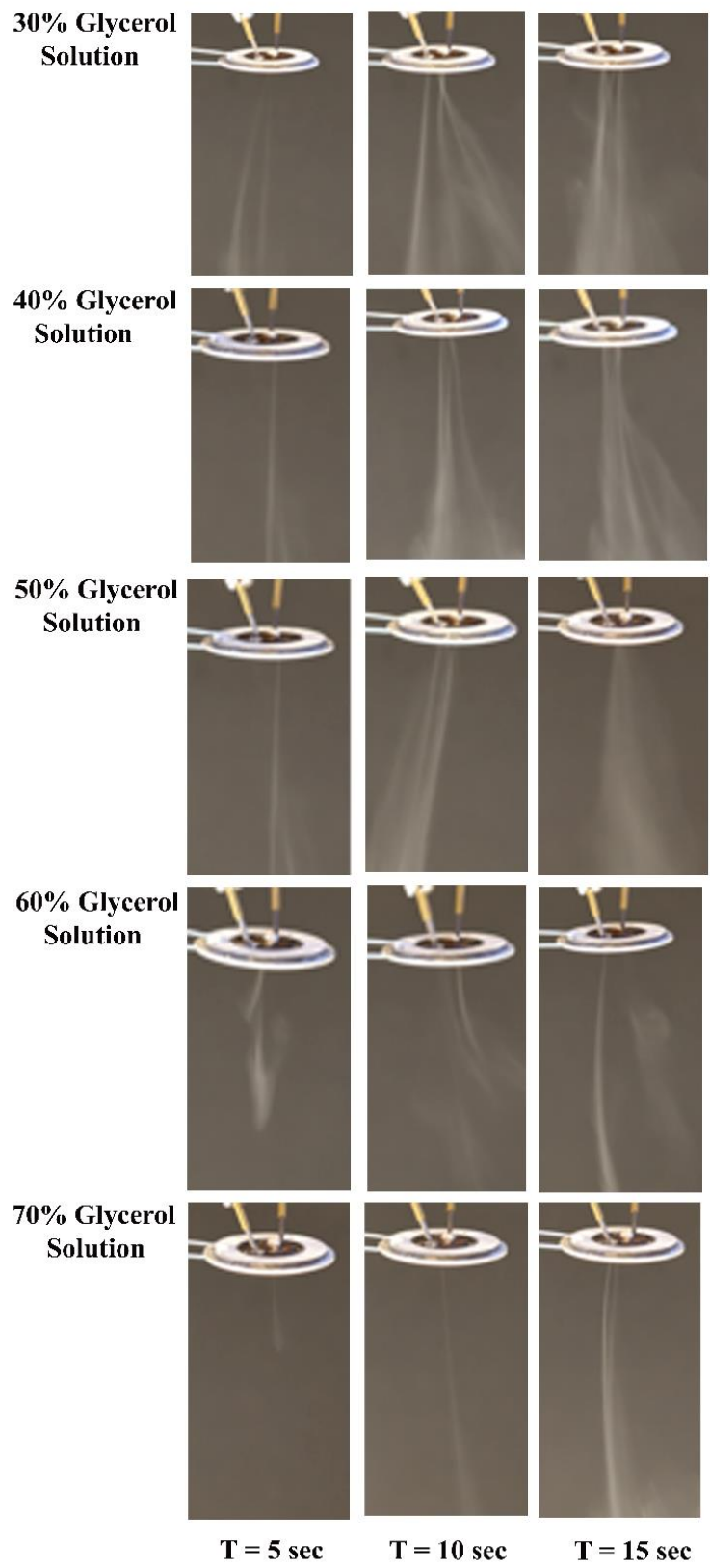


Figure 5.5. Photographic images of spray formation with integrated device at different times.

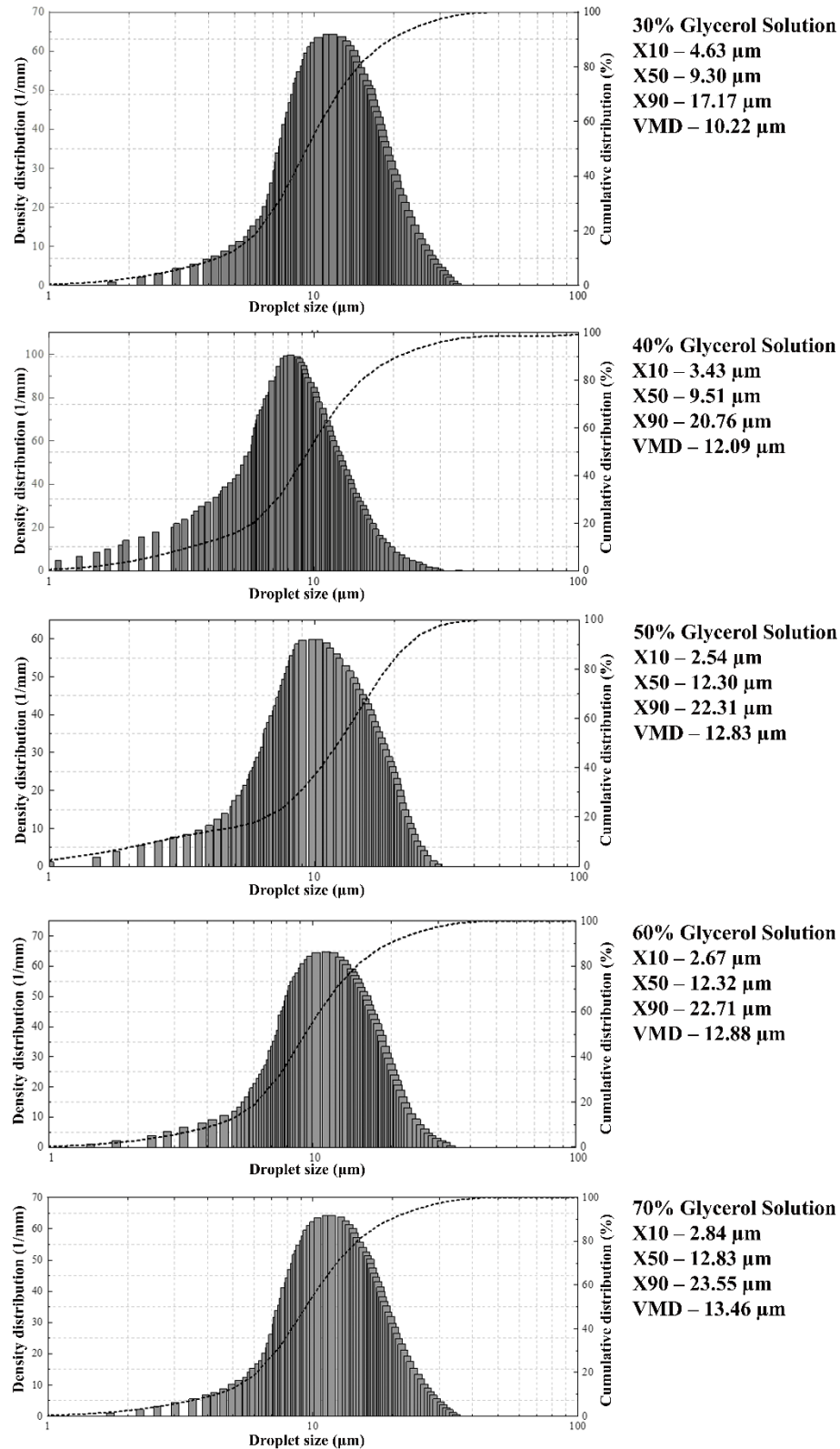


Figure 5.6. Droplet size distribution for different glycerol concentrations with the new device. The comparison of spray angle and VMD of droplets produced for different concentrations is shown in figure 5.7. The spray angle tends to decrease and VMD increases as the glycerol concentration goes up due to the density and viscosity and the resistance of the fluid flow leads to these results.

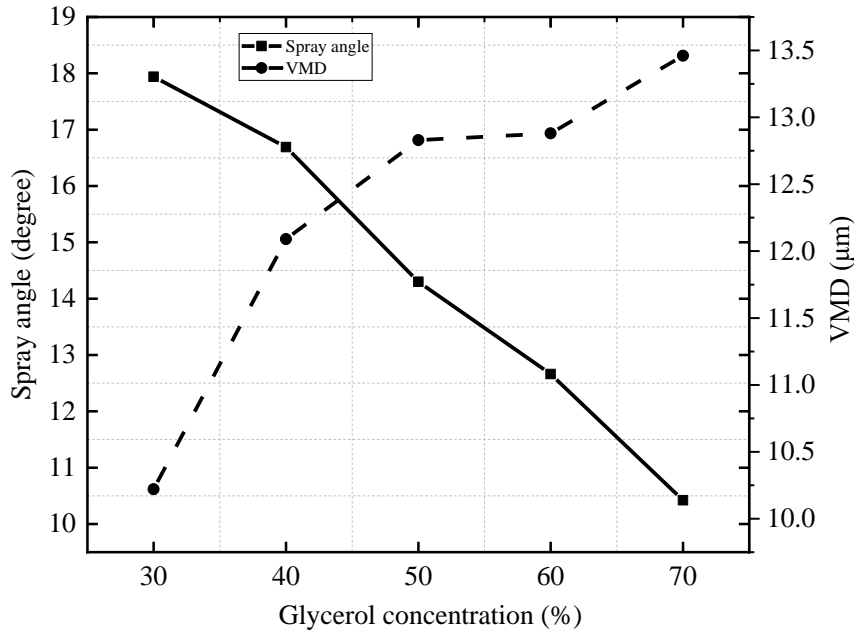


Figure 5.7 – Spray angle and VMD comparison for glycerol concentration solution.

## 5.4 Summary

This study presents the modified MEMS vibrating mesh atomizer consisting of a microheater, an atomizer, and a spacer, which supplies thermal energy to reduce the working liquid's viscosity and maintain the capillary action in the gap between two integrated devices working independently. Different experiments were conducted to study microheater design, power consumption, temperature profile, droplet size distribution, and spray angle of the ejected droplets. The proposed microheater design consumes less power, making it a low-power device (<1W) with a range of temperatures depending on the application's requirements. The images

were post-processed to identify the spray angle and help view the atomization process. Finally, the built device was demonstrated to work with a wide variety of liquid viscosities up to 28cP, which is nine times larger than the independent device's threshold of 3cPs. The modification of the MEMS-based atomizer opens the door to new applications in various industries.

## CHAPTER 6

### APPLICATION OF MEMS VIBRATING MESH TECHNOLOGY

The flexibility of a gadget, or the range of its uses, affects its industrial usefulness. The conventional atomizer device is widely used in a variety of applications and has been studied for many years; however, the MEMS-based vibrating mesh atomizer device is new to the market with only one application (i.e., inhalation therapy), so the purpose of this study is to identify an application where this device could benefit from its key advantages, as well as identify areas that need to be improved and conduct new problem-solving research. In this chapter, the results of an experimental inquiry into the usage of vibrating mesh atomizer in new areas are discussed, and the output obtained is compared to what was expected or to the outcomes of traditional procedures. Experiments with MEMS VMA have been undertaken in two areas: creating SiO<sub>2</sub> and resist thin films using spin-spray deposition with the manufactured device, and spray cooling the heated substrate with the same device and comparing it to the commercial device. The next sections cover in further detail the details of the two investigations.

#### **6.1 Vibrating Mesh Atomizer for Spin Spray Deposition of SOG and SU-8**

This section describes the use of a silicon-based MEMS vibrating mesh atomizer for the spin-spray deposition technique. This study examines spin spray deposition of SOG and photoresist as a substitute for spin coating techniques for conformal coating of high aspect ratio 3D objects [98]. Spin coating is the most common method for creating homogeneous thin coatings of liquid-based materials, such as photosensitive materials, with thicknesses ranging from micrometers to nanometers. It's commonly employed in the production of a broad range of

integrated circuits and microsystems [99]. Centrifugal force drives the liquid outward radially and surface tension and viscous force tends to cause the formation of thin residual film on a flat surface [100]. Spin coating produces a homogeneous coating but has a number of drawbacks, including high quantities of wasted material since almost all of the liquid is spun off the wafer, making it unsuitable for costly liquids. Furthermore, spin coating is effective at coating flat surfaces but fails to conformally cover 3D topographical surfaces [101]. Spin coating may form a thin layer of any liquid-based substance and is often used in microfabrication to install photosensitive compounds such as photoresist. Other specialty liquids, on the other hand, are extensively utilized for certain purposes.

Spin on Glass (SOG) or spin on dopants (SOD) are extensively used in microfabrication as a dielectric material, sacrificial layer, structural layer, mask layer, and is commonly used as a carrier of dopants for SOD technology. It is a material that serves as a planarization agent and as an insulating layer [102]. There are various types of SOG such as Silicate SOG, siloxane SOG, Phosphorus doped silicate SOG and Siloxane SOG with high organic dopants [103]. SOG has been demonstrated as an alternative to LPCVD or thermally grown  $\text{SiO}_2$  due to lower deposition time, and ease of deposition [104]. SOG is typically deposited via spin coating onto a wafer and then cured in a furnace to form  $\text{SiO}_2$  layer. SOD films can then undergo diffusion doping at elevated temperatures. A uniform layer is achieved in small sample sizes but is significantly affected by large full wafer substrates as the film quickly solidifies on the surface due to high evaporation rates resulting in poor uniformity. High acceleration speeds can reduce this affect but results in only 1% of the applied liquid being used to form the layer thus resulting in large amounts of wasted material. SOG and SOD liquids are expensive compared to traditional resists thus the high amount of liquid wasted is not desirable.

MEMS devices often have high aspect ratio 3D topography which cannot be conformally coated using traditional spin coating techniques. Due to its strong mechanical qualities, SU-8 is frequently utilized as a resin for high aspect ratio MEMS device architectures, microchannels for microfluidics, and bioMEMS devices [105, 106]. Photoresist spray coating was previously developed to overcome the 3D topographical structure coating challenges [101]. However, spray coating resulted in poor uniformity.

Spin-spray technique was developed [107], as a method of overcoming the drawbacks of spin coating and spray coating i.e., non-uniformity by combining the two methods. Spin-spray coating involves spraying the liquid on the substrate while spin coating. This method has been demonstrated for various films including transition metal ferrites deposition [108], optically transparent ZnO [109], and photoresist [110]. Spin spray deposition was used to enhance uniformity of the layer across the wafer and reduces the amount of solution needed to cover the wafer. However, current spin-spray methods use air pressure or ultrasonic atomization methods which have several disadvantages including limited droplet control resulting in wide range of large droplet sizes ( $>50\ \mu\text{m}$ ) [111-113]. In addition, ultrasonic spin-spray technology requires a bulky setup which makes it difficult to integrate into a standard spin coater. As the system requires high power consumption, bulky equipment to actuate the ultrasound device, fluid syringe pump, and the atomizer (ultrasound device, nozzle, and baffle).

### **6.1.1 Spin Spray Deposition Experimental Setup**

The spin-spray setup using the silicon vibrating mesh atomizer, Laurell Spin coater, and a custom PCB with circuitry is demonstrated in figure 6.1. A hole in the lid of the spin coater which is typically used for dispensing liquid onto the substrate was used for the atomizer, which was placed over the hole and taped down. Liquid was then placed on the top of the mesh

membrane and atomized by powering the system. The overall setup is easy to integrate onto any spin coater and can be easily removed for standard spin coating applications.

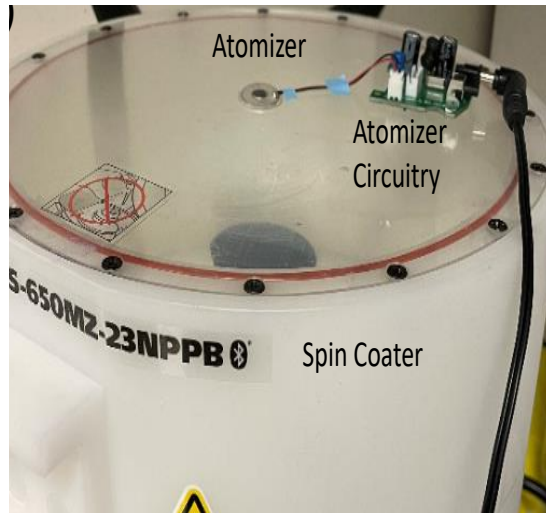


Figure 6.1 – Image of spin-spray setup using vibrating mesh atomizer.

To validate atomization the droplet size distribution of the aerosols was measured using laser diffraction technology (Sympatec particle analyzer). Initial testing was performed on 50 mm silicon wafers with undoped SOG (Desert Silicon NDG-5000R) with viscosity of  $0.9 \pm 0.15$  cps. The Si wafer was cleaned for 5 minutes with 4:1 mixture of Sulfuric acid ( $H_2SO_4$ ) and hydrogen peroxide ( $H_2O_2$ ) at  $100^\circ C$  and then immersed in 6:1 BOE etchant to remove native oxide and spin rinse dried in DI water and then dehydrated on a hot plate at  $100^\circ C$  for 10 minutes. The spin spray deposition involves spraying the SOG at a rate of 0.05 ml/s on the spinning substrate at a low speed (300-500 rpm) for 15 s. After the spraying, the spinning rate was increased at an acceleration rate of 5000 rpm/sec until the desired final speed was achieved (according to Table 6.1). The final speed was held for 30 s to remove excess solution from the wafer. The conventional spinning method was also employed to deposit SOG film for comparison with the different spin speeds specified in Table 6.1 at an acceleration of 5000 rpm/sec for 30 seconds. Both methods were then soft baked at  $150^\circ C$  for 1 hour in a convection

oven and then cured at various temperature ranging from 200°C to 1000°C with a step of 200°C for 1 hour in a N<sub>2</sub> furnace to study the uniformity and quality of the film deposited by the two methods. Thermally grown SiO<sub>2</sub> is the gold standard of oxide quality. To compare the results of the SOG oxide a wet thermal oxide of 500 nm was grown on the (100) Si wafer.

Table 6.1 - Spin speed variations.

<b>Method</b>	<b>Final Spin Speed (rpm)</b>	<b>Spin speed during spray (rpm)</b>
Spin coat	2000,3000,4000,5000	N/A
Spin Spray	5000	300,400,500
Spin Spray	2000,3000,4000,5000	500

The etch rates of SiO<sub>2</sub> film formed by the two methods were studied with wet etchant (6:1 BOE), Vapor HF (Idonus HF Vapor Etcher), and RIE. The wafer temperature was maintained at 40°C and HF vapor generated at 30°C. RIE plasma etching was performed at 250 W, 300 mTorr pressure, 250 sccm of CF<sub>4</sub> and 50 sccm of O<sub>2</sub> gas flow. The film thickness with varying spin speed was measured by Nanometrics CTS 102. Spin and spin spray methods were also studied for 3D structure conformality using a 10x10 mm die, with 40 μm thick silicon structures created using DRIE. For the 3D topography experiment both methods applied 2 drops of SOG at the center of the die. Surface roughness of SOG was measured by Digital Instruments Atomic force microscope. The scan size 1 μm x 1 μm and each measurement contain 256 x 256 data points. Film stresses of the SiO<sub>2</sub> films were measured using a Flexus stress measurement tool.

To demonstrate that the vibrating mesh spin-spray method could be applied to photosensitive materials. Photolithography was performed with SU-8 2000.5 resist with viscosity of 2.5 cps

on piranha cleaned Si wafer with the spin spray deposited at 500 rpm spin speed while spraying for 10 seconds and 5000 rpm final spin speed with 5000 rpm/sec ramp rate for 30 seconds. The Su-8 layer was then soft baked at 95°C for 90 s, exposure with Exposure-masking system UV-KUB2 at 4 mW/cm<sup>2</sup> intensity for 15seconds followed by post exposure bake at 95°C for 90 s and developed in SU-8 developer for 60 s.

To determine the conformal coating capability of the spin-spray method using the Si-vibrating mesh atomizer, 3D topographical samples were created using KOH etched silicon cavities of 40 µm diameter and thickness of 10-15 µm. The samples were then coated with Su-8 2000.5 using traditional spin coating and spin-spray method using the vibrating mesh atomizer. The spinning profile for the spin coated sample had an initial spin speed of 500 rpm for 10 seconds with 5000 rpm/s ramp and final speed of 5000 rpm for 30 seconds. The conformality of the coating was inspected by looking at the cross-section images with SEM.

### **6.1.2 Characterization of produced film properties – Etching, Uniformity, Roughness and Pattern ability**

The thickness of both methods decreased as spin speeds were increased, as expected by spin theory. The spin-spray method resulted in thicker films compared to spin coating, which was likely due to the low amounts of liquid being spun off the wafer, thus there was more liquid on the surface that was used to create the film. Spin spray layer thickness with different initial speeds during spraying is shown in figure 6.2(b) resulting in thick films with 5500 Å value at 300 rpm speed and thin film with 3200 Å at 500 rpm speed during spraying. Speeds lower than 300 rpm resulted in poor coverage of the substrate and cracks after curing. Low ramp rates resulted in poor coverage as the SOG likely crystallized or evaporated before a uniform coat could be generated.

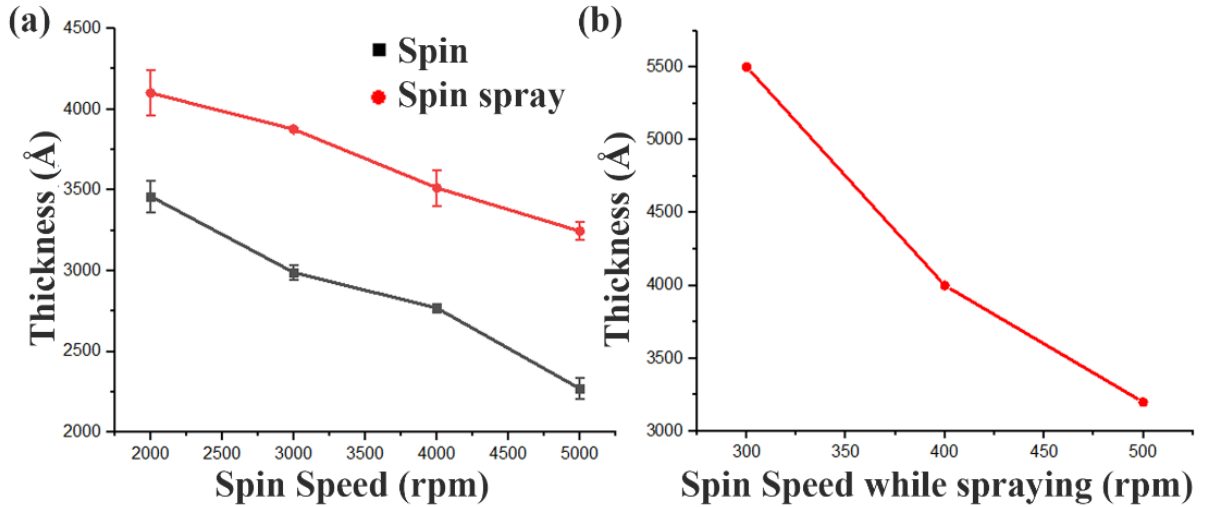


Figure 6.2 – (a) SiO<sub>2</sub> film thickness w.r.t final spin speed (b) Spin speed while spray process.

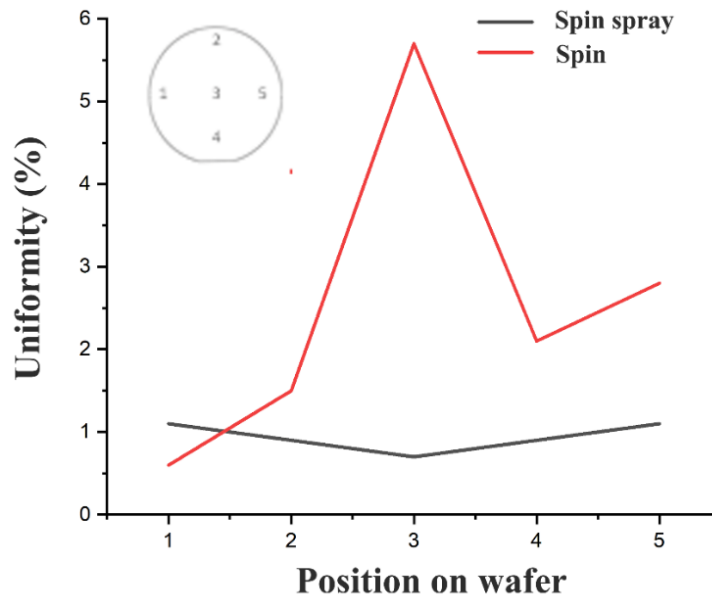


Figure 6.3 - SiO<sub>2</sub> film thickness at various positions on the wafer with final spin speed of 5000 rpm.

The spin spray method used approximately 0.75 ml of SOG to coat a 100 mm wafer compared to approximately 4 ml of SOG used during traditional spin coating. This means less material is wasted. Thus a 125 ml bottle of SOG could potentially coat about 130 more wafers than spin

coating. Uniformity of the wafer is shown in figure 6.3 considering five main points on the wafer. The Spin spray coated SiO<sub>2</sub> layer had a uniformity of < 1% (center and edges) as the spray was able to cover a larger area of the wafer. Spinning while spraying caused the liquid to spread uniformly during deposition which prevented it from evaporating at a specific location. Spin coated SiO<sub>2</sub> layer was thick at the center of the wafer and thin at the edges due to dispensing the solution at the center and SOG tends to crystallize quickly creating a thicker layer at the center of the wafer thus resulting in decreased uniformity across the wafer with a peak uniformity error of 5.7% in the center of the wafer.

Etch rate of the SiO<sub>2</sub> films deposited with different annealing temperatures is shown in figure 6.4. Fig. 6.4(a) shows the etch rate in 6:1 BOE wet etchant. Film annealed at low temperature, 200°C demonstrated higher etch rate for both spin and spin spray coated layer due to lower density of SiO<sub>2</sub> film. As the annealing temperature increased the density and overall quality of the SiO<sub>2</sub> film increased thus reducing the etch rate. For 1000°C annealed samples the etch rate of spin spray SiO<sub>2</sub> layer was 16.9 Å/sec which was similar to the etch rate of thermal grown SiO<sub>2</sub> (16.6 Å/sec). Fig. 6.4(b) shows the etch rate of the SiO<sub>2</sub> in RIE plasma etch. Films deposited by both methods demonstrated the same trend i.e., increased etch rate at low anneal temperatures and decreased etch rate at higher anneal temperatures. Spin spray SiO<sub>2</sub> etches slightly slower than spin SiO<sub>2</sub> making it suitable for MEMS device. Fig. 6.4(c) shows the etch rate in vapor HF. Etch rate in vapor HF was 150 Å/sec for spin sprayed layer and 115 Å/sec for spin coated layer both annealed at 200°C. The etch rate decreased to 60.3 Å/sec for spin sprayed layer and 32.33 Å/sec for spin coated layer annealed at 1000°C. The etch rates can be decreased by increasing the temperature and increasing wafer temperature resulted in lower

etch rate. The comparison of the etch rates of Spin spray, spin and thermal grown SiO<sub>2</sub> is shown in Table 6.2.

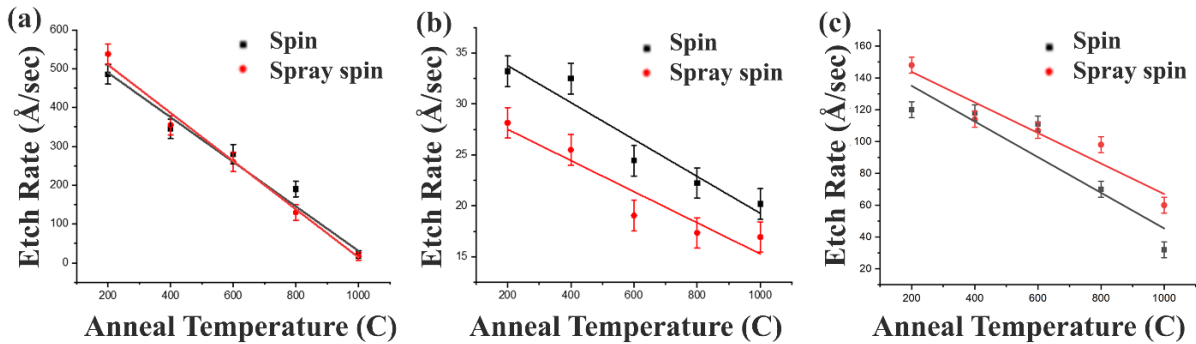


Figure 6.4 –(a) Etch rate with 6:1 BOE etchant, (b)Etch rate with RIE plasma etcher, (c) Etch rate with Vapor HF. Black and red lines represents best linear fit of the points and error bars represent the standard deviation.

Table 6.2 – Etch Rate Variations.

Etchant	Spin SOG Etch Rate (Å/min)	Spin spray SOG etch Rate (Å/min)	Grown SiO <sub>2</sub> Etch Rate (Å/min)
6:1 BOE	1332	1008	1000
Vapor HF	2200	3000	2000
Plasma Etch (RIE)	1212	1014	1128

The film stresses for wet thermally grown SiO<sub>2</sub>, spin coated, and spin-spray coated using the vibrating mesh technology are demonstrated in figure 6.5. The spin and spin-sprayed films had a final spin speed of 5000 rpm. The results demonstrate that all three SiO<sub>2</sub> films demonstrated compressive stress in the range of 100 MPa. The spin-spray coated film had a slightly higher film stress of 138 MPa compared to thermal grown (109 MPa) and spin coated SiO<sub>2</sub> (104 MPa).

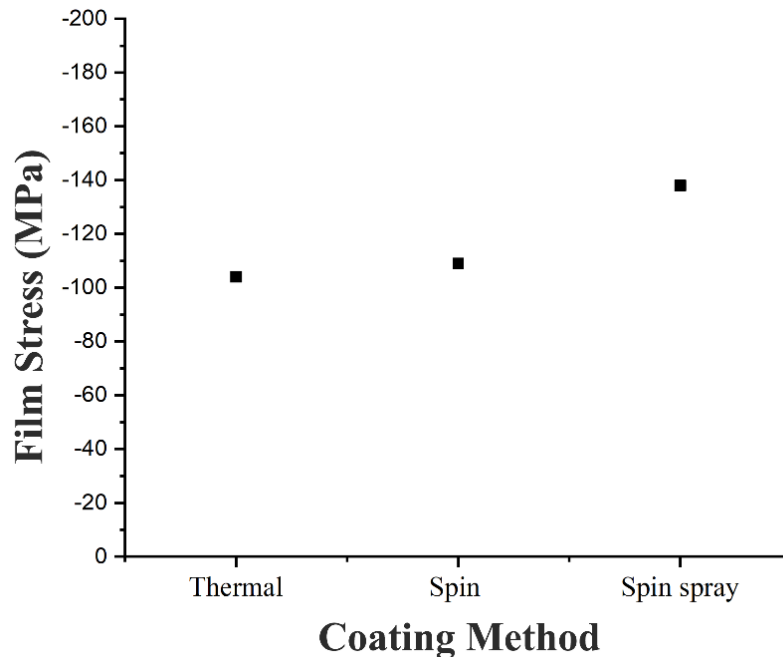


Figure 6.5 – SiO<sub>2</sub> film stress deposited by various methods with thicknesses of (500 nm, (thermal), 220 nm (Spin), and 320 nm (spin-spray)).

The absorbance of the three SiO<sub>2</sub> films (thermal, spin, and spin-spray) were measured using a UV spectrophotometer and the results are demonstrated in figure 6.6. At low wavelengths (< 400 nm) the three films had similar absorbance peaks with the exception of a peak at 320 nm for the thermal grown oxide. However, at higher wavelengths the thermal and spin-spray films had peaks at 567nm and 643 nm whereas there were no absorbance peaks of the spin coated samples. This demonstrates that the spin-spray oxide better resembles the absorbance of thermal oxide at higher wavelengths.

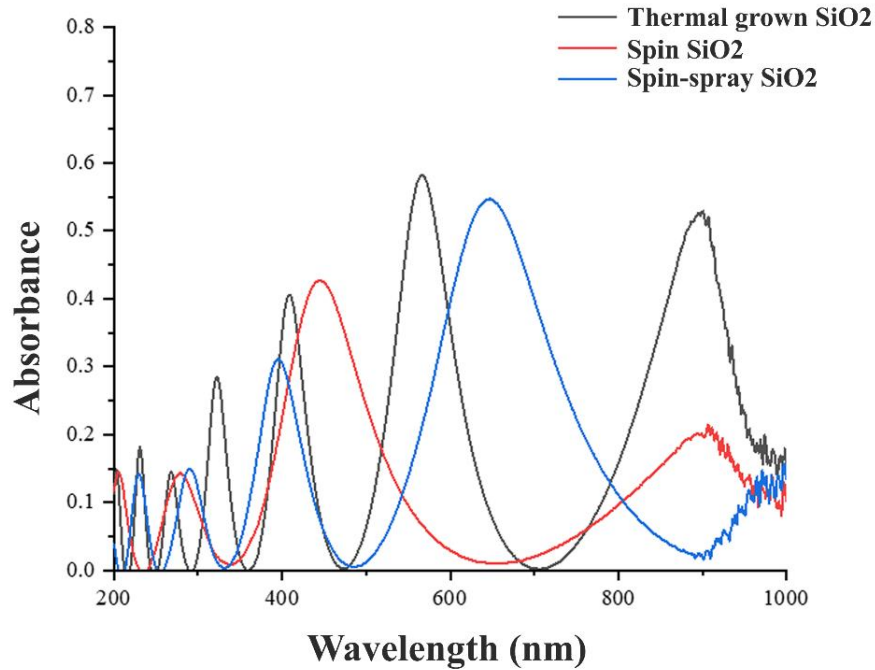


Figure 6.6 – Absorbance as a function of wavelength for thermal, spin, and spin-spray coated films of SiO<sub>2</sub>.

Figure 6.7 demonstrates the conformality of SiO<sub>2</sub> for both methods for high 3D topography structures. Fig. 6.7(a) and (b) shows the normal and zoomed in SEM image of a 3D structure etched by DRIE coated by spin method. The results demonstrate that the liquid SOG successfully coated the top surface with a SiO<sub>2</sub> layer but no traces of SiO<sub>2</sub> are present on the sidewalls of the structures. Fig. 6.7(c) and (d) shows the same structure coated with spin spray method, which demonstrated a more conformal coating of the top, bottom, and sidewalls of the high aspect ratio structure. Cracking is due to intentional thermal shocking and stress at the corners or edges as the structures were 40 μm deep. Stress cracking issues can be reduced by annealing the samples at low ramp rates. The coating was tested on small samples of 1 x 1 cm<sup>2</sup> larger substrates would likely have less coverage for spin coated methods. However, the spin-spray method can easily be applied to coat larger substrates.

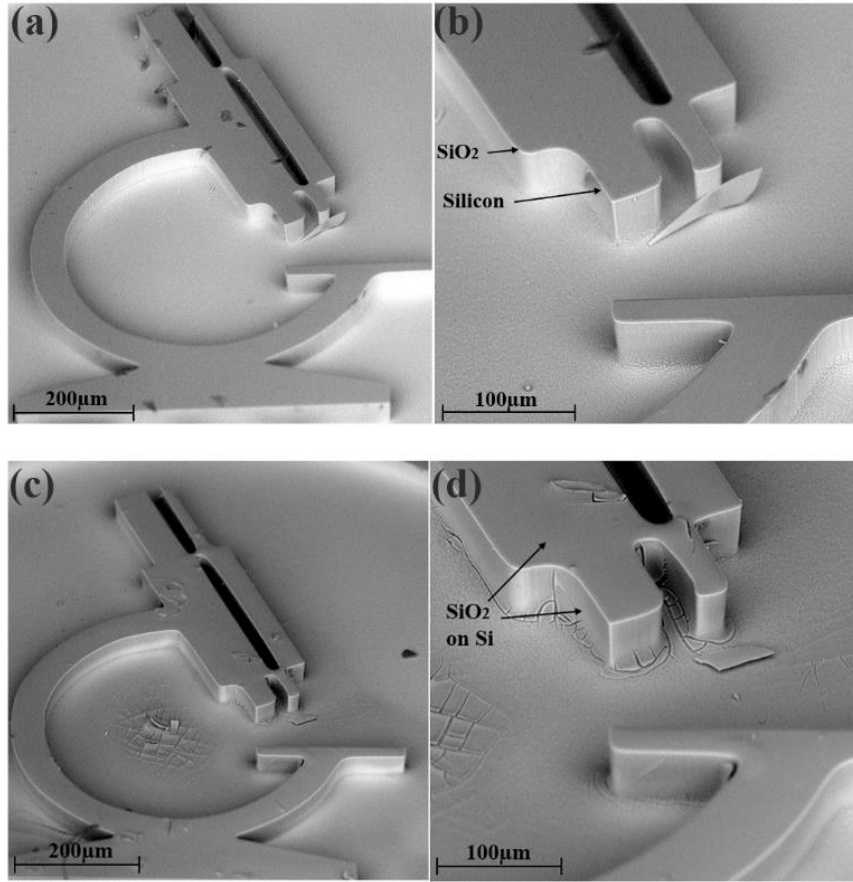


Figure 6.7 – (a), (b) SEM images of 3D structure coated by spin coating, (c) and (d) SEM images of 3D structure coated by spin spray method.

Figure 6.8 demonstrates the surface profiles of the film deposited by spin-spray coated SiO<sub>2</sub> and spin coated SiO<sub>2</sub>. The AFM images of a (1 µm x 1 µm) of the two films demonstrate a higher surface roughness for spin coated samples. The RMS roughness of the two films were 15.1 nm and 28.97 nm for the spin-spray and spin coated films, respectively. The higher surface roughness of spin coated SiO<sub>2</sub> is due to the evaporation or crystallization which causes some areas to crystallize before a uniform layer can be deposited. The spin-spray method resulted in a smoother surface as the droplets were allowed to spread across the wafer before it could be crystallized.

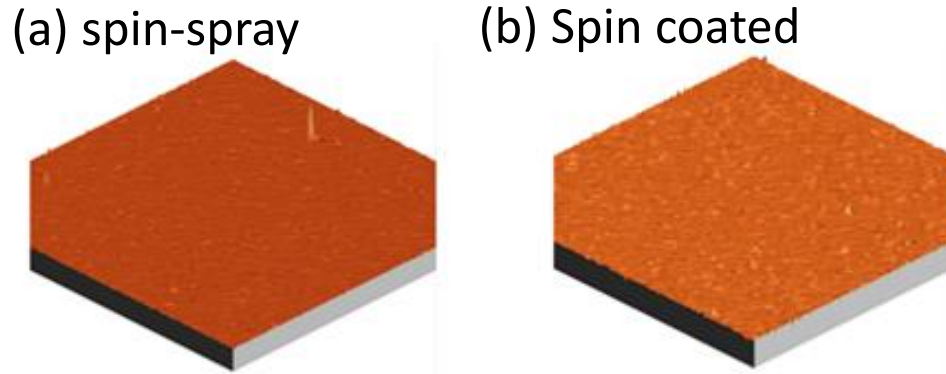


Figure 6.8 – AFM surface profiles: (a) Spin-spray coated SiO<sub>2</sub>, (b) Spin coated SiO<sub>2</sub>.

Figure 6.9 shows the structures patterned with the SU-8 resist coated by spin-spray method. A uniform and defect free layer are obtained and variety of shapes in different dimension is patterned by optimizing the parameters such as time of spray during deposition as spray time more than 10 seconds resulted in Su-8 droplets forming an initial layer and thus resisting spinning flow, which created defects in the patterned structures. Ability of the vibrating mesh atomizer to spin-spray deposit SU-8 resist makes it easy and simple to deposit and pattern by lithography. Other low viscosity resists could also be used. There was no significant clogging of the nozzles from the Su-8.

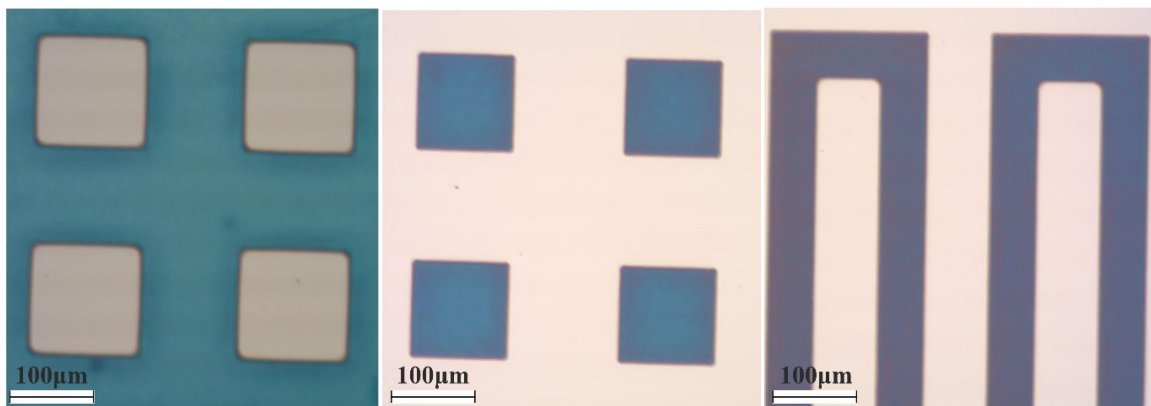


Figure 6.9 – SU-8 resist patterned structures with spin-spray deposition method.

Conformal coating capabilities of 3D structures using Su-8 that was deposited using spin coating and spin-spray coating using the vibrating mesh atomizer is demonstrated in figure 6.10. A more uniform 1.6  $\mu\text{m}$  thick layer was deposited with spin-spray method on the sidewalls and bottom surface of the etched circles. Whereas in case of spin method only the bottom surface is covered with the resist. The resist settled at the bottom of the cavity resulting in a thicker bottom coating of 2.56  $\mu\text{m}$  and no visible sidewall coverage. The resist thickness was repeatable over all the cavities regardless of the position of cavities on the wafer with less amount of resist consumed with spin-spray method. The results agree with previous ultrasonic spin-spray deposition studies.

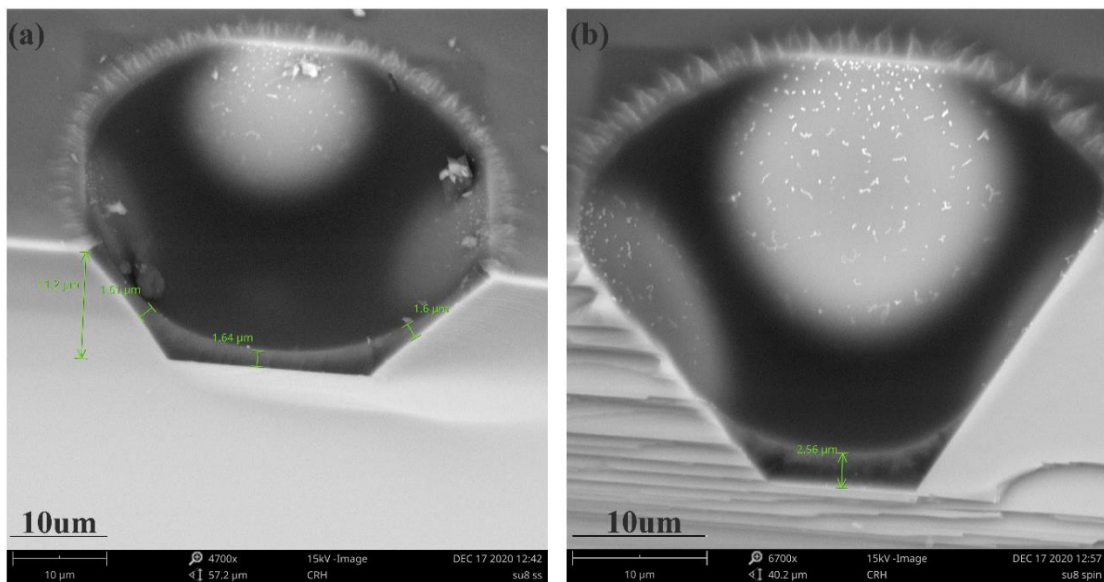


Figure 6.10 – KOH etched cavities coated with (a) Spin-spray method, (b) spin coating method.

This section demonstrates the ability to conformally deposit thin films of liquid-based materials using spin-spray deposition method employing vibrating mesh atomizer. The spin-spray method resulted in enhanced uniformity across the wafer and lower waste material, thus making it especially useful for high-cost liquids. Various low viscosity liquids including SOG,

and SU-8 resist were conformally coated on high aspect ratio 3D topography structures using the new atomizer. This new method of coating SOG can be used as a passivation layer for complex topography structured devices and could be applied to SOD to create enhance doping capabilities of 3D structures. The concept could be applied to various other liquid materials including conducting inks. Atomization of higher viscosity photoresists and liquids needs to be further investigated in the future. Vibrating mesh technology atomization spin-spray manufacturing offers significant advancement over traditional ultrasonic spin-spray such as easier integration on to a spin- coater, easier stimulation circuitry, better control of droplet sizes to enhance film uniformity, and lower power consumption. This study validates that vibrating mesh technology can be used as an alternative to ultrasonic spin-spray deposition to create uniform thin films from liquids.

## **6.2 Spray cooling using MEMS vibrating mesh atomizer**

This section reports on the novel use of a MEMS based vibrating mesh atomizer (VMA) for spray cooling applications. The work focuses on the fabrication of the MEMS VMA along with experimental analysis comparing the cooling performance to a metallic stainless steel VMA based on droplet size distribution and its effect on cooling rate. The study on heat transfer through spraying on a metal ceramic heater substrate using MEMS and metallic VMA for water, Isopropyl Alcohol, and PEAK (Antifreeze+coolant) as three different spray liquids. The nozzle size of 5 $\mu$ m was used and tested for spray height of 10mm, 20mm and 30mm. It is demonstrated that the droplet distribution with more uniform size droplets and low span value produced from the MEMS device and large spray angle is more effective in cooling a heated substrate compared to large droplet size distribution and small spray cone angle from the metallic non-MEMS device.

Thermal management is an important task in microelectronic components and miniaturization of the components such as nano structured surfaces [114] and nanosized transistors generate high heat flux due to high power density. Spray cooling is the powerful thermal control tool widely applied in medical systems, power electronics, energies, laser, etc. To maintain low operating temperatures, low-cost thermal solutions with little power input and adaptability are necessary, boosting the device's dependability and performance. Liquid cooling is required if the power dissipation level increases and it involves single-phase cooling in microchannels, spray cooling, jet impingement cooling, heat pipes, etc. Spray cooling is a high heat flux, uniform, and efficient cooling technique that has been shown successful in a variety of applications due to its several efficient heat transfer mechanisms. However, spray cooling's cooling capacity and efficiency must be increased to satisfy the demands of next-generation

ultrahigh-power applications. Spray cooling is a complicated process divided into four regions involving single phase heat transfer, nucleate boiling, transition boiling and film boiling. The complexity of spraying, such as spray dynamics and temperature response, are not completely understood, particularly for micro spraying through MEMS atomizers.

The spray cooling performance are mostly focused on pressure control, flow rate of the coolant, nozzle tip, nozzle arrangement, target to nozzle distance, surface type and working conditions[115-118]. Heat transfer coefficient was improved to 8500W/m<sup>2</sup>K by using wicking grooves[119]. The mass flow rate of the coolant impacting heat transfer was investigated in [120] and it was discovered that the dilute spray has greater cooling performance than the dense spray. [121] investigated the spray characteristics and effect of roughened silicon surface compared to smooth on heat transfer performance using DI water as working medium. Pulsed spray cooling at varying spray to target distance using R404A coolant was examined to study changes in temperature in [122]. Nozzle inlet pressure was experimentally examined over the range of 0.6-1MPa to study the cooling performance including heat transfer coefficient, surface temperature and critical heat flux (CHF) for the closed cooling cycle using R22 coolant in[123] and concluded that as pressure increases, the CHF increases and decreases.

Nozzle selection is very important for spray cooling. Most of the research in spray cooling applications involve the use of air pressure for spray generation which require high power to operate (>100 W), have large droplet distribution (believed to reduce cooling rates), bulky (multiple components), and are not ideal for integration into microsystems [2]. Recently, PZT actuated mesh atomizers which has relative advantages over traditional methods such as low velocity, controlled droplet distribution, simple and compact assembly, and low consumption has been widely used in spray generation but its application in spray cooling is quite limited.

Mesh atomizers use a PZT actuator, which takes a high-frequency electrical signal from a power source and converts it to mechanical oscillations in a thin mesh membrane, which then creates a pumping action on the liquid in contact with the membrane and squeezes it out in the form of droplets repeatedly, forming spray. Commercial vibrating mesh atomizers consist of stainless-steel membrane manufactured using laser drilling method or Pd-Ni electroplating[124]. Metallic atomizers are extensively researched in various aspects such as dynamics[125], atomization rate[61] and effect of operating parameters on its performance[126]. Numerous researchers have investigated the design parameters of metallic atomizer in spray cooling applications. [127] performed an experimental study on flow and heat transfer for a single hole micro nozzle and concluded spray velocity is influenced by spray height and surface initial temperature and thus, affecting CHF. An experimental study on micro spray based cooling with PZT atomizer was performed applied to high power LEDs[128] to study effect of cooling. Recently, Silicon based VMA were developed using MEMS microfabrication techniques to increase yield, reduce manufacturing cost and add functionality[10, 42, 43]. The working criteria and dynamics of the MEMS VMA is similar to the metallic VMA but offers relative advantages such as enhanced droplet distribution, design modifications such as customization in nozzle size, membrane dimension, membrane material and surface properties.

In this work, a low power (<1 W), low-cost MEMS vibrating mesh atomizer is developed and employed to study the spray characteristics in terms of spray cone angle and its effect on heater surface cooling history. This paper experimentally compares the performance of a microfabricated MEMS VMA to a Metallic VMA device with laser drilled apertures to demonstrate the effects of droplet distribution and spray cone angle on spray cooling rates.

## 6.2.1 Experimental Setup

For comparative study, the metallic atomizer with  $5\mu\text{m}$  outlet chosen was SMMOD10F190, STEMiNC which operates at the resonant frequency of 190kHz respectively. The experimental apparatus schematic for spray cooling using VMA is shown in figure 6.1. In a loop, driving voltage and particular driving frequency is supplied by a pulse waveform generator (TG5011 AIM TII Instruments) and high frequency amplifier (Model 2100HF Trek).

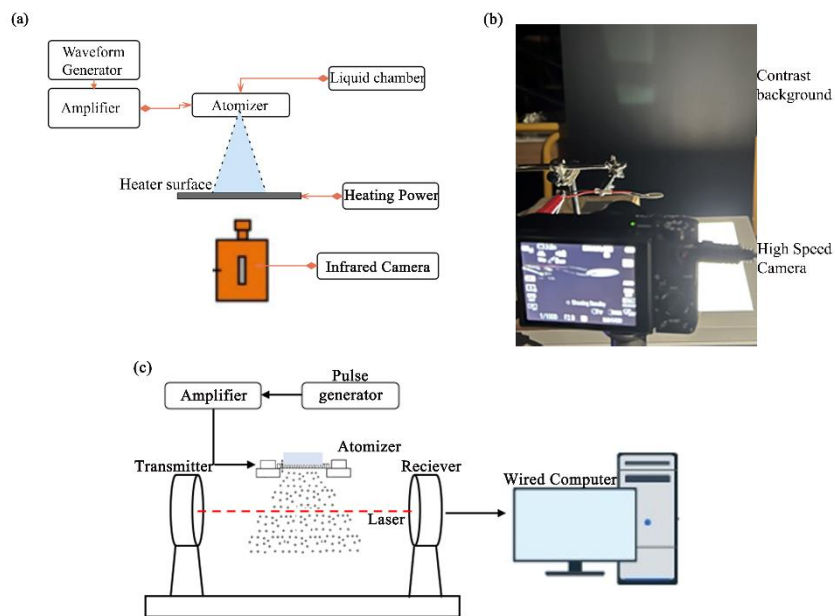


Figure 6.11- (a) Schematic of the spray cooling setup, (b) setup image of the high-speed camera and device, and (c) Schematic of the droplet distribution measuring system.

The cooling measurement system consist of a circular metal ceramic substrate ( $4.029\text{cm}^2$  area and  $0.5\text{mm}$  thickness) was heated using a temperature controller. Thermal infrared imager (PI 640i Microscope optics) with measuring range of  $0^\circ\text{C}$ - $250^\circ\text{C}$  with an accuracy of  $\pm 1^\circ\text{C}$  was used to monitor temperature of the substrate. Droplet size distribution was measured using a laser particle analyzer (Sympatec) based on laser diffraction principle with the measuring size range of  $0.9\mu\text{m}$ - $175\mu\text{m}$ . The spray cone angle was determined by post processing the images

captured by D3500 Nikon NIKKOR 18-55mm lens and the setup is shown in figure 6.1(c) and to keep the image's contrast, the backdrop was darkened. The two devices, Metallic and MEMS devices were experimentally tested for different coolants – Water, Isopropyl Alcohol (IPA), and PEAK Antifreeze+coolant.

During spray cooling, the metal ceramic heater was first heated to 100°C using a temperature controller, then switched off and coolant was sprayed over the testing surface after it reached the set temperature. After the surface temperature achieved a constant level, the temperature measurement was discontinued. Temperature was measured using an infrared thermal sensor that took 1 second intervals. For present study the main variables were voltage supply to the device, coolants, and impact height for metallic and MEMS atomizer device.

To assess the cooling efficacy of the MEMS device, a study to compare the heat flux removal capacity of the MEMS device against a Metallic device was performed. To achieve this, a ceramic substrate was preheated to 100°C and the temperature was physically measured using a thermocouple to track the temperature variations during the experiment. Employing Eq. 1, the total heat loss ( $\dot{Q}_L$ ) can be estimated if the mass ( $m$ ) and the heat capacity ( $Cp$ ) of the substrate are known and the variations of temperature with time ( $\frac{\Delta T}{\Delta t}$ ) are measured. The total heat loss has two major components, the natural convective ( $\dot{Q}_{nc}$ ) and forced convective ( $\dot{Q}_{fc}$ ) heat losses as shown in Eq 2.

$$\dot{Q}_L = m Cp \frac{\Delta T}{\Delta t} \quad (1)$$

$$\dot{Q}_L = \dot{Q}_{nc} + \dot{Q}_{fc} \quad (2)$$

Similarly, normalizing Eq 2. By the top area of the substrate, Eq. 2 becomes Eq. 3 where the natural convective ( $\dot{q}_{nc}$ ) and forced convective ( $\dot{q}_{fc}$ ) heat flux components make up for the total heat flux loss ( $\dot{q}_L$ ).

$$\dot{q}_L = \dot{q}_{nc} + \dot{q}_{fc} \quad (3)$$

Knowing this, the cooling heat flux component from the nozzle spray can be found by calculating the total heat flux and natural convective heat flux as seen in Eq. 4. Therefore, by measuring the temperatures without any spray cooling, the natural convective heat flux loss can be estimated.

$$\dot{q}_{fc} = \dot{q}_L - \dot{q}_{nc} \quad (4)$$

Similarly, while employing the spray cooling the total heat flux loss can be estimated. Thus, taking the difference as shown in Eq. 4, the final equation to estimate the forced convective heat flux component can be represented with Eq. 5.

$$\dot{q}_{fc} = \left. \frac{m Cp \Delta T}{A \Delta t} \right]_{with\ spray\ cooling} - \left. \frac{m Cp \Delta T}{A \Delta t} \right]_{without\ spray\ cooling} \quad (5)$$

### 6.2.3 Results and Discussion

For the two devices in our investigation the droplet size distribution, which reflects the quality of atomization, was evaluated. Figure 3(a-f) demonstrates the droplet size distribution curve of water, IPA, and ethylene glycol coolant for the two devices with a 5  $\mu\text{m}$  outlet nozzle. A summary of the results is shown in Table 6.3. The results demonstrate that the MEMS VMA had a narrower droplet distribution with a span  $((X90 - X10)/X50)$  of 0.59, 0.40 and 0.88 for water, IPA, and coolant where X10, X50 and X90 are droplet size which accounts for 10%, 50%, and 90% of total cumulative percentage of volume of all droplets produced. The metallic commercial VMA device demonstrated a significantly higher span of 1.23, 0.79, and 1.5 for

water, IPA, and ethylene glycol coolant respectively. The span which represents the width of the distribution was significantly higher in the metallic membrane compared to the Si membrane for all mediums investigated. The volumetric median diameter (VMD), which corresponds to the midpoint of the droplet size was significantly lower for the MEMS device compared to the metallic devices. The span and the VMD indicate that the MEMS droplet size was both smaller and more uniform than the metallic membrane. Span and VMD are two significant characteristics used to define the droplet distribution quality, however they are reliant on the liquid physiochemical properties (density, surface tension and dynamic viscosity) as well as the nozzle shape and geometry (orifice diameter, thickness). However, by keeping the liquid physiochemical properties the same, we determined that the change in the span and VMD were due to the mesh membrane properties. The droplet distribution highly depends on the volume of the liquid pumped in and out of the nozzle in every single cycle, which further depends on the deformation of the membrane, operating frequency and shape and geometry of the nozzle. In previous chapter, it has been discussed that the change in volume of micro-cone nozzle depends on the thickness of the membrane ( $h$ ), change in taper angle during positive and negative cycle and the total flow rate depends on change in volume of nozzle, operating frequency, and number of holes.

The size of the droplets influences the overall volume of the drops produced as well as the overall flow rate of the device. The flow rates of water, IPA, and ethylene glycol coolant using MEMS devices were  $171 \pm 10 \mu\text{L}/\text{min}$ ,  $110 \pm 5 \mu\text{L}/\text{min}$ , and  $30 \pm 3 \mu\text{L}/\text{min}$ , respectively. Whereas the commercial metallic VMA had a flow rate for water, IPA, and coolant of  $200 \pm 8 \mu\text{L}/\text{min}$ ,  $120 \pm 5 \mu\text{L}/\text{min}$ , and  $38 \pm 2 \mu\text{L}/\text{min}$ , respectively. The flow rates for the MEMS and metallic

atomizers were comparable with a slight increase for the metallic membrane with the same applied voltage.

The control of droplet size has a significant impact on the cooling rate, as smaller droplets increase the mixing intensity and increases the surface to volume ratio of the liquid droplets thus improving the cooling effect [129]. The droplet size and homogeneity were unaffected by changing the supply voltage for both devices, however the droplet density distribution increased as the voltage was increased. The spray droplet distribution impacts the dispersion of the droplets which affects the spray angle; therefore, it was critical to investigate the angle and parameters that influence it in order to enhance cooling performance.

The nozzle with fine droplets in a spray cooling system intensifies mixing to raise the surface to volume ratio of the liquid droplets, improving the cooling effect[129]. The droplet size and homogeneity were unaffected by changing the supply voltage for both devices, however the density distribution of the droplets formed increased as the voltage was increased. Because the spray droplet distribution impacts the dispersion of the droplets and, as a result, the spray angle, it is critical to investigate the angle and parameters that influence it.

Table 6.3: Droplet density distribution for MEMS and metallic VMA device with various liquids.

Liquid	X10 (μm)		X50 (μm)		X90 (μm)		VMD (μm)		Span	
	MEMS	Comm.	MEMS	Comm.	MEMS	Comm.	MEMS	Comm.	MEMS	Comm.
Water	4.35±0.04	4±0.07	6.20±0.09	7.87±0.14	8.82±0.217	13.73±0.17	6.37±0.11	8.37±0.12	0.72	1.23
IPA	4.97±0.12	6.36±0.2	5.98±0.07	9.75±0.15	7.34±0.13	14.11±0.1	6.87±0.1	10±0.15	0.40	0.79
Coolant	4.22±0.18	3.93±0.16	6.43±0.12	11.70±0.2	9.91±0.11	21.66±0.18	7.10±0.13	12.89±0.18	0.88	1.5

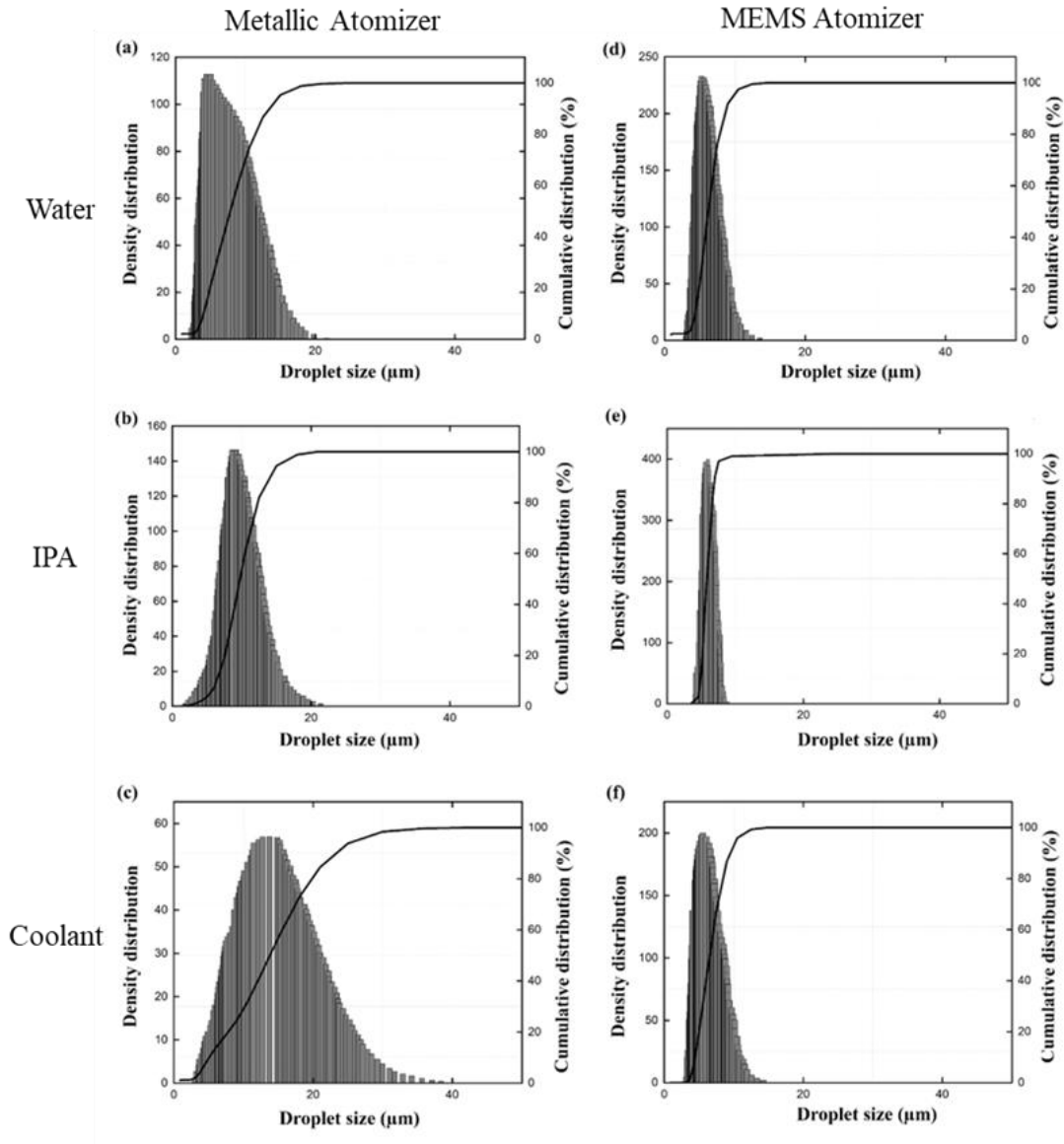


Figure 6.12 - Droplet distribution curve of (a), (b), (c) Water, IPA, and ethylene glycol coolant with metallic atomizer, (d), (e), (f) Water, IPA, and ethylene glycol coolant with MEMS atomizer.

### 6.2.3.1 Spray Angle Measurement

Spray angle demonstrates the angle of the spray generated by the device and directly affects the impacting area on the substrate. Figure 6.3 shows the variation of spray angle for metallic and MEMS atomizer for different coolant tested at 100V supply voltage. The spray angle of

MEMS atomizer was higher (approx.  $3^\circ$ ) than the metallic device for all the coolants. The spray angle observed was maximum for water as coolant i.e.,  $12.9^\circ$  for metallic and  $15.7^\circ$  for MEMS atomizer. For IPA, the angle was approximately  $1^\circ$  less than spray angle of water. Spray angle of glycol coolant was reduced to  $3.35^\circ$  for metallic device and  $6.61^\circ$  for MEMS device as its physiochemical properties (Viscosity – 2.56cP, Density -1.075kg/m<sup>3</sup>) is higher than water and IPA. Due to higher density and viscosity, the atomizer membrane requires higher velocity to create the pumping action and rupture the surface tension force of the coolant. Since the devices operate at (0,2) mode of vibration and has maximum velocity at the center and minimum towards the edge of the membrane, it is able to atomize glycol coolant with comparatively higher viscosity through the center part of the membrane and the spray stream is thinner and hence, the spray angle is less in comparison to other media employed. With all the coolants, it is demonstrated that MEMS device is more capable of impacting larger area. The droplet distribution justifies the MEMS device's large spray angle: the finer the droplets produced, the broader the spray angle, and larger spray angles have more area to scatter the droplets and fewer chances of combination.

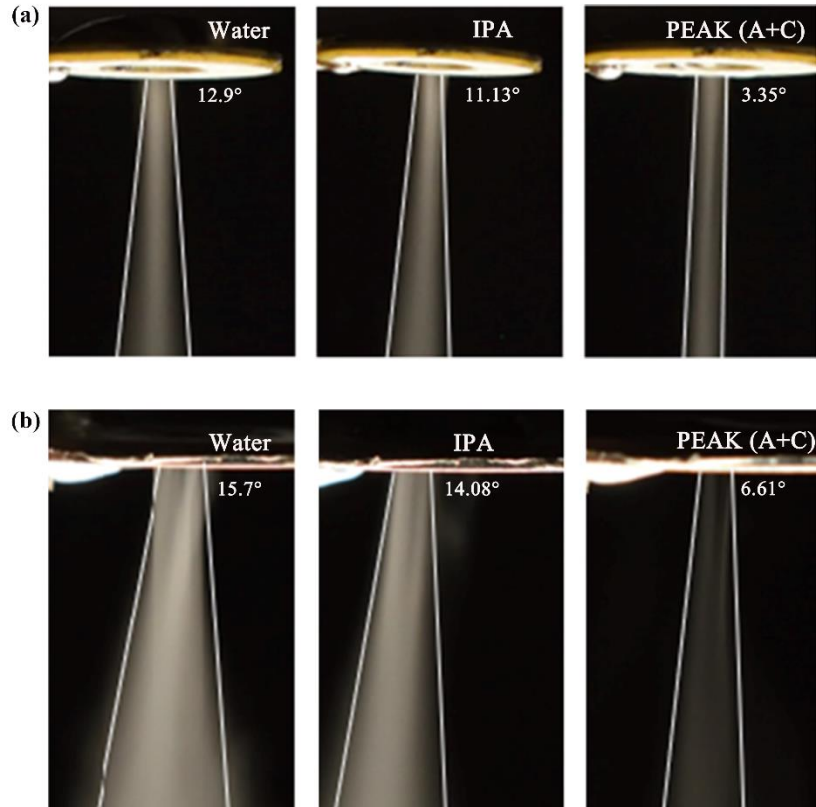


Figure 6.13 – Spray angle of water, IPA, and PEAK (Antifreeze+coolant) for (a) Metallic device, (b) MEMS device.

Figures 6.4 and 6.5 show the results of spray angle with varying applied voltage using water as the medium and operating at the resonant frequency. The peak displacement at the center of the membrane increases with increasing voltage. The increased peak also results in an increased velocity of the membrane, which affects the pressure and force on the liquid. Due to the increase in the peak displacement and velocity of the membrane, the spray angle demonstrated a linear increase with respect to the applied voltage. The increased velocity and displacement spreads radially from the center, so as the applied voltage was increased the displacement away from the center was increased which reaches the atomization threshold. This results in liquid being atomized in nozzles further away from the center as voltage was

increased. At 50V, the spray angle was  $6.54^\circ$  for the metallic atomizer and  $8.20^\circ$  for the MEMS atomizer and the angle increased to  $12.9^\circ$  and  $15.77^\circ$  at 100V. The spray angle of the metallic device was always smaller than the MEMS as expected due to the increased velocity and displacement threshold of metallic VMA compared to Si VMA devices.

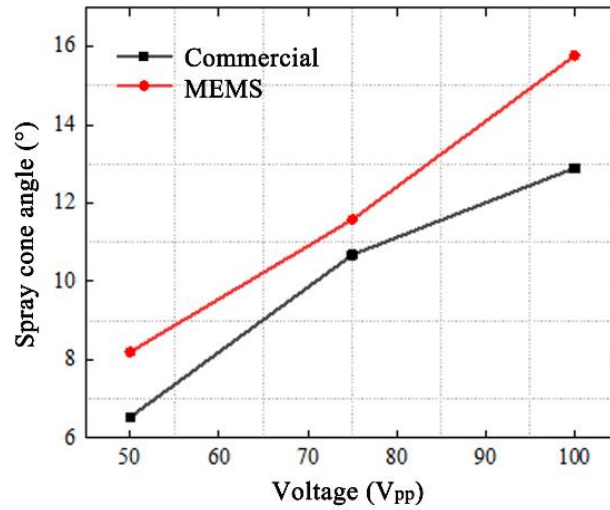


Figure 6.14 - Spray angle comparison for both the devices at variable voltage.

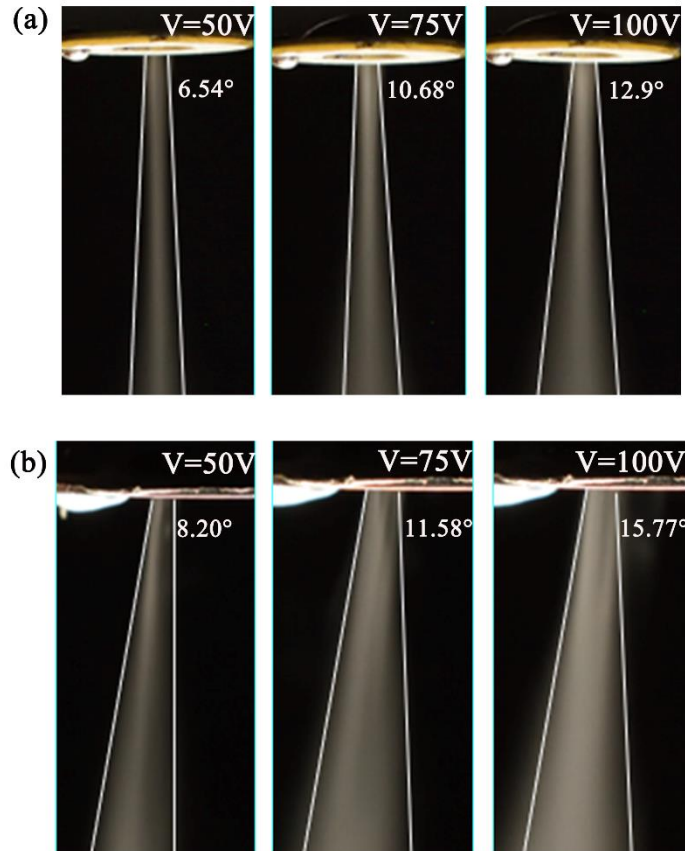


Figure 6.15 – Spray angle at varying supply voltage (a) Metallic device, (b)MEMS device.

### 6.2.3.2 Heat transfer measurements

Three variables of interest were studied using both the MEMS device and the metallic nozzle. First, three different liquid coolants were considered for this study employing a fixed target distance of 10 mm and a voltage of 100 V. Figure 6.6(a) shows the variation of the surface temperature with time using two devices at the impacting distance of 10mm. It is demonstrated that cooling is fast in first 10seconds and it tends to stabilize after 20seconds and cools down slowly after. The film and transition boiling times are quite brief because the heat transfer between the spray and heating surfaces transpired very quickly. The substrate can cool from 100°C to 48°C in 15 sec for MEMS device and water whereas it cools down to 68.3°C for metallic device as the spray would impact less area due to small spray angle. As seen in Figure

6.6(b), water appears to be the best cooling media for both nozzles as it yields the highest heat flux values. However, a clear difference in performance can be observed between the MEMS and the metallic devices. The droplet dispersion created by the two devices is another factor that influences cooling. The metallic device created larger droplets that tended to gather after a period of time, and there was no further heat dissipation or cooling once surface thermal resistance was reached. On the other hand, MEMS device produced more uniform distribution of droplets on heated surface. Even after the surface temperature has reduced, the water droplets tend to evaporate quickly, resulting in improved cooling performance.

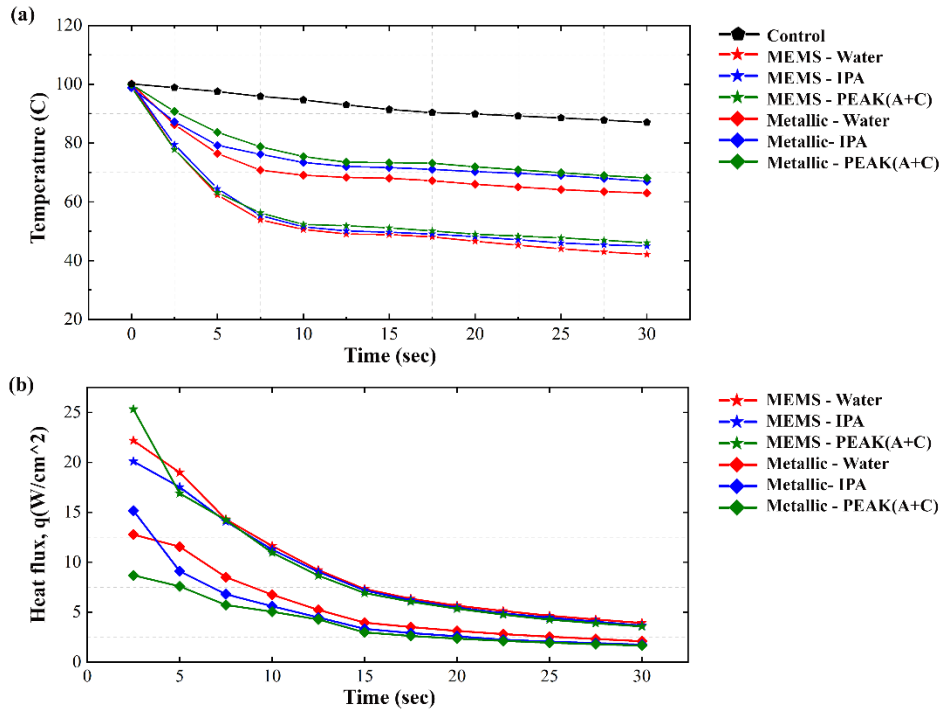


Figure 6.16 – (a) Temperature variation and (b) Heat flux variation with time for different cooling liquids for both atomizers.

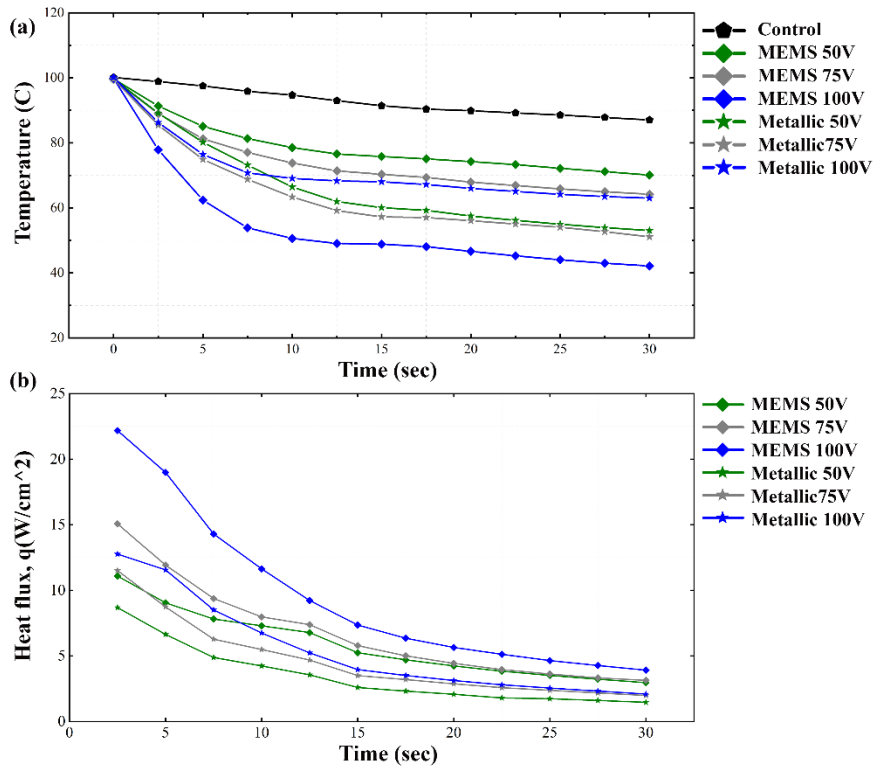


Figure 6.17 - (a) Temperature variation and (b) Heat flux variation with time for the two atomizers.

devices operating at variable voltage.

Similarly, to assess the effect of the voltage applied to the spray nozzles, Figure 6.7(a, b) shows the temperature with respect to time and a comparison of the heat flux removal capacity of the MEMS and metallic devices using water at a distance of 10 mm from the target. For both devices, it appears that 100 V yields the higher heat flux for both devices as the spray angle is highest at 100V so, the spray impacts more area and cools down the surface more in comparison to other operating voltage.

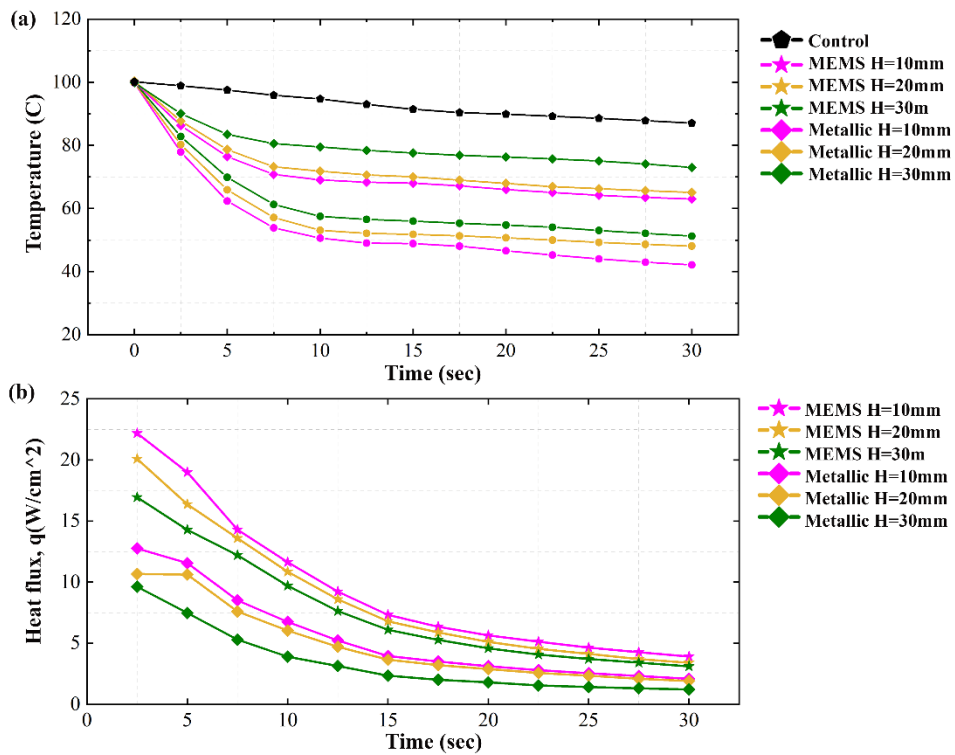


Figure 6.18 - (a) Temperature variation and (b) Heat flux variation with time at different spray height.

Lastly, the impacting height of 10mm, 20mm and 30mm was studied to assess the impact on the cooling capabilities of the devices using water employing a voltage of 100 V. It is demonstrated from temperature variation that impacting height doesn't show huge temperature

difference at 10mm and 20mm height but at 30mm a lot of vortices is created and affects the cooling. Figure 6.8 shows that a smaller distance between the devices and the target yields higher heat flux values. However, it should be noted that in all 3 cases the target was completely covered by the spray.

It should be noted that this is only valid if the Biot Number ( $Bi$ ) is below 0.1. For this case, the maximum heat transfer coefficient allowed to maintain this criterion is approximately 10,000  $W/m^2-K$ . The maximum estimated heat transfer coefficient value for the experiments presented was  $<5000 W/m^2-K$  which validates the lumped capacitance assumption in the calculations.

$$Bi = \frac{h t c}{K} \frac{t}{2} \quad (6)$$

The novel use of a MEMS based vibrating mesh atomizer for spray cooling is developed and investigated. The spray characteristics including droplet distribution and spray angle are investigated experimentally and its effect on cooling performance is studied for MEMS and metallic atomizer. The spray angle of the two devices is found to be dependent on the working fluid, with the angle being higher for less dense liquid and smaller for dense liquid, as well as the driving voltage, with the angle increasing as the voltage increases and reaching its maximum. The cooling performance of the device is affected by droplet size distribution and spray angle, as devices that produce larger and non-uniform droplets tend to have smaller spray angles and low heat flux values, as large size droplets on the surface evaporate at a slower rate than smaller and uniform droplets, limiting the advantage of two-phase heat transfer and resulting in limited temperature drop. MEMS atomizer has higher spray angle and high heat flux values with all the different working fluids and at different voltage and various impacting height than metallic atomizer. In this investigation, the lowest spray height, i.e., 10mm, had the best cooling performance, followed by 20mm and 30mm.

### **6.3 Summary**

This chapter presented the experimentally studied uses of vibrating mesh atomizers. The use of MEMS-based VMA in thin-film development via spin spray deposition is demonstrated to compare the developed film characteristics such as thickness, uniformity, etch rates, and coating of 3D microstructures to the film created using the traditional spin coating method. MEMS VMA-developed thin films that showed better quality (equivalent to thermally grown oxide), uniformity, and ability to coat high aspect ratio structures with less resist consumption. Spray cooling for microelectronic devices is another application investigated in this chapter, which uses MEMS VMA and commercial VMA to examine the influence of droplet size distribution and spray angle parameters on the cooling rate of the heated substrate. The results show that MEMS VMA has a higher spray angle and more controlled droplet size distribution, which contributes to the high cooling rate of the heated substrate in comparison to metallic VMA of the same nozzle outlet dimension.

The two applications encourage the employment of MEMS-based atomizers in additional applications where their significant benefits may be exploited more effectively, such as spray drying applications for drying sub-micron-sized droplets.

## CHAPTER 7

### CONCLUSION AND RECOMMENDATION FOR FUTURE WORK

This thesis presents the results of the development and investigation of novel concept of vibrating mesh atomizer. The atomizer is a micro-electromechanical system (MEMS) based device that works on principle of formation of droplets and fluid ejection by exploiting structural resonances of the thin vibrating membrane with number of apertures. Original contributions has been made in device fabrication as well as structural characterization (Chapter 3) of device operation. Successful operation of the device has been demonstrated for the number of working liquids (water, Spin on glass, low viscosity SU-8 resist and low viscosity mixtures of glycerol and water) and comparison of existing metallic device (commercial) demonstrated promising results in terms of better control of droplet distribution of droplets produced by the MEMS device. High viscosity mixtures of glycerol and water were problematic to atomize with the developed device so, reducing the viscosity values by supplying heat energy is the concept used further in the work. So design, fabrication and characterization of microheater device (Chapter 4) is demonstrated followed by integration of the two devices, atomizer and microheater to work as one integrated device (chapter 5) and demonstrated that the different high viscosity mixture of glycerol and water was atomizable and was characterized based on droplet size distribution and spray angle behavior. Finally the unique advantages of the developed atomizer are illustrated for variety of applications such spin-spray deposition of thin films, spray cooling to cool the heater substrate for micro level integrated circuits (chapter 6).

## **FUTURE RECOMMENDATIONS**

The experimentally validated Finite element analysis (FEA) simulations of the structural responses of the device in chapter 2 have been shown to predict resonant frequencies, modes, and displacement in the membrane for efficient device working. These simulations did not take the fluid at interface and chamber into consideration and nonlinear terms are not considered into governing equations. The FEA neglects other aspects of piezoelectric and acoustic actuation such as frictional losses in the fluid and heat generation. Therefore, following studies are recommended for future:

1. Investigation of acoustic response of the system should be conducted. The simulations or response study with respect to fluid properties, geometry of device and frequency of operation by coupling the acoustic physics with the structural mechanics. Accurate account of losses in the fluid should also be included in the model.
2. In addition, investigation of different geometries of the nozzle and PZT ceramic geometry and placement to determine which shape produce the greatest effect on working.

In chapter 2, the fluid ejection simulations are performed to observe the interface evolution during fluid ejection out of nozzle. These simulations enable to test wide range of fluid properties and device geometry as it is easier to investigate the effect of changing fluid properties than to actually perform large number of experiments. Some of the recommendation for future studies are:

1. Based on the actual nozzle shape obtained from the actual fabrication process, the simulation model could be modified to accurately represent the right profile of the nozzle i.e., they should be treated as pyramidal shape instead of conical shape which is

used in this thesis. To do this, it would add more complexities as the model will have to be built into 3-dimension which could be intense computationally. This should be combined with the variation in the nozzle dimension and different operating frequencies. The physiochemical properties of wide range of fluids such as high viscosity and low surface tension fluids should be investigated to understand the physics and to know the optimal operating parameters for the device.

2. Along with the alteration in the geometry of the device, it is recommended that the surface properties of the nozzle be investigated numerically by modifying the contact angle, slip no-slip conditions.

The device microfabrication and characterization in terms of resonance frequencies, atomization of various fluids is presented in chapter 3. The droplet formation concept by this device has been shown to address the challenges associated with the conventional atomization methods. This concept represents a low temperature and low power atomization of any potential liquid. Despite demonstrated unique advantages of the developed device, it has been found to be difficult to achieve reliable droplet formation/fluid ejection with high viscosity liquids and low surface tension, which presents unique challenges that provide a fruitful ground for future research. In particular, investigation of following device modifications is recommended for future research:

1. *Investigation of single nozzle to study the droplet formation* – It has been found that array of thousands of apertures makes it difficult to study the droplet behavior or journey from bulk to various phases of droplet formation. Less array of apertures on the center part of the membrane where displacement and velocity are maximum makes it easy to approach and study the phenomena of fluid ejection in this type of device.

CCD camera or laser-based system is required to study the fluid ejection journey like droplet necking and detachment, jetting, etc. and the various time like process time, inertial time, capillary time, and viscous time scale study.

2. *Effect of membrane material properties, nozzle orifice and fluid supply method on ejection of high viscosity liquids* – It is known from this study that the membrane of silicon material is stiff so the maximum operating conditions such as voltage and pressure is limited as it is likely to fail or break at the maximum stress points so, requirement of high pressure for high viscous liquids is not met with silicon membrane. Taking the advantage of microfabrication techniques, different material could be used for membrane with apertures to make it flexible and compatible for high displacement from the neutral axis at higher voltage. SU-8, polymer-based membrane is some of the materials could find its application in this device. Ejection of high viscosity liquids by ejector is possible if the viscous losses are overcome by nozzle tip and that is possible by larger pressure gradient. That means the device must be operable at high power input values which is prone to the heating, likelihood of membrane breaking. It is recommended that this design for manufacturability issue to be investigated further to determine the best equation between power consumption, simplicity of fabrication and device robustness. Supply of liquid to the nozzle is another aspect to investigate for high viscosity liquids. Bulk liquid in contact with the membrane makes it difficult to break or overcome the viscous forces with the maximum displacement. So, transfer of liquid through capillary action using wick or type of fabric that could hold the tiny amount of fluid and supply when suction is created on the membrane making it easy to break the viscous force little easy and doable.

3. Effect of surface properties on ejection of low surface tension liquids – It has been found that low viscosity liquids with low surface tension liquids are highly unstable and tend to weep through the nozzle membrane and travel to the other side of the nozzle and do not make detachment occur. To deal with low surface tension liquids, modifying the surface properties of the nozzle i.e., making the surface fluid philic using oxygen plasma but was made no change in the droplet formation so a permanent or more reliable coating like parylene would be desirable to alter the surface properties. The observation and the experience with device operation suggest it may be desirable to have wetting surface on the top surface and on nozzle to avoid any bubble or gap formation inside the nozzle and non-wetting surface on the outside of the nozzle to prevent formation of blocking fluid film. Careful experimental and theoretical investigation of related fluid mechanics would be of great value to device design and fabrication with the choice of coating with desired surface properties.
4. Assembly of piezoelectric thin film on the device – In this study, the piezoceramic ring is used for actuation and transfer of vibration onto the membrane. The literature and experience with device operation it may be desirable to have the piezoelectric material thin film on top of aperture membrane so that the lateral and vertical vibration are directly transferred to the membrane. There is a tradeoff with it, the piezoelectric constant of PZT ceramic is in range of 297pC/N whereas with the thin film it will be in range of 5-30pC/N depending on the thickness of the thin film. However, assembly of the piezo material with the MEMS device will make the device compact and inexpensive. Therefore, it is recommended that an investigation into the use of

microfabrication method to integrate the material and device together and study the performance.

The design and microfabrication of microheater device based on polymer substrate is presented in chapter 4. The microheaters are characterized based on their working temperature and power requirement. The characterization of integrated device with various mixture of glycerol and water is demonstrated in chapter 5. The two devices were integrated using 3D printed spacer and the assembly demonstrated good results. It is recommended that the two devices should have a better way to integrate and make it a single component. The microfabrication process should be investigated so that the microheater and micronozzles be manufactured using semiconductor process together instead of building individually and then assembly. Some of the future work recommendations are:

1. The single fabrication process will consist of resistor circuit on top of membrane itself and defect free metal layer will be a requirement for the circuit to work efficiently.
2. Insulation layer on top of resistor circuit should be compatible with the microfabrication methods and various materials should be investigated to find the perfect one.
3. Method of supply of viscous liquid should be altered and investigated. Now the supply of liquid is simply placing the drop on top of microheater, and the quantity of drop is not fixed every time. So, a method of supplying liquid through microchannels or using wick (capillary action) should be explored to determine the best way of supplying the fluid to the device.

In chapter 6, the microfabricated atomizer device was shown to be well-suited for atomization of spin on glass for development of silicon dioxide thin films using spin-spray deposition method, spray cooling which involves cooling of localized hotspots on an IC chip with non-uniform heat generation. and comparison with the conventional metallic mesh atomizer. Each of the application utilizes the key advantages of the developed device. The ability to produce monodisperse sub-micron size of droplet distribution makes it suitable for drug delivery applications and is very helpful in spin-spray deposition method. The low power consumption and no heat involvement makes it suitable for biological fluids. The higher spray angle of the spray and controlled drop size distribution produced by the device makes it suitable for spray cooling on the heated substrate.

The application-based study presented in chapter 6 demonstrates the range of applications of this vibrating mesh atomizer however as discussed in chapter 1, this technology can be utilized in any application that requires better control on droplet size and distribution which are repeatable and reliable. Wide range of applications opens up which involves the use of high viscosity liquids such as deposition of polymers, multilayer in additive manufacturing should be investigated.



## REFERENCES

1. Aliseda, A., et al., Atomization of viscous and non-newtonian liquids by a coaxial, high-speed gas jet. Experiments and droplet size modeling. *International Journal of Multiphase Flow*, 2008. **34**(2): p. 161-175.
2. Khmelev, V.N., A.V. Shalunov, and E.S. Smerdina. The Cavitation Spraying of the Viscous Liquids. in *International Workshops and Tutorials on Electron Devices and Materials*. 2006.
3. Gong, J.-S. and W.-B. Fu, The experimental study on the flow characteristics for a swirling gas–liquid spray atomizer. *Applied Thermal Engineering*, 2007. **27**(17): p. 2886-2892.
4. Schröder, J., et al., Characterization of gelatinized corn starch suspensions and resulting drop size distributions after effervescent atomization. *Journal of Food Engineering*, 2011. **105**(4): p. 656-662.
5. Lefebvre, A.H., *Atomization and sprays*. 1989, New York: Hemisphere Pub. Corp.
6. Khavkin, Y., *The theory and practice of swirl atomizers*. 2004, New York: Taylor & Francis.
7. Bayvel, L.P., *Liquid atomization*. 1993, Washington, D.C. :: Taylor & Francis.
8. Santati, S., J. Thongsri, and P. Sarntima, Modified Small-Volume Jet Nebulizer Based on CFD Simulation and Its Clinical Outcomes in Small Asthmatic Children. *Journal of Healthcare Engineering*, 2019. **2019**: p. 2524583.
9. Gogate, P.R., 30 - The use of ultrasonic atomization for encapsulation and other processes in food and pharmaceutical manufacturing, in *Power Ultrasonics*, J.A. Gallego-Juárez and K.F. Graff, Editors. 2015, Woodhead Publishing: Oxford. p. 911-935.
10. Olszewski, O.Z., et al., A Silicon-based MEMS Vibrating Mesh Nebulizer for Inhaled Drug Delivery. *Procedia Engineering*, 2016. **168**: p. 1521-1524.
11. Lass, J.S., A. Sant, and M. Knoch, New advances in aerosolised drug delivery: vibrating membrane nebuliser technology. *Expert Opin Drug Deliv*, 2006. **3**(5): p. 693-702.
12. Comparison of a nebulizer using a novel aerosol generator with a standard ultrasonic nebulizer designed for use during mechanical ventilation. 2001.
13. Turpeinen, M. and K. Nikander, Nebulization of a suspension of budesonide and a solution of terbutaline into a neonatal ventilator circuit. *Respir Care*, 2001. **46**(1): p. 43-8.
14. Elhissi, A.M.A. and K.M.G. Taylor, Delivery of liposomes generated from proliposomes using air-jet, ultrasonic, and vibrating-mesh nebulisers. *Journal of Drug Delivery Science and Technology*, 2005. **15**(4): p. 261-265.
15. Lentz, Y.K., T.J. Anchoroquy, and C.S. Lengsfeld, Rationale for the Selection of an Aerosol Delivery System for Gene Delivery. *Journal of Aerosol Medicine*, 2006. **19**(3): p. 372-384.
16. Dhand, R., Nebulizers that use a vibrating mesh or plate with multiple apertures to generate aerosol. *Respiratory care*, 2002. **47**(12): p. 1406-16; discussion 1416-8.
17. Ghazanfari, T., et al., The influence of fluid physicochemical properties on vibrating-mesh nebulization. *International Journal of Pharmaceutics*, 2007. **339**(1): p. 103-111.

18. Waldrep, J.C. and R. Dhand, Advanced nebulizer designs employing vibrating mesh/aperture plate technologies for aerosol generation. *Curr Drug Deliv*, 2008. **5**(2): p. 114-9.
19. Vehring, R., Pharmaceutical Particle Engineering via Spray Drying. *Pharmaceutical Research*, 2008. **25**(5): p. 999-1022.
20. Beck-Broichsitter, M., et al., Modified vibrating-mesh nozzles for advanced spray-drying applications. *European Journal of Pharmaceutics and Biopharmaceutics*, 2015. **92**: p. 96-101.
21. Lacas, F., et al., Design and Performance of an Ultrasonic Atomization System for experimental combustion applications. *Particle & Particle Systems Characterization*, 1994. **11**(2): p. 166-171.
22. Maehara, N., S. Ueha, and E. Mori, Influence of the vibrating system of a multipinhole-plate ultrasonic nebulizer on its performance. *Review of Scientific Instruments*, 1986. **57**(11): p. 2870-2876.
23. Toda, K. and J. Ishii, Operation Performance of Self-Oscillation Ultrasonic Vibrating Device for Liquid Atomization. *Japanese Journal of Applied Physics*, 1995. **34**(Part 1, No. 9B): p. 5332-5334.
24. De Heij, B., et al. Modelling and Optimisation of a vaporiser for inhalation drug therapy. in *Proceedings of the Second International Conference on Modelling and Simulation of Microsystems*. 1999. Citeseer.
25. Pan, C.T., J. Shiea, and S.C. Shen, Fabrication of an integrated piezo-electric micro-nebulizer for biochemical sample analysis. *Journal of Micromechanics and Microengineering*, 2007. **17**(3): p. 659-669.
26. Perçin, G., L. Levin, and B.T. Khuri-Yakub, Piezoelectrically actuated droplet ejector. *Review of Scientific Instruments*, 1997. **68**(12): p. 4561-4563.
27. Perçin, G. and B.T. Khuri-Yakub, Piezoelectric droplet ejector for ink-jet printing of fluids and solid particles. *Review of Scientific Instruments*, 2003. **74**(2): p. 1120-1127.
28. Shen, S.-C., Y.-J. Wang, and Y.-Y. Chen, Design and fabrication of medical micro-nebulizer. *Sensors and Actuators A: Physical*, 2008. **144**(1): p. 135-143.
29. Shen, S.C., A new cymbal-shaped high power microactuator for nebulizer application. *Microelectronic Engineering*, 2010. **87**(2): p. 89-97.
30. Yan, Q., W. Sun, and J. Zhang, Study on the Influencing Factors of the Atomization Rate in a Piezoceramic Vibrating Mesh Atomizer. *Applied Sciences*, 2020. **10**(7).
31. Chen, H., et al., Experimental study on optimal spray parameters of piezoelectric atomizer based spray cooling. *International Journal of Heat and Mass Transfer*, 2016. **103**: p. 57-65.
32. Tsao, C.-W., et al., Piezo-Ring-on-Chip Microfluidic Device for Simple and Low-Cost Mass Spectrometry Interfacing. *The Analyst*, 2018. **143**.
33. Cheng, Y., et al., Numerical investigation of droplet spreading and heat transfer on hot substrates. *International Journal of Heat and Mass Transfer*, 2018. **121**: p. 402-411.
34. Lejeune, M., et al., Ink-jet printing of ceramic micro-pillar arrays. *Journal of the European Ceramic Society*, 2009. **29**(5): p. 905-911.
35. Vecellio, L., The mesh nebuliser: a recent technical innovation for aerosol delivery. *Breathe*, 2006. **2**(3): p. 252.

36. Zhang, G., A. David, and T.S. Wiedmann, Performance of the Vibrating Membrane Aerosol Generation Device: Aeroneb Micropump Nebulizer™. *Journal of Aerosol Medicine*, 2007. **20**(4): p. 408-416.
37. Yan, Q., C. Wu, and J. Zhang, Effect of the Dynamic Cone Angle on the Atomization Performance of a Piezoceramic Vibrating Mesh Atomizer. *Applied Sciences*, 2019. **9**(9).
38. Kuo, Y.-M., et al., Characterization of Vibrating Mesh Aerosol Generators. *Aerosol and Air Quality Research*, 2019. **19**(8): p. 1678-1687.
39. Yan, Q., W. Sun, and J. Zhang, Study on the formation and separation process of droplets in the medical piezoelectric atomization device induced by intra-hole fluctuation. 2020.
40. Moon, S.-H., et al., Effects of Driving Frequency and Voltage on the Performances of Vibrating Mesh Nebulizers. *Applied Sciences*, 2021. **11**: p. 1296.
41. Yan, Q., et al., Effects of Vibration Characteristics on the Atomization Performance in the Medical Piezoelectric Atomization Device Induced by Intra-Hole Fluctuation. *Chinese Journal of Mechanical Engineering*, 2021. **34**.
42. Sharma, P. and N. Jackson. Spin-spray deposition of spin on glass using MEMS atomizer. in 2021 IEEE 34th International Conference on Micro Electro Mechanical Systems (MEMS). 2021. IEEE.
43. Sharma, P. and N. Jackson, Vibrating Mesh Atomizer for Spin-Spray Deposition. *Journal of Microelectromechanical Systems*, 2021. **30**(4): p. 582-588.
44. Law, J., et al., Atomization of High-Viscosity Fluids for Aromatherapy Using Microheaters for Heterogeneous Bubble Nucleation. *Scientific Reports*, 2017. **7**(1): p. 40289.
45. Pritchard, J.N., et al., Mesh nebulizers have become the first choice for new nebulized pharmaceutical drug developments. *Therapeutic Delivery*, 2018. **9**(2): p. 121-136.
46. Leissa, A.W., *Vibration of Plates*. NASA-SP160, National Aeronautics and Space Administration, Washington DC., 1969.
47. Martin, G.D. and I.M. Hutchings, *Fundamentals of Inkjet Technology*, in *Inkjet Technology for Digital Fabrication*. p. 21-44.
48. Lee, E., *Microdrop Generation*. 2002. 1-253.
49. Furlani, E.P., *Fluid Mechanics for Inkjet Printing*, in *Fundamentals of Inkjet Printing*. 2016. p. 13-56.
50. Meinhart, C.D. and H. Zhang, The flow structure inside a microfabricated inkjet printhead. *Journal of Microelectromechanical Systems*, 2000. **9**(1): p. 67-75.
51. Harlow, F.H. and J.E. Welch, Numerical Calculation of Time-Dependent Viscous Incompressible Flow of Fluid with Free Surface. *The Physics of Fluids*, 1965. **8**(12): p. 2182-2189.
52. Amsden, A.A. and F.H. Harlow, A simplified MAC technique for incompressible fluid flow calculations. *Journal of Computational Physics*, 1970. **6**(2): p. 322-325.
53. Vecelli, J.A., A computing method for incompressible flows bounded by moving walls. *Journal of Computational Physics*, 1971. **8**(1): p. 119-143.
54. Chan, R.K.C. and R.L. Street, A computer study of finite-amplitude water waves. *Journal of Computational Physics*, 1970. **6**(1): p. 68-94.
55. Nichols, B.D., C.W. Hirt, and R.S. Hotchkiss, SOLA-VOF: a solution algorithm for transient fluid flow with multiple free boundaries. 1980: United States. p. 123.

56. Heinzen, C., A. Berger, and I. Marison, Use of Vibration Technology for Jet Break-Up for Encapsulation of Cells and Liquids in Monodisperse Microcapsules. *Fundamentals of Cell Immobilisation Biotechnology*, 2004. **8**.
57. Yan, Q., C. Wu, and J. Zhang, Effect of the Dynamic Cone Angle on the Atomization Performance of a Piezoceramic Vibrating Mesh Atomizer. *Applied Sciences*, 2019. **9**(9): p. 1836.
58. Cai, Y., et al., Theoretical calculations and experimental verification for the pumping effect caused by the dynamic micro-tapered angle. *Chinese Journal of Mechanical Engineering*, 2016. **29**(3): p. 615-623.
59. Houlihan, R., et al. Acoustic Structural Coupling In A Silicon Based Vibrating Mesh Nebulizer. in *2021 21st International Conference on Solid-State Sensors, Actuators and Microsystems (Transducers)*. 2021. IEEE.
60. Ghazanfari, T., et al., The influence of fluid physicochemical properties on vibrating-mesh nebulization. *International journal of pharmaceutics*, 2007. **339**(1-2): p. 103-111.
61. Guerra-Bravo, E., et al., Vibration Analysis of a Piezoelectric Ultrasonic Atomizer to Control Atomization Rate. *Applied Sciences*, 2021. **11**(18): p. 8350.
62. Yan, Q., et al., Effects of Vibration Characteristics on the Atomization Performance in the Medical Piezoelectric Atomization Device Induced by Intra-Hole Fluctuation. *Chinese Journal of Mechanical Engineering*, 2021. **34**(1): p. 123.
63. Zhang, J., et al., Experimental Verification of the Pumping Effect Caused by the Micro-Tapered Hole in a Piezoelectric Atomizer. *Sensors*, 2018. **18**(7): p. 2311.
64. Dean, A.M. and D. Voss, *Design and Analysis of Experiments*. Springer Texts in Statistics. 2000: Springer New York.
65. Kutner, M.H., Neter, J., Nachtsheim, C.J. and Li, W. , *Applied Linear Regression Models* 2004.
66. Palasagaram, J.N. and R. Ramadoss, MEMS-Capacitive Pressure Sensor Fabricated Using Printed-Circuit-Processing Techniques. *IEEE Sensors Journal*, 2006. **6**(6): p. 1374-1375.
67. Wu, S., et al., MEMS flow sensors for nano-fluidic applications. *Sensors and Actuators A: Physical*, 2001. **89**(1): p. 152-158.
68. Wang, Y.-H., C.-Y. Lee, and C.-M. Chiang, A MEMS-based Air Flow Sensor with a Free-standing Micro-cantilever Structure. *Sensors (Basel, Switzerland)*, 2007. **7**(10): p. 2389-2401.
69. Cognata, T., K. Hollingsworth, and L. Witte, High-Speed Visualization of Two-Phase Flow in a MicroScale Pin-Fin Heat Exchanger. *Heat Transfer Engineering*, 2007. **28**.
70. Lewis, D.H., et al., Digital micropropulsion. *Sensors and Actuators A: Physical*, 2000. **80**(2): p. 143-154.
71. Prasad, M., et al., FEM simulation of platinum-based microhotplate using different dielectric membranes for gas sensing applications. *Sensor Review*, 2012. **32**(1): p. 59-65.
72. Setti, L., et al., Thermal Inkjet Technology for the Microdeposition of Biological Molecules as a Viable Route for the Realization of Biosensors. *Analytical Letters - ANAL LETT*, 2004. **37**: p. 1559-1570.
73. Mendum, T., et al., Concentration of bisphenol A in thermal paper. *Green Chemistry Letters and Reviews*, 2011. **4**(1): p. 81-86.

74. Setti, L., et al., Thermal Inkjet Technology for the Microdeposition of Biological Molecules as a Viable Route for the Realization of Biosensors. *Analytical Letters*, 2004. **37**(8): p. 1559-1570.
75. Zhou, W. Interface dynamics in inkjet deposition. 2014.
76. Lahlalia, A., et al., Electro-Thermal Simulation & Characterization of a Microheater for SMO Gas Sensors. *Journal of Microelectromechanical Systems*, 2018. **27**(3): p. 529-537.
77. Elmi, I., et al., Development of ultra-low-power consumption MOX sensors with ppb-level VOC detection capabilities for emerging applications. *Sensors and Actuators B: Chemical*, 2008. **135**(1): p. 342-351.
78. Spannake, J., et al., SnO<sub>2</sub>:Sb – A new material for high-temperature MEMS heater applications: Performance and limitations. *Sensors and Actuators B: Chemical*, 2007. **124**(2): p. 421-428.
79. Nguyen, H., et al., Controllable growth of ZnO nanowires grown on discrete islands of Au catalyst for realization of planar-type micro gas sensors. *Sensors and Actuators B: Chemical*, 2014. **193**: p. 888-894.
80. Dai, C.-L., A capacitive humidity sensor integrated with micro heater and ring oscillator circuit fabricated by CMOS–MEMS technique. *Sensors and Actuators B: Chemical*, 2007. **122**(2): p. 375-380.
81. Nerushev, O.A., J. Ek-Weis, and E.E.B. Campbell, In situ studies of growth of carbon nanotubes on a local metal microheater. *Nanotechnology*, 2015. **26**(50): p. 505601.
82. Zhang, K.L., S.K. Chou, and S.S. Ang, Fabrication, modeling and testing of a thin film Au/Ti microheater. *International Journal of Thermal Sciences*, 2007. **46**(6): p. 580-588.
83. Toskov, S., et al. Modeling and fabrication of Pt micro-heaters built on alumina Substrate. in *Proceedings of the 36th International Spring Seminar on Electronics Technology*. 2013.
84. Tiwari, S.K., S. Bhat, and K.K. Mahato, Design and fabrication of screen printed microheater. *Microsystem Technologies*, 2018. **24**(8): p. 3273-3281.
85. Aslam, M., C. Gregory, and J.V. Hatfield, Polyimide membrane for micro-heated gas sensor array. *Sensors and Actuators B: Chemical*, 2004. **103**(1): p. 153-157.
86. Maeder, T., L. Sagalowicz, and P. Muralt, Stabilized Platinum Electrodes for Ferroelectric Film Deposition Using Ti, Ta and Zr Adhesion Layers. *Japanese Journal of Applied Physics*, 1998. **37**.
87. Hwang, W.J., et al., Development of micro-heaters with optimized temperature compensation design for gas sensors. *Sensors (Basel)*, 2011. **11**(3): p. 2580-91.
88. Zhou, Y., et al. Design and Fabrication of Microheaters for Localized Carbon Nanotube Growth. in *2008 8th IEEE Conference on Nanotechnology*. 2008.
89. Yu, S., et al., A novel polyimide based micro heater with high temperature uniformity. *Sensors and Actuators A: Physical*, 2017. **257**: p. 58-64.
90. Creemer, J.F., et al., Microhotplates with TiN heaters. *Sensors and Actuators A: Physical*, 2008. **148**(2): p. 416-421.
91. Gordillo, G., F. Mesa, and C. Calderón, Electrical and morphological properties of low resistivity Mo thin films prepared by magnetron sputtering. *Brazilian Journal of Physics*, 2006. **36**: p. 982-985.
92. Mele, L., et al., A molybdenum MEMS microhotplate for high-temperature operation. *Sensors and Actuators A: Physical*, 2012. **188**: p. 173-180.

93. Bott, B. and T.A. Jones, A highly sensitive NO<sub>2</sub> sensor based on electrical conductivity changes in phthalocyanine films. *Sensors and Actuators*, 1984. **5**(1): p. 43-53.
94. Giberti, A., et al., Influence of ambient temperature on electronic conduction in thick-film gas sensors. *Sensors and Actuators B: Chemical*, 2009. **137**(1): p. 111-114.
95. Jang, D., D. Kim, and J. Moon, Influence of Fluid Physical Properties on Ink-Jet Printability. *Langmuir*, 2009. **25**(5): p. 2629-2635.
96. Jeng, S.M., M.A. Jog, and M.A. Benjamin, Computational and Experimental Study of Liquid Sheet Emanating from Simplex Fuel Nozzle. *AIAA Journal*, 1998. **36**(2): p. 201-207.
97. Eslamian, M. and N. Ashgriz, Swirl, T-Jet and Vibrating-Mesh Atomizers, in *Handbook of Atomization and Sprays: Theory and Applications*, N. Ashgriz, Editor. 2011, Springer US: Boston, MA. p. 755-773.
98. Sharma, P. and N. Jackson, Spin-Spray Deposition of Spin on Glass using MEMS Atomizer, in *IEEE MEMS 2021*. 2021. p. 681-684.
99. Sahu, N., B. Parija, and S. Panigrahi, Fundamental understanding and modeling of spin coating process: A review. *Indian Journal of Physics*, 2009. **83**(4): p. 493-502.
100. Lawrence, C.J. and W. Zhou, Spin coating of non-Newtonian fluids. *Journal of Non-Newtonian Fluid Mechanics*, 1991. **39**(2): p. 137-187.
101. Pham, N., et al., Spin, Spray coating and Electrodeposition of photoresist for MEMS structures - A comparison. 2003.
102. Peterson, R.J., Literature Review of Spin On Glass. 2016, Los Alamos National Lab.(LANL), Los Alamos, NM (United States).
103. Ergül, A. Nano Circuits Based on Vertical Transport. 2005.
104. Packeer, F., et al., Alternative Spin-On-Glass (SoG) material characterization For Deep-Submicron (<0.35 um) soft reflow fabrication process. *IOP Conference Series: Materials Science and Engineering*, 2018. **380**.
105. Guodong, H., A.S. Holmes, and M.E. Heaton. SU8 resist plasma etching and its optimisation. in *Symposium on Design, Test, Integration and Packaging of MEMS/MOEMS 2003*. 2003.
106. Seidemann, V., et al., SU8-micromechanical structures with in situ fabricated movable parts. *Microsystem technologies*, 2002. **8**(4-5): p. 348-350.
107. Obi, O., Magnetic thin film characterization by spin spray process. 2008, Northeastern University.
108. Caruntu, G., et al., Magnetic characterization of nanocrystalline nickel ferrite films processed by a spin-spraying method. *Journal of Physics D: Applied Physics*, 2005. **38**(6): p. 811-815.
109. Okazaki, T., et al., Spectroelectrochemical Evaluation of a ZnO Optically Transparent Electrode Prepared by the Spin-spray Technique. *Electroanalysis*, 2020. **32**(8): p. 1681-1688.
110. Kim, H., et al., Laser interference lithography using spray/spin photoresist development method for consistent periodic nanostructures. *Current Applied Physics*, 2014. **14**(2): p. 209-214.
111. Dalmoro, A., M. d'Amore, and A.A. Barba, Droplet size prediction in the production of drug delivery microsystems by ultrasonic atomization. *Translational Medicine@ UniSa*, 2013. **7**: p. 6.

112. Ramisetty, K.A., A.B. Pandit, and P.R. Gogate, Investigations into ultrasound induced atomization. *Ultrasonics sonochemistry*, 2013. **20**(1): p. 254-264.
113. Zhang, Y., S. Yuan, and L. Wang, Investigation of capillary wave, cavitation and droplet diameter distribution during ultrasonic atomization. *Experimental Thermal and Fluid Science*, 2021. **120**: p. 110219.
114. Chen, J.-n., et al., Phenomenon and Mechanism of Spray Cooling on Nanowire Arrayed and Hybrid Micro/Nanostructured Surfaces. *Journal of Heat Transfer*, 2018. **140**(11).
115. Hata, K. and Q.S. Liu, Conductive and viscous sub-layers on forced convection and mechanism of critical heat flux during flow boiling of subcooled water in a platinum circular tube with 3 mm inner diameter and 32.7 mm heated length at high liquid Reynolds number. *International Journal of Heat and Mass Transfer*, 2020. **162**: p. 120269.
116. He, W., et al., Experimental investigation on the performance of a novel dual synthetic jet actuator-based atomization device. *International Journal of Heat and Mass Transfer*, 2019. **142**: p. 118406.
117. Hsieh, S.-S., et al., Spray cooling heat transfer on microstructured thin film enhanced surfaces. *Experimental Thermal and Fluid Science*, 2015. **68**: p. 123-134.
118. Yan, Z.B., et al., Large area impingement spray cooling from multiple normal and inclined spray nozzles. *Heat and Mass Transfer*, 2013. **49**: p. 985-990.
119. Opoku, R. and J.P. Kizito, Experimental investigation of heat transfer characteristics and performance of smooth and wicking surfaces in spray cooling for high heat flux applications. *Results in Engineering*, 2020. **6**: p. 100119.
120. Zhou, N., et al., Experimental investigation on the performance of a water spray cooling system. *Applied Thermal Engineering*, 2017. **112**: p. 1117-1128.
121. Zhang, Z., et al., Experimental investigation of spray cooling on smooth and micro-structured surfaces. *International Journal of Heat and Mass Transfer*, 2014. **76**: p. 366-375.
122. Zhou, Z.-F., et al., Heat transfer characteristics during pulsed spray cooling with R404A at different spray distances and back pressures. *Applied Thermal Engineering*, 2016. **102**: p. 813-821.
123. Hou, Y., et al., Experimental study on phase change spray cooling. *Experimental Thermal and Fluid Science*, 2013. **46**: p. 84-88.
124. Choi, K.-H., et al., Fabrication and Characterization of Medical Mesh-Nebulizer for Aerosol Drug Delivery. *Applied Sciences*, 2018. **8**: p. 604.
125. Yan, Q., C. wu, and J. Zhang, Effect of the Dynamic Cone Angle on the Atomization Performance of a Piezoceramic Vibrating Mesh Atomizer. *Applied Sciences*, 2019. **9**: p. 1836.
126. Moon, S.-H., et al., Effects of Driving Frequency and Voltage on the Performances of Vibrating Mesh Nebulizers. *Applied Sciences*, 2021. **11**(3): p. 1296.
127. Hsieh, S.-S., C.-F. Huang, and Y.-M. Lu, Water spray heat transfer through a piezoelectric atomizer with a single-hole micronozzle. *Journal of Mechanical Science and Technology*, 2020. **34**: p. 1-10.
128. Hsieh, S.-S., Y.-F. Hsu, and M.-L. Wang, A microspray-based cooling system for high powered LEDs. *Energy Conversion and Management*, 2014. **78**: p. 338-346.
129. Liu, X., et al., Effects of injection pressure difference on droplet size distribution and spray cone angle in spray cooling of liquid nitrogen. *Cryogenics*, 2017. **83**: p. 57-63.